POLITECNICO DI MILANO

School of Civil, Environmental and Land Management Engineering

Master of Science in
Civil Engineering – Structures

HOMOGENIZATION AND ELASTIC WAVE POLARIZATION IN ANISOTROPIC LOCALLY RESONANT METAMATERIALS

Supervisor:
Prof. Claudia Comi

Co-supervisors:
Prof. Angela Vincenti
Dr. David Faraci

Candidate:
Francesco Mendicino – 995829

Academic Year 2022 – 2023

Acknowledgements

I would like to thank, firstly, Professors Claudia Comi and Angela Vincenti for their continued availability. Of course, a big thank goes to Dr. David Faraci for his kind cooperation in this work. I learned notions that will be useful, in some way, for my future career and this thesis represents an excellent conclusion of my last course of study at Politecnico di Milano. The experience in Paris at Sorbonne Universitè has been very important not only for academic reasons but also for a personal growth. I'm very honored to take part of this work team also for the preparation of an article for a scientific journal. My last but not less important thanks go to my family and friends for the moral support.

Abstract

Locally resonant metamaterials are artificial composites that, by a proper design, can control the elastic wave propagation and provide the band gaps. The latter are special frequency ranges in which waves cannot propagate without attenuation. In particular, anisotropic locally resonant metamaterials are able to provide also the polarization control of elastic waves in specific frequency intervals, called polarization bands.
In the present work, we take into consideration a ternary locally resonant metamaterial made of a periodic repetition of cells with non-symmetrically coated inclusion and we obtain the equivalent anisotropic dynamic mass density tensor through the two-scale asymptotic homogenization technique. The eigenvalues of this tensor allow us to identify the band gaps and the polarization bands.
With a proper geometric configuration of the metamaterial, mode-converting mechanisms can be achieved within these polarization bands. Transmission analyses confirm the possibility to generate mode-conversion.
The developed homogenization technique allows to analyze the effect of several geometric parameters. A further development of this work could be in direction of metamaterial optimization for specific requests.

Contents

Acknowledgements i

Abstract iii

List of Figures vii

List of Tables xi

1 Introduction 1
- 1.1 Anisotropy of locally resonant materials and mode conversion applications . . . 1
- 1.2 Aims of the work . . . 8
- 1.3 Outline of the thesis . . . 8

2 Elastic wave propagation in metamaterials 11
- 2.1 Wave propagation in homogeneous media . . . 11
- 2.2 Wave propagation in periodic metamaterials . . . 14
- 2.3 Examples of discrete periodic metamaterials . . . 18
  - 2.3.1 1D monoatomic chain . . . 18
  - 2.3.2 2D mass-in-mass chain . . . 19

3 Dynamic homogenization of locally-resonant metamaterials 31
- 3.1 Problem formulation . . . 31
- 3.2 Asymptotic homogenization . . . 32
- 3.3 Motion in the matrix . . . 34
- 3.4 Motion in the inclusions . . . 35
- 3.5 Homogenized equation of motion . . . 37
- 3.6 Effective dispersion properties . . . 37

4 Evaluation of the homogenized properties 39
- 4.1 Effective stiffness . . . 40
  - 4.1.1 Square unit cell with circular inclusions . . . 40
  - 4.1.2 Rhomboidal unit cell with circular inclusions . . . 44
- 4.2 Effective mass density . . . 47
  - 4.2.1 Perfectly centered fiber . . . 48
  - 4.2.2 Eccentric fiber . . . 49
- 4.3 Band-gaps prediction by Bloch-Floquet analysis . . . 50
  - 4.3.1 Perfectly centered fiber . . . 50
  - 4.3.2 Eccentric fiber . . . 51

4.4 Effective dispersion properties 54
4.4.1 Square unit cell with eccentric fiber 54
4.4.2 Rhomboidal unit cells with eccentric fiber 57
4.5 Parametric discussion 60

5 Transmission analyses **65**
5.1 Eccentric fibers with θ=0° 66
5.1.1 $\boldsymbol{e}_I$-transmission analysis 66
5.1.2 $\boldsymbol{e}_{II}$-transmission analysis 69
5.2 Eccentric fibers with θ=90° 71
5.2.1 $\boldsymbol{e}_I$-transmission analysis 71
5.2.2 $\boldsymbol{e}_{II}$-transmission analysis 72
5.3 Eccentric fibers with θ=45° 73

6 Conclusions and further developments **79**

Bibliography **83**

List of Figures

Figure1.1 Unpolarized light, possessing random polarization, passes through a linear polarizer to create linearly polarized light, then passes through a quarter-wave plate to create circularly polarized light (from [20]). . 4
Figure1.2 Illustration of ground motions produced by compressional or P-waves and shear or S-waves (from [21]). 4
Figure1.3 An illustration of a mode-coupled layer surrounded by an isotropic medium. The incident longitudinal wave can be converted to the shear wave as it propagates through the mode-coupled layer (from [23]). 5
Figure1.4 The principle of the ultrasonic shear-wave tomography system (from [24]). 6
Figure1.5 a) Ultrasonic shear-wave tomography instrument b) Analysis image (from [24]). 6

Figure2.1 Three-dimensional homogeneous media 11
Figure2.2 Polar diagrams of normalized phase velocities with respect to propagation directions (blue) and with superposed polarization directions (red) 14
Figure2.3 a) 2D b) 3D Primitive Bravais lattices, from [36] 15
Figure2.4 a) Metamaterial with hollowed square unit cells b) Wigner-Seitz primitive cell c) FBZ and IBZ 16
Figure2.5 Boundaries of the IBZ (red) for a square reciprocal Wigner-Seitz cell 17
Figure2.6 Rhomboidal unit cell: a) Wigner-Seitz primitive rhomboidal cell b) reciprocal hexagonal cell (FBZ) with the boundaries of the IBZ depicted in red 17
Figure2.7 1D monoatomic chain 18
Figure2.8 2D "mass-in-mass"-spring lattice: the blue box indicates the unitary cell of side L, while the red one identifies a focus zone useful for the derivation of the dynamic equlibrium equations 20
Figure2.9 2D "mass-in-mass"-spring lattice: focus zone (red box) 20
Figure2.10 Dispersion curves versus effective mass: isotropic case with s_1=s_2=630.22 [N/m] 25
Figure2.11 Dispersion curves versus effective mass: isotropic case with s_2=s_1=1721.00 [N/m] 25
Figure2.12 Dispersion curves versus effective masses: anisotropic case with s_1=630.22 [N/m] and s_2=1721.00 [N/m] 26

Figure2.13 Opening and closure frequencies along x_1 and x_2 in function of β: cases with α=0.1, 1 29
Figure2.14 Opening and closure frequencies along x_1 and x_2 in function of β: cases with α=3, 10 29

Figure3.1 a) Geometry of locally resonant metamaterial b) Unit cell with eccentric fiber 31
Figure3.2 State of stress on ∂Y_f of the fiber 36

Figure4.1 a) Square unit cell with eccentric fiber b) Rhomboidal unit cell with eccentric fiber 39
Figure4.2 Square unit cell of the periodic media with holes instead of inclusions 40
Figure4.3 Tension test along direction x_1 for the square cell: comparison of the contour of displacement along x_1 between real and homogenized model 41
Figure4.4 Non-pure shear test for the square cell: comparison of the contour of displacement along x_2 between real and homogenized model (case 1) 43
Figure4.5 Non-pure shear test for the square cell: comparison of the contour of displacement along x_2 between real and homogenized model (case 2) 43
Figure4.6 Rhoboidal unit cell of the periodic media with holes instead of inclusions 44
Figure4.7 Tension test along direction x_1 for the rhomboidal cell: comparison of the contour of displacement along x_1 between real and homogenized model 45
Figure4.8 Tension test along direction x_2 for the rhomboidal cell: comparison of the contour of displacement along x_2 between real and homogenized model 46
Figure4.9 Non-pure shear test for the rhomboidal cell: comparison of the contour of displacement along x_2 between real and homogenized model 47
Figure4.10 Circular inclusions: coating with eccentric fiber 48
Figure4.11 Normalized effective mass density for the perfectly centered fiber (null horizontal eccentricity) 48
Figure4.12 Normalized effective mass density for the eccentric fiber (horizontal eccentricity e=1.5 mm) 49
Figure4.13 a) Dispersion curves of the square unit cell with perfectly centered fiber b) Dispersion curves of the rhomboidal unit cell with perfectly centered fiber c) Normalized effective mass density for the perfectly centered fiber 50
Figure4.14 a) Dispersion curves of the square unit cell with eccentric fiber b) Dispersion curves of the rhomboidal unit cell with eccentric fiber c) Normalized effective mass density for the eccentric fiber 51
Figure4.15 Dispersion surfaces for the square unit cell with eccentric fiber on FBZ, 3D view 52

Figure4.16 Comparison between dispersion curves along the IBZ a) and dispersion surfaces on FBZ, lateral view b) for the square unit cell with eccentric fiber 52
Figure4.17 Dispersion surfaces for the rhomboidal unit cell with eccentric fiber on FBZ, 3D view 53
Figure4.18 Comparison between dispersion curves along the IBZ a) and dispersion surfaces on FBZ, lateral view b) for the rhomboidal unit cell with eccentric fiber 54
Figure4.19 Square unit cell with eccentric fiber: phase velocities (black line) and polarization directions (red line) within different propagation directions (blue line) when $\rho^0_{11}<0$ and $\rho^0_{22}>0$. a) Low mass contrast b) High mass contrast 55
Figure4.20 Square unit cell with eccentric fiber: phase velocities (black line) and polarization directions (red line) within different propagation directions (blue line) when $\rho^0_{22}<0$ and $\rho^0_{11}>0$. a) Low mass contrast b) High mass contrast 57
Figure4.21 Rhmoboidal unit cells: geometrical configurations 57
Figure4.22 Rhomboidal unit cells with eccentric fiber: phase velocities (black line) and polarization directions (red line) within different propagation directions (blue line) when $\rho^0_{11}<0$ and $\rho^0_{22}>0$ (frequency $\omega/2\pi$=1200 Hz) 58
Figure4.23 Rhomboidal unit cells with eccentric fiber: phase velocities (black line) and polarization directions (red line) within different propagation directions (blue line) when $\rho^0_{22}<0$ and $\rho^0_{11}>0$ (frequency $\omega/2\pi$=920 Hz) 60
Figure4.24 Fiber radius R_f variation, maintaining fixed the coating radius R_c and the horizontal eccentricity e of the fiber 61
Figure4.25 Frequency bands in which $\rho^0_{11} < 0$ and $\rho^0_{22} > 0$ (blue), $\rho^0_{22} < 0$ and $\rho^0_{11} > 0$ (red) and $\rho^0_{11} < 0$ and $\rho^0_{22} < 0$ (purple) for different values of the ratio R_f/R_c 61
Figure4.26 Horizontal eccentricity e variation, related to the fiber, maintaining fixed the coating radius R_c and the fiber radius R_f 62
Figure4.27 Frequency bands in which $\rho^0_{11} < 0$ and $\rho^0_{22} > 0$ (blue), $\rho^0_{22} < 0$ and $\rho^0_{11} > 0$ (red) and $\rho^0_{11} < 0$ and $\rho^0_{22} < 0$ (purple) for different values of the ratio e/e_{max} 63

Figure5.1 Unit cell of the three different kind of metamaterial considered with a) $\theta = 0°$ b) $\theta = 45°$ c) $\theta = 90°$. 65
Figure5.2 Principal values of the effective mass density tensor for $L = 21$ mm, $R_c = 7.5$, $R_f = 3.5$ mm and $e = 3.25$ mm. 66
Figure5.3 Array of 40×1 cells with horizontally eccentric fibers ($\theta = 0°$), employed in the $\boldsymbol{e}_I$-transmission analysis. 67
Figure5.4 Transmission spectrum of $|\langle u\rangle|$ as a function of frequency for the array of 40×1 cells (θ=0°) with imposed $\boldsymbol{e}_I$-displacement. 67

Figure5.5 a) Contour plot of the horizontal displacement in the first twelve cells of the array at frequency $\omega/2\pi = 505$ Hz b) Contour plot of the horizontal displacement in the first six cells of the array at frequency $\omega/2\pi = 681$ Hz c) Contour plot of the horizontal displacement in the last six cells of the array at frequency $\omega/2\pi = 681$ Hz. 68
Figure5.6 Contour plot of the horizontal displacement in the last twenty-four cells of the array at frequency $\omega/2\pi = 442$ Hz. 69
Figure5.7 Array of 40×1 cells with horizontally eccentric fibers ($\theta = 0°$), employed in the $\boldsymbol{e}_{II}$-transmission analysis. 69
Figure5.8 Transmission spectrum of $|\langle v \rangle|$ as a function of the frequency for the array 40×1 cells (θ=0°) and the imposed $\boldsymbol{e}_{II}$-displacement. . . 70
Figure5.9 a) Contour plot of the vertical displacement in the first ten cells of the array at frequency $\omega/2\pi = 371$ Hz b) Contour plot of the vertical displacement in the first fourteen cells of the array at frequency $\omega/2\pi = 447$ Hz. 70
Figure5.10 Array of 40×1 cells with vertically eccentric fibers ($\theta = 90°$), employed in the $\boldsymbol{e}_{I}$-transmission analysis. 71
Figure5.11 Transmission spectrum of $|\langle v \rangle|$ as a function of the frequency for the array 40×1 cells (θ=90°) and the imposed $\boldsymbol{e}_{I}$-displacement. . . 71
Figure5.12 Array of 40×1 cells with vertically eccentric fibers ($\theta = 90°$), employed in the $\boldsymbol{e}_{II}$-transmission analysis. 72
Figure5.13 Transmission spectrum of $|\langle u \rangle|$ as a function of the frequency for the array 40×1 cells (θ=90°) and the imposed $\boldsymbol{e}_{II}$-displacement. The close-up in red represent a more refined trends of $|\langle u \rangle|$ at two different frequencies. 73
Figure5.14 Media of 7×21 cells and eccentric fibers with $\theta = 45°$, employed in the inclined transmission analysis. 74
Figure5.15 Transmission spectrum of $|\langle u\cos(45°) + v\sin(45°)\rangle|$ in P_1 as a function of the frequency for the inclined transmission analysis. . . . 74
Figure5.16 Contour plot of $u\cos(45°) + v\sin(45°)$ on the deformed shape for: a) $\omega/2\pi = 540$ Hz b) $\omega/2\pi = 591$ Hz c) $\omega/2\pi = 677$ Hz. 75
Figure5.17 Close-up view of the transmission spectrum of figure 5.15 at frequencies: a) $\omega/2\pi = 540.1$ Hz b) $\omega/2\pi = 591.5$ Hz c) $\omega/2\pi = 676.4$ Hz. The black line is $|\langle u\cos(45°) + v\sin(45°)\rangle|$ and the green line is $|\langle -u\sin(45°) + v\cos(45°)\rangle|$. 76
Figure5.18 Transmission spectrum of $|\langle -u\sin(45°) + v\cos(45°)\rangle|$ in P_2 as a function of the frequency for the inclined transmission analysis. . . 76
Figure5.19 Contour plot of $-u\sin(45°) + v\cos(45°)$ on the deformed shape for: a) $\omega/2\pi = 306$ Hz b) $\omega/2\pi = 368$ Hz c) $\omega/2\pi = 392$ Hz. 77
Figure5.20 Close-up view of the transmission spectrum of figure 5.18 at frequencies: a) $\omega/2\pi = 306.2$ Hz b) $\omega/2\pi = 367.4$ Hz c) $\omega/2\pi = 392.4$ Hz. The green line is $|\langle -u\sin(45°) + v\cos(45°)\rangle|$ and the black line is $|\langle u\cos(45°) + v\sin(45°)\rangle|$. 78

List of Tables

Table2.1 Maximization and minimization discussion for k_2L along Γ X for α=0.1 27
Table2.2 Maximization and minimization discussion for k_1L along XM for α=0.1 28
Table2.3 Maximization and minimization discussion for k_1L=k_2L along MΓ for α=0.1 28

Table4.1 Geometrical and material properties 40
Table4.2 Tension test along direction x_1 for the square cell: outputs . . . 42
Table4.3 Non-pure shear test for the square cell: outputs (case 1) 42
Table4.4 Non-pure shear test for the square cell: outputs (case 2) 44
Table4.5 Tension test along direction x_1 for the rhomboidal cell: outputs 45
Table4.6 Tension test along direction x_2 for the rhomboidal cell: outputs 46
Table4.7 Non-pure shear test for the rhomboidal cell: outputs 47

Chapter 1

Introduction

This first chapter is devoted, in a first part, to a general introduction about anisotropic locally-resonant metamaterials within the concept of wave polarization and then to specific applications presented in literature. In a second part, the aims of the work will be described and in a third and last part, an outline of the thesis contents will be given.

1.1 Anisotropy of locally resonant materials and mode conversion applications

Metamaterials are artificial composites made by a micro-structure that gives them special properties which are difficult to find in the usual natural materials. These specific properties can be achieved from particular configurations of the geometry of the structure, defined using sufficiently small elements which are periodically arranged. The chemical composition of the components of these artificial composites are not so relevant for the presence of these special properties. In order to get the desired properties, a suitable design of the micro-structure have to be developed.

In mechanics, some applications are related to phononic crystals that are metamaterials made using a periodic structure that allows them to act as a filter to the propagation of elastic waves at specific frequency ranges. These frequency bands, in which waves cannot propagate without attenuation, are called band gaps. An interesting property, used for the prediction of these special frequency ranges, is the effective dynamic mass density which becomes negative in these frequency intervals. The intervals of frequency, in which waves are attenuated, can have different applications in vibration isolation and impact absorption ([1],[2],[3] and [4]). The band gaps, with reference to locally-resonant metamaterials, are generated by a mechanism in which energy is trapped in parts of the structure that resonate. Some examples that show how this category of metamaterials work can be found in [5] and [6]. As mentioned in [5], locally-resonant acoustic metamaterials (LRAMs) have recently attracted a great interest for their dynamic behaviour, characterized by band gaps at relatively low frequencies. In artificial LRAMs, the opening and closure frequencies of the band gaps depend on the frequency of the resonators and, thus, they can provide a wave attenuation at relatively low frequency, e.g., in the

range of some kHz, without requiring large dimensions as it occurs for phononic crystals. LRAMs are usually composed by a stiff matrix with a periodic repetition of small heavy resonators trapped in a soft coating. When the frequency is near to the local resonance frequency of the resonating mass, LRAMs absorb and store the kinetic energy. Moreover, they provide a damping mechanism without any material dissipation. As mentioned in [6], the local resonance phenomenon is independent from the lattice dimensions.

An important focus must be done on the concept of effective dynamic mass density which is a frequency-dependent property useful for studying the dynamic behaviour of locally-resonant metamaterials. In order to obtain the effective dynamic mass density tensor, the two scale asymptotic homogenization technique can be used. As mentioned in [7], the two scale homogenization method was firstly proposed in [8] for binary elastic composite materials, and then implemented in different directions. The further development of the method with three-component composite materials was defined in [9]. Another interesting works extend the approach also for a periodic arrangement of locally resonant inclusions ([10], [11]). In particular, the homogenized media can be represented by an equivalent mass density that is frequency-dependent and which can become negative close to the resonant frequencies of the inclusions, thus defining the band gaps. The asymptotic procedure for the two scale homogenization was firstly proposed in [12] in order to overcome the hypothesis of wavelength much higher than the characteristic lattice length. This new technique was also implemented in [13] to study the wave propagation through an elastic media made of periodic arrangements of inclusions. As shown in [14], the macroscopic behaviour of periodically heterogeneous linearly elastic bodies can be described by asymptotic homogenization which is a diffuse mathematical tool. This technique is able to define the homogenized properties of a periodic media by means of the so-called cell problems. In some cases, analytical solutions can be achieved but this method can be also numerically implemented by the available finite element software. After setting specific hypotheses on the geometry and on the materials which compose the unit cell, this tool provides predictions of the band gaps, through a frequency-dependent effective mass density. The theoretical framework of this technique is developed in chapter 3. As explained in [7], the study of wave propagation in locally-resonant metamaterials can be defined in different ways. An alternative approach takes into account the wave propagation through an infinite periodic media and implements the Bloch-Floquet analysis to achieve the dispersion surfaces and to identify the band gaps [15]. In order to apply the Bloch-Floquet principles, a finite element analysis can be performed considering a unit cell of the periodic material with the Bloch-Floquet boundary conditions ([16], [17]). As shown in chapter 4, the band gaps obtained with these two different methods are in good agreement from a qualitative point of view. However, the are few studies which discuss the comparison between these two methods, except in [18]. As mentioned in [7], the principal advantage of the homogenization technique with respect to the Bloch-Floquet analysis is that it can provide analytical predictions of the band gaps and, in this way, the method is very suitable in the design of the metamaterial. In particular, the homogenization approach can be useful also for opening a way to the optimization of the metamaterial because it provides information about the

dependence of the band gaps on the geometry and on the mechanical properties of the components. It is important also to remind that the homogenization approach is strictly governed by specific hypothesis which can affect the range of application.

As explained in [19], for spherical homogeneous inclusions, the dynamic mass density is equal in any direction of the motion, while for cylindrical inclusions, it has components which are not the same for the motion along the axis of the cylinder. In the latter case, the dynamic mass density is therefore anisotropic. Another case, in which the dynamic mass density is anisotropic, is related to composites with elliptic fibers. The anisotropy can be also achieved in the case of a micro-structure made of elastic beams or plates; in particular, the anisotropic effect, for example, can be due to an higher stiffness for the motion along the direction of the beam than for the motion along the transversal direction. In the present work, for the discrete model (subsection 2.3.2), the anisotropic effect on the dynamic mass is obtained though the presence of different spring stiffnesses along two different directions in a "mass-in-mass"-spring lattice, while for the continuum model (chapters 3 and 4), the anisotropic effect on the dynamic mass density is provided by the presence of an eccentric cylindrical fiber. Making reference to an in-plane wave propagation, this anisotropic effect provides an effective dynamic mass density tensor in which the two principal components have different sign in specific frequency intervals. These special frequency intervals, predicted by the two scale asymptotic homogenization technique, are called polarization bands.

In order to understand the physical meaning of polarization, we can refer to [20], in which polarization of light is described. The latter is the optical phenomenon occuring when oscillations of an electric field vector within an electromagnetic wave become restricted to a single plane. This polarization plane is obtained by the direction of propagation and the direction of the electric field oscillations. In general, light is unpolarized and possesses a random polarization in which the electric field vector oscillates in random directions that are perpendicular to the direction of propagation. From a practical point of view, the light waves are not aligned in any specific direction but they continuously change it. In order to give a specific polarization direction to light waves, the light has to pass through a polarizer. There are different types of polarization such as linear and circular. Linearly polarized light is such that the electric field vector oscillates in a single plane which is perpendicular to the direction of propagation. Light can be linearly polarized with a polarizer that acts as a filter which gives a preferential polarization direction to light waves and, in the meanwhile, blocks the others. Circularly polarized light occurs when the electric field vector rotates, around the direction of propagation within a constant amplitude and frequency. This type of polarization can be generated by passing linearly polarized light through a quarter-wave plate. These two types of polarization for light are shown in figure 1.1.

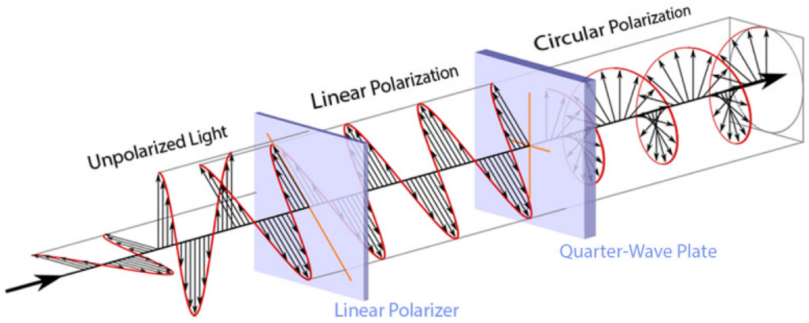

Figure 1.1. Unpolarized light, possessing random polarization, passes through a linear polarizer to create linearly polarized light, then passes through a quarter-wave plate to create circularly polarized light (from [20]).

Another physical interpretation for the concept of polarization is related to seismic waves. The body waves can be distinguished in two main categories that are the compressional or P-waves and the shear or S-waves. For P-waves, the propagation direction and the ground motion direction are parallel, while for S-waves, these directions are orthogonal, as shown in figure 1.2.

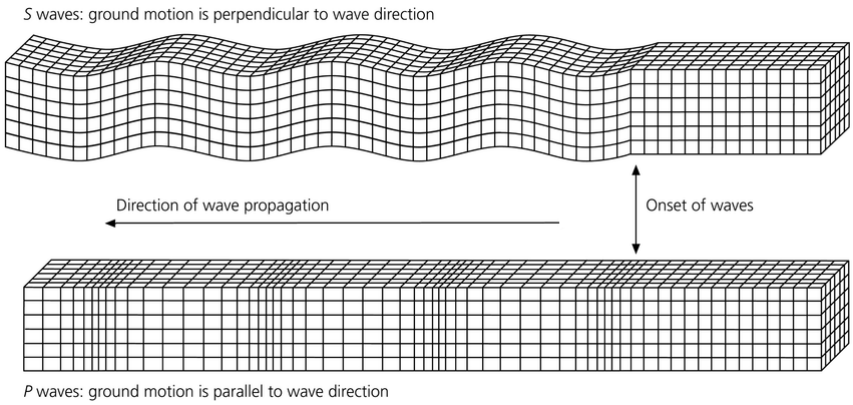

Figure 1.2. Illustration of ground motions produced by compressional or P-waves and shear or S-waves (from [21]).

The ground motion direction can be also seen as a particle motion direction. The latter, from a physical point of view, represents the orientation of the particle oscillations, which is the polarization direction.

With reference to the present work, the discussion about polarization directions will be developed in chapters 3 and 4, while the role of polarization bands in terms of transmission analysis will be developed in chapter 5.

As mentioned in [22], in correspondence of the band gaps, the transmission of elastic waves is impeded. In [22], it is reported the numerical linear elastic transmission spectrum, for the periodic material taken into consideration and for a specific propagation path, superimposed to the band gaps. It is possible to notice that the

transmission curve shows attenuated peaks inside the band gaps. In the present work, in chapter 5, we perform several numerical transmission analyses for specific periodic arrays and we discuss the role of the polarization bands predicted by the two scale asymptotic homogenization technique.

Anisotropic locally-resonant metamaterials can be designed in order to achieve mode conversion from longitudinal to shear waves, with some interesting applications. As explained in [23], both longitudinal and shear modes occur in elastic solids. During elastic wave propagation in anisotropic media, longitudinal and transverse particle motions can be coupled and transformed. For example, a longitudinal wave can be transformed in a longitudinal and S wave through an anisotropic mode-coupled layer, as shown in figure 1.3.

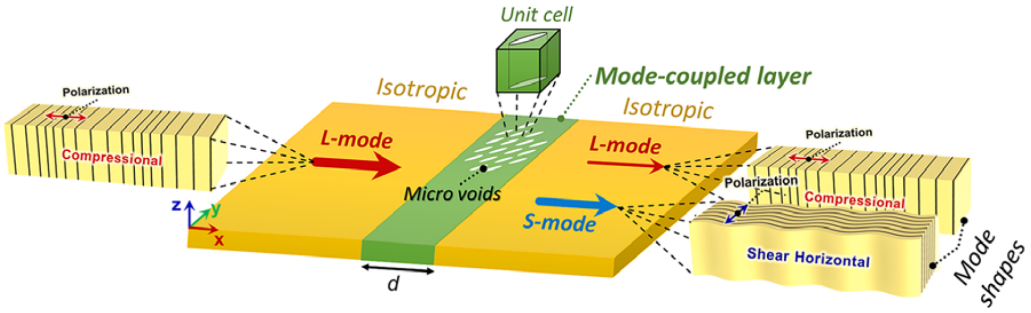

Figure 1.3. An illustration of a mode-coupled layer surrounded by an isotropic medium. The incident longitudinal wave can be converted to the shear wave as it propagates through the mode-coupled layer (from [23]).

With reference to figure 1.3, the mode-coupled layer is an elastic metamaterial with slender, tilted microvoids inserted in an isotropic media. After the propagation through this mode-coupled layer, there is a partial conversion from longitudinal to shear mode, due to the presence of the anisotropic media.

As shown in [24], the use of shear waves has a great potential in civil engineering applications, such as in non-destructive testing methods. The latter are useful for detecting horizontal cracking or delamination, spalling, map-cracking at the mid-depth of concrete pavement slabs, concrete cracks, delamination in bridge columns and shallow concrete cover in bridge piers. Ultrasonic shear-wave tomography overcomes the limitation of traditional ultrasonic testing which is the high scattering of the transmitted pulses due to the heterogeneity of concrete. Another advantage is the reduction of operating time because the traditional transducers have to be coupled to the surface of concrete pavement using a coupling gel and this procedure usually takes much more time. The principle of the ultrasonic shear-wave tomography system is shown in figure 1.4.

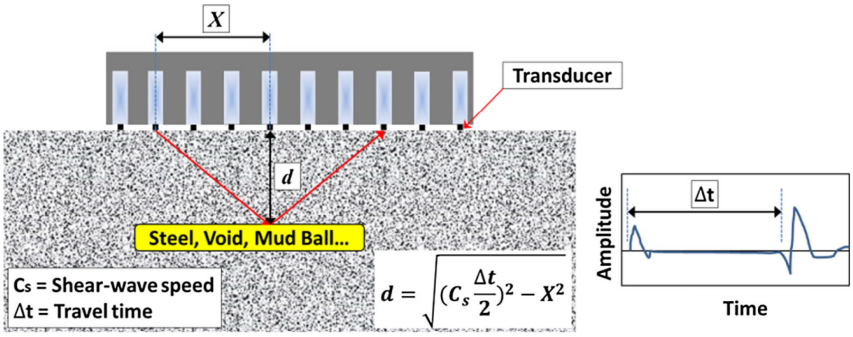

Figure 1.4. The principle of the ultrasonic shear-wave tomography system (from [24]).

The shear waves are generated by exciting a piezoelectric material with a short-burst, high-amplitude pulse which has high voltage and current. The principle is based on the ultrasonic pulse-echo method with the use of transmitting and receiving transducers. In particular, one transducer sends a stress-wave pulse and a second one receives the reflected pulse. The travel time Δt from the beginning of the pulse to the arrival of the echo can be measured, the shear wave velocity C_s is known, the distance X from the transmitter to the receiver is also known and, thus, the depth d of the reflecting interface can be computed using the equation shown in figure 1.4. Moreover, figure 1.5 a) shows the testing instrument on a cracked concrete bridge column, whereas figure 1.5 b) shows the analysis image in which the delamination cracks are displayed at the depth of 60–90 mm from the surface.

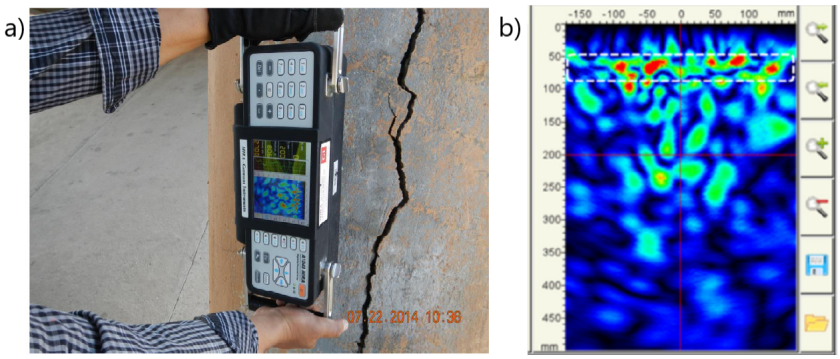

Figure 1.5. a) Ultrasonic shear-wave tomography instrument b) Analysis image (from [24]).

As mentioned in [25], non-destructive testing by ultrasonic shear waves is useful also for investigation of mechanical behaviour of materials. In that specific study, it was possible to provide the characterization of acoustic properties for sandy sediments. In particular, transducers are used in order to transmit and receive shear waves obtained by reflection mode conversion. The analysis of the amplitude responses and their spectrum can provide information on vibrations in a very low range frequency of 1–10 Hz. This application can be useful for the study of physical properties related to soils but also for detecting the dynamic characteristics of the machine structures perturbed by static or dynamic forces. For example, one of the ap-

plications allows the characterization of the acoustic impedance for the sand sediment.

As mentioned in [26], the ultrasonic shear waves can be very efficient to predict fatigue state in pressurized components, such as pipes in nuclear power generation plants or in other industrial applications. These steel pipes are usually subjected to important cyclic loadings and they can be very sensitive to fatigue damage. The prediction of fatigue state for these pipes is very important because failure can suddenly occur but also because their monitoring and replacement costs could be very high. Ultrasonic waves can be employed to detect the presence of fatigue damage. As shown in [27],[28] and [29], it is possible to correlate the evolution of ultrasonic velocity and attenuation within the fatigue state of a component. As explained in [26], augmenting the sensitivity of a through-thickness wave measurement to the changes in velocity and attenuation is always desirable because larger changes provide more confidence for the prediction of the fatigue state. Through-thickness shear wave measurements can be useful in this sense, because they can increase the changes in velocity since they spend much more time in the fatigue spots. The opportunity of using shear waves provides an improvement of the measurements, in terms of sensitivity to fatigue, due to two substantial aspects:

- Shear waves are more sensitive to the presence of a fatigue zone. [30],[31] and [32] have shown that shear waves are much better at causing dislocations to vibrate.
- EMATs with high repeatability for shear waves have recently become available, within an improved sensitivity to fatigue and the possibility to provide an high-quality scanning area.

The longitudinal-to-shear mode conversion has great potential also in medical ultrasonic applications. As explained in [33], clinical applications of longitudinal and shear mode ultrasound propagation within the human skull bone have been provided for the treatment of tumors, targeted drug delivery, thrombolytic stroke treatment, blood flow imaging and brain imaging. Experimental investigations with isotropic phantom materials and ex vivo human skulls verified that a shear mode propagation scenario is less distorted with respect to the longitudinal one. The crucial advantage consists on providing an higher resolution for the imaging applications. This higher resolution provided by the shear mode propagation is due to the lower velocity of shear waves with respect to longitudinal waves. As shown in [34], the skull's shear wave velocity provides also less phase alteration than its longitudinal counterpart. Also in this work, practical demonstrations of the phenomena and numerical predictions are developed with plastic phantoms and using an ex vivo human skull. Since the shear wave experiences a reduced phase shift, a more simplified non-invasive trans-skull focusing method can be developed and it can be extended to larger regions in the brain. Another interesting information are mentioned in [35], in which they discover that the longitudinal-to-shear mode conversion, which occurs at the interface between elastic bone and tissues, can be used for the distorsion reduction in imaging applications by increasing the incidence angle between the ultrasound beam and the skull.

1.2 Aims of the work

The focus of this thesis is on the study of wave propagation in anisotropic locally-resonant metamaterials and on the possibility to control wave polarization. Specific design of this particular category of metamaterials allows to obtain band gaps in the dispersion plot where all waves are attenuated and other intervals, called polarization bands, where only propagation of waves with specific polarization is allowed for. The focus is related to wave polarization within the polarization bands that can be obtained by the metamaterial's anisotropy. One of the most important aims of this work consists on studying the effect of the anisotropic equivalent mass on band gaps and polarization bands. The study of the eigenvalues of the equivalent mass can predict band gaps, polarization bands and can identify the effects of several geometric parameters on these special frequency ranges. Thus, another purpose is to analyze the effects of geometric parameters related to the metamaterial taken into consideration and study the influence of them on band gaps and polarization bands. Anisotropic locally-resonant metamaterials can be designed in order to obtain the mode conversion from longitudinal to shear waves inside the polarization bands. Mode conversion can be achieved in the polarization bands predicted by the two-scale asymptotic homogenization technique. This can be developed through specific transmission analysis. For obtaining mode conversion, a proper geometric configuration of the metamaterial will be adopted. Shear waves, obtained by mode conversion, are very useful in a great number of real engineering applications. The latters can be industrial, medical but also for detecting mechanical behaviour of materials in the civil engineering field.

1.3 Outline of the thesis

After this first chapter, the present thesis is divided into other four chapters.

The second chapter is devoted, in a first part, to a general description of elastic wave propagation in homogeneous media and periodic metamaterials. In a second part, examples of discrete periodic metamaterials are developed in order to study wave propagation and obtain the dispersion curves. An important step developed in this chapter is the description of the effective negative mass that can be useful for the prediction of band gaps and polarization bands. The latter, with reference to the 2D "mass-in-mass"-spring lattice, are due to the use of different spring stiffnesses along two different directions that provides an anisotropic effect to the system.

In the third chapter, the theoretical framework of the two-scale asymptotic homogenization procedure is developed. This technique is defined for a periodic locally-resonant metamaterial made by a rigid eccentric fiber with a soft coating embedded in a stiff matrix. In particular, this procedure is numerically implemented in order to obtain the equivalent frequency-dependent mass tensor useful for the prediction of band gaps and polarization bands.

The fourth chapter is the core of the work since it contains the evaluation of the

homogenized properties obtained numerically. The latter are the effective stiffness for two different geometric configuration of the matrix and the effective mass density for perfectly centered and eccentric fiber. Furthermore, a band gaps prediction is developed by Bloch-Floquet analysis to obtain the dispersion curves for the two different geometric shapes of the matrix. This predictions are defined for the perfectly centered fiber and also for the eccentric one. Another important section of this chapter is devoted to the effective dispersion properties. Phase velocities, polarization and propagation directions are shown in polar diagrams in order to observe how they change in different polarization bands and within different geometrical configurations of the matrix. The last section consists on the analysis of the effects of geometric parameters related to the metamaterial and on studying the influence of them on band gaps and polarization bands.

The fifth chapter is devoted to transmission analysis for three different types of fiber eccentricity. In particular, the case in which the fiber is eccentric with an angle of 45° with respect to the horizontal axis of the plane is considered in detail. In this case, mode conversion can be detected in the polarization bands which are numerically predicted by the homogenization procedure.

At the end of the elaborate, a final chapter related to conclusions and further developments is presented.

Chapter 2

Elastic wave propagation in metamaterials

In this chapter, elastic wave propagation will be described for homogeneous media and also for periodic metamaterials. In the section related to periodic metamaterials, the focus will be done on the Bloch-Floquet analysis. Moreover, the last section of this chapter will be devoted to examples of discrete models which can be useful for understanding the concept of effective negative mass for the prediction of band gaps and polarization band gaps. The theoretical references are related to [36].

2.1 Wave propagation in homogeneous media

Let us consider a three-dimensional media made of an isotropic homogeneous linear-elastic material, as the one which is shown in figure 2.1.

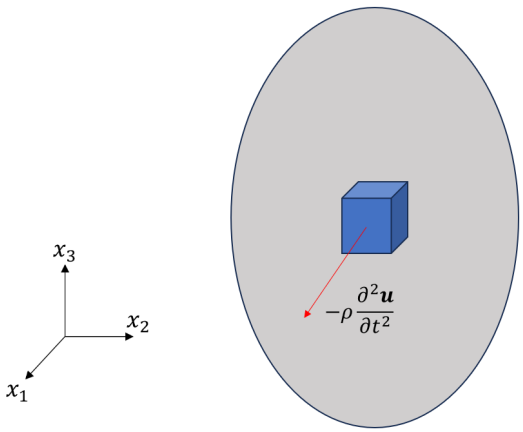

Figure 2.1. Three-dimensional homogeneous media

The dynamic equilibrium equation of the media is:

$$\nabla \cdot \boldsymbol{\sigma} - \rho \frac{\partial^2 \boldsymbol{u}}{\partial t^2} = \mathbf{0} \tag{2.1}$$

with $\boldsymbol{u}$ is the displacement field, ρ is the mass density and $\boldsymbol{\sigma}$ is the Cauchy's stress tensor. The latter, for a linear-elastic isotropic material can be expressed as:

$$\boldsymbol{\sigma} = 2\mu\boldsymbol{\varepsilon} + \lambda\varepsilon_{vol}\boldsymbol{I} \tag{2.2}$$

where λ, μ are the Lame's costants of the material, $\boldsymbol{\varepsilon}$ is the small strain tensor given by:

$$\boldsymbol{\varepsilon} = \frac{1}{2}(\nabla\boldsymbol{u} + \nabla\boldsymbol{u}^T) \tag{2.3}$$

while ε_{vol} is the volumetric strain, i.e., the trace of $\boldsymbol{\varepsilon}$.

Replacing (2.2) and (2.3) in (2.1), one obtains the Navier's equation:

$$(\lambda + \mu)\nabla\nabla\cdot\boldsymbol{u} + \mu\nabla^2\boldsymbol{u} - \rho\frac{\partial^2\boldsymbol{u}}{\partial t^2} = \boldsymbol{0} \tag{2.4}$$

Applying the gradient on both sides of (2.4), one obtains:

$$(\lambda + 2\mu)\nabla^2\varepsilon_{vol} = \rho\frac{\partial^2\varepsilon_{vol}}{\partial t^2} \tag{2.5}$$

which can be recognized as a classical wave equation. In particular, it is possible to observe that the volumetric strain propagates at a velocity c_1:

$$c_1 = \sqrt{\frac{\lambda + 2\mu}{\rho}} \tag{2.6}$$

Thus, c_1 is the velocity of propagation of pressure (P) waves which provokes only a volumetric deformation of the media. The P-waves are also called longitudinal waves.

If no volumetric deformation occurs, i.e, $\nabla\cdot\boldsymbol{u} = \boldsymbol{0}$, equation (2.4) reads:

$$\mu\nabla^2\boldsymbol{u} - \rho\frac{\partial^2\boldsymbol{u}}{\partial t^2} = \boldsymbol{0} \tag{2.7}$$

which is the wave equation that governs the propagation of isochoric waves. The latters, called shear (S) waves propagate at a velocity c_2:

$$c_2 = \sqrt{\frac{\mu}{\rho}} \tag{2.8}$$

It is important to note that the longitudinal waves' velocity c_1 is always greater than the shear waves' velocity c_2, because the elasticity tensor is positive definite, i.e., $\lambda + 2\mu > 0$ with $\mu > 0$.

Dispersion properties for an homogeneous isotropic elastic media One can search for a solution in the form of a monochromatic wave:

$$\boldsymbol{u}(\boldsymbol{x}, t) = \boldsymbol{p}\exp[\mathrm{i}(\boldsymbol{k}\cdot\boldsymbol{x} - \omega t)] \tag{2.9}$$

where $\boldsymbol{p}$ is the polarization vector, $\mathbf{k}$=k$\mathbf{n}$ is the wavevector, k the wavenumber, $\boldsymbol{n}$ the propagation direction and ω the angular frequency.

Substituting (2.9) in (2.4), it is possible to obtain the dispersion relation:

$$(\boldsymbol{Q} - \rho c^2 \boldsymbol{I}) \cdot \boldsymbol{p} = \mathbf{0} \tag{2.10}$$

where $c = \omega/k$ is the phase velocity and $\boldsymbol{Q}(\boldsymbol{n})$ is the acoustic tensor obtained as:

$$\boldsymbol{Q}(\boldsymbol{n}) = \boldsymbol{n} \cdot \mathbb{D} \cdot \boldsymbol{n} \tag{2.11}$$

where $\mathbb{D}$ is the fourth-order elastic stiffness tensor depending on Lame's costants and it is defined as:

$$\mathbb{D} = 2\mu\mathbb{I} + \lambda \boldsymbol{I} \otimes \boldsymbol{I} \tag{2.12}$$

$\boldsymbol{Q}(\boldsymbol{n})$ is a real second order symmetric tensor due to the symmetries of $\mathbb{D}$ (2.12) and it is also positive definite.

Equation (2.10) can be recognized as a standard eigenvalue problem. Since $\boldsymbol{Q}(\boldsymbol{n})$ is real, symmetric and positive definite, equation (2.10) defines three real eigenvalues c_1^2, c_2^2 and c_3^2 associated to the corresponding real eigenvectors $\boldsymbol{p}_1$, $\boldsymbol{p}_2$ and $\boldsymbol{p}_3$.

For an homogeneous isotropic media, c_1, c_2 are defined in (2.6) and (2.8) respectively and $c_3 = c_2$. The corresponding eigenvectors represent the associated polarization directions; in particular, at the phase velocity c_2, polarization and propagation directions are orthogonal, while at the phase velocity c_1, these directions are parallel. When there is orthogonality between these directions, the waves are defined as shear waves (S-waves), whereas when they are parallel, the waves are longitudinal (P-waves).

In a 2D problem, only c_1 and c_2 can be defined and they are represented in adimensional form with respect to $\sqrt{E/\rho}$ in figure 2.2. E is the Young's modulus and it can be defined through the Lame's costants:

$$E = \frac{\mu(3\lambda + 2\mu)}{\lambda + \mu} \tag{2.13}$$

Since c_1 and c_2 are normalized with respect to $\sqrt{E/\rho}$, the Poisson's coefficient ν is the sole parameter that influences the solution. ν is defined as:

$$\nu = \frac{\lambda}{2(\lambda + \mu)} \tag{2.14}$$

With reference to figure 2.2, since the stiffness tensor is isotropic, the wave velocities do not depend on $\mathbf{n}$ and so they are represented by two circumferences. It can be noticed that the velocity c_1, represented by the bigger circumference, increases augmenting the value of ν. On the other side, the velocity c_2, represented by the smaller circumference, decreases augmenting the value of ν.

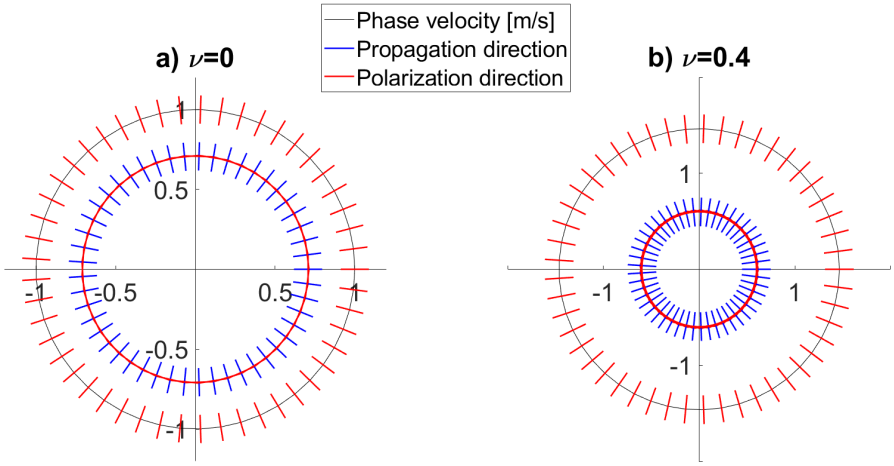

Figure 2.2. Polar diagrams of normalized phase velocities with respect to propagation directions (blue) and with superposed polarization directions (red)

With reference to figure 2.2, the propagation directions are always radial with respect to the polar diagrams. Moreover, at the bigger phase velocity c_1 (P-waves), the polarization and propagation directions are parallel, whereas at the smaller phase velocity c_2 (S-waves), polarization and propagation directions are orthogonal.

2.2 Wave propagation in periodic metamaterials

We consider now a three dimensional periodic body, i.e., invariant with respect to a set of translations defined by the translation vectors:

$$\boldsymbol{R} = n_1\boldsymbol{a}_1 + n_2\boldsymbol{a}_2 + n_3\boldsymbol{a}_3 \tag{2.15}$$

where n_1, n_2, n_3 are integer numbers and $\boldsymbol{a}_1$, $\boldsymbol{a}_2$, $\boldsymbol{a}_3$ are the three non-complanar vectors, called primitive vectors. The set of points defined by (2.25) is called Bravais lattice of the periodic body. With reference to [36], some examples of primitive Bravais lattices are shown in figure 2.3.

Since the considered body is periodic, it can be constructed by the repetition of a unit cell by means of the translations defined in equation (2.25). The smallest cell which can reproduce the entire space without any overlap is called primitive cell.

Among all the primitive cells, only one can preserves all the symmetries of the lattice. This cell is called Wigner-Seitz cell and it is also defined as the locus of points which are the closest to one point of the lattice.

Due to the periodicity of the considered body, each associated property f must have the same periodicity of the Bravais lattice, such that:

$$f(\boldsymbol{x} + \boldsymbol{R}) = f(\boldsymbol{x}) \tag{2.16}$$

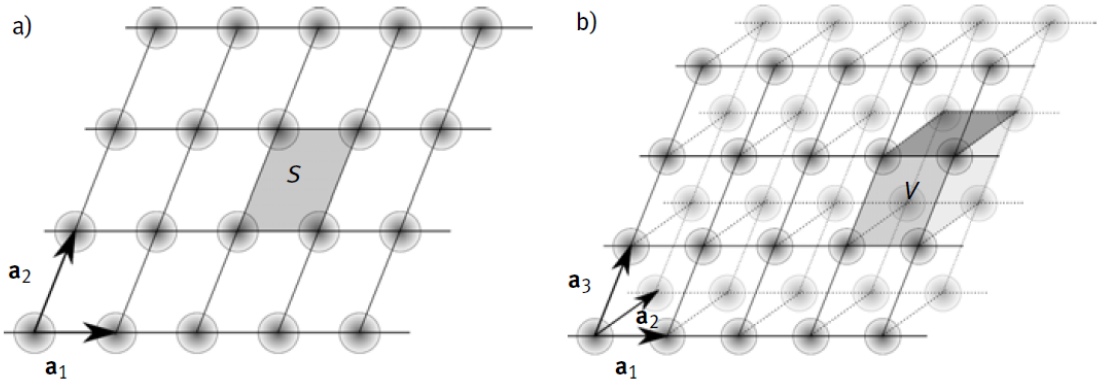

Figure 2.3. a) 2D b) 3D Primitive Bravais lattices, from [36]

and this is valid for any integer numbers n_1, n_2 and n_3.

Since the body is periodic, f($\mathbf{x}$) can be written in Fourier series as:

$$f(\boldsymbol{x}) = \sum_{\boldsymbol{K}} \tilde{f}_{\boldsymbol{K}} \exp(\mathrm{i}\boldsymbol{K} \cdot \boldsymbol{x}) \tag{2.17}$$

where $\tilde{f}_{\boldsymbol{K}}$ are the Fourier coefficients of f with respect to the following vectors:

$$\boldsymbol{K} = \beta_1 \boldsymbol{b}_1 + \beta_2 \boldsymbol{b}_2 + \beta_3 \boldsymbol{b}_3 \tag{2.18}$$

where β_1, β_2, β_3 are real numbers and $\boldsymbol{b}_1$, $\boldsymbol{b}_2$, $\boldsymbol{b}_3$ are the basis of the reciprocal lattice. The basis vectors are obtained from a condition that reads:

$$\boldsymbol{a}_i \cdot \boldsymbol{b}_j = 2\pi\delta_{ij} \tag{2.19}$$

where δ_{ij} is the Kronecker delta. It is possible to prove that the vectors $\boldsymbol{b}_1$, $\boldsymbol{b}_2$, $\boldsymbol{b}_3$ are not coplanar, which means that the set of points defined in (2.18) construct a Bravais lattice, called reciprocal lattice. The latter lives in the space of the wavevectors.

The Wigner-Seitz cell of the reciprocal lattice is called First Brillouin Zone (FBZ) and the smallest portion of the FBZ, which can be achieved exploiting all the symmetries of the lattice, is called Irreducible Brillouin Zone (IBZ). For example, in a 2D plane, a metamaterial with Wigner-Seitz primitive square cell of lenght L has a reciprocal cell which is also a square but with side 2π/L (figure 2.4). With reference to figure 2.4 c), the FBZ is the square of side 2π/L highlighted in black and the IBZ is the triangle depicted in red.

The propagation of elastic waves in a three dimensional periodic domain, characterized by the repetition of a unit cell, can start from equations (2.1) and (2.3) but considering $\boldsymbol{\sigma}$ as:

$$\boldsymbol{\sigma} = \mathbb{D} : \boldsymbol{\varepsilon} \tag{2.20}$$

The elastic stiffness tensor $\mathbb{D}(\boldsymbol{x})$ and the mass density $\rho(\boldsymbol{x})$ of the body are periodic and satisfy the equation (2.16).

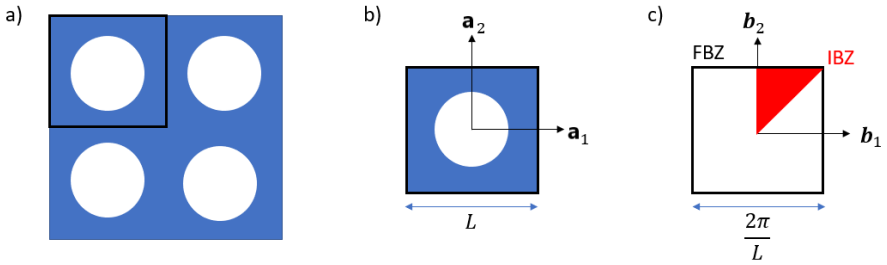

Figure 2.4. a) Metamaterial with hollowed square unit cells b) Wigner-Seitz primitive cell c) FBZ and IBZ

We assume the separation of variables for the displacement field:

$$\boldsymbol{u}(\boldsymbol{x}, t) = \boldsymbol{u}(\boldsymbol{x}) \exp(-\mathrm{i}\omega t) \tag{2.21}$$

where $\boldsymbol{u}(\boldsymbol{x})$ must satisfy the Helmholtz equation:

$$\nabla \cdot [\mathbb{D} : \boldsymbol{\varepsilon}(\boldsymbol{u})] + \rho\omega^2 \boldsymbol{u} = \mathbf{0} \tag{2.22}$$

For a periodic media, according to the Bloch's theorem [36], the eigenmodes of (2.22) are Bloch waves of the form:

$$\boldsymbol{u}(\boldsymbol{x}) = \exp(-\mathrm{i}\boldsymbol{k} \cdot \boldsymbol{x})\tilde{\boldsymbol{u}}(\boldsymbol{x}) \tag{2.23}$$

where $\boldsymbol{k}$ is the wavevector and $\tilde{\boldsymbol{u}}(\boldsymbol{x})$ is a vector field which has the same periodicity of the Bravais lattice, i.e., satisfies the condition:

$$\tilde{\boldsymbol{u}}(\boldsymbol{x} + \boldsymbol{R}) = \tilde{\boldsymbol{u}}(\boldsymbol{x}) \tag{2.24}$$

Considering a specific unit cell of the body, for each point **x'** in the region occupied by the body, a unique point **x** in the unit cell and a triplet n_1, n_2, n_3 exist such that $\boldsymbol{x'} = \boldsymbol{x} + \boldsymbol{R}$. Thus, from (2.23) one has:

$$\boldsymbol{u}(\boldsymbol{x'}) = \exp(-\mathrm{i}\boldsymbol{k} \cdot \boldsymbol{R})\boldsymbol{u}(\boldsymbol{x}) \tag{2.25}$$

This means that the solution of (2.22) can be found only within a single unit cell, while in the whole domain, it can be reconstructed through (2.25). On the opposite sides of the unit cell must be prescribed the so-called Bloch-Floquet's boundary conditions, through condition (2.25). We finally obtain the so-called Bloch-Floquet's problem, in which one has to determine the frequencies ω and the wavevector $\boldsymbol{k}$ such that:

$$\begin{cases} \nabla \cdot [\mathbb{D} : \boldsymbol{\varepsilon}(\boldsymbol{u})] + \rho\omega^2 \boldsymbol{u} = \mathbf{0} & \text{where } \boldsymbol{s} = \mathbb{D} : \boldsymbol{\varepsilon}(\boldsymbol{u}) \text{ in the unit cell} \\ \boldsymbol{u}(\boldsymbol{x} + \boldsymbol{a}_i) = \exp(-\mathrm{i}\boldsymbol{k} \cdot \boldsymbol{a}_i)\boldsymbol{u}(\boldsymbol{x}) & \text{on the boundaries of the unit cell} \\ \boldsymbol{N} \cdot \boldsymbol{s}(\boldsymbol{x} + \boldsymbol{a}_i) = \boldsymbol{N} \exp(-\mathrm{i}\boldsymbol{k} \cdot \boldsymbol{a}_i)\boldsymbol{s}(\boldsymbol{x}) & \text{on the boundaries of the unit cell} \end{cases} \tag{2.26}$$

has no trivial solutions. $\boldsymbol{N}$ is the unit outer normal and the considered boundaries are the opposite sides of the unit cell.

Due to periodicity and to the symmetries of the unit cell, the wavevector $\boldsymbol{k}$ can be defined by considering only the IBZ but, usually, the discretization is done along the boundaries of the IBZ ($\Gamma X M \Gamma$), as shown in figure 2.5.

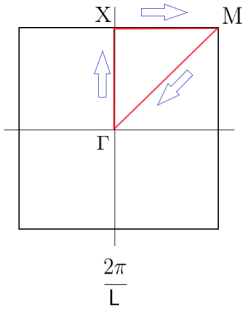

Figure 2.5. Boundaries of the IBZ (red) for a square reciprocal Wigner-Seitz cell

The components of the wave vector, in the vertices of the IBZ, are:

$$\begin{cases} \Gamma : (k_1 = 0, k_2 = 0) \\ X : (k_1 = 0, k_2 = \frac{\pi}{L}) \\ M : (k_1 = \frac{\pi}{L}, k_2 = \frac{\pi}{L}) \end{cases} \tag{2.27}$$

Another case is defined in figure 2.6 that shows the FBZ related to the rhomboidal unit cell which is a regular hexagon of side $4\pi/3d_1$, while the IBZ is the triangle of vertices Γ, X and M.

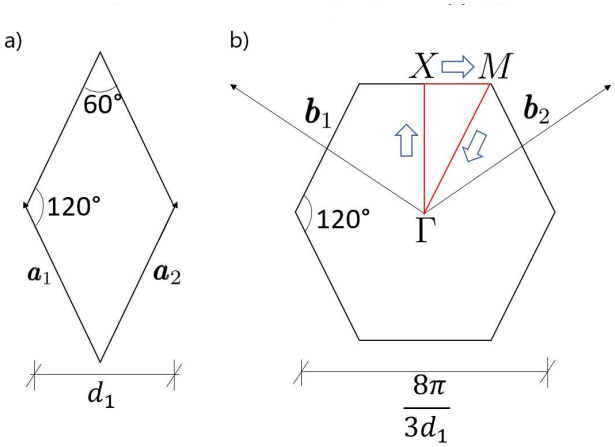

Figure 2.6. Rhomboidal unit cell: a) Wigner-Seitz primitive rhomboidal cell b) reciprocal hexagonal cell (FBZ) with the boundaries of the IBZ depicted in red

With reference to figure 2.6, the primitive vectors of the direct lattice are:

$$\begin{cases} \boldsymbol{a}_1 = d_1(-\frac{1}{2}, \frac{\sqrt{3}}{2}) \\ \boldsymbol{a}_2 = d_1(\frac{1}{2}, \frac{\sqrt{3}}{2}) \end{cases} \tag{2.28}$$

where d_1 is the horizontal diagonal of the rhombus cell. Through (2.19), one can compute the reciprocal basis, which reads:

$$\begin{cases} \boldsymbol{b}_1 = \frac{2\pi}{d_1}(-1, \frac{\sqrt{3}}{3}) \\ \boldsymbol{b}_2 = \frac{2\pi}{d_1}(1, \frac{\sqrt{3}}{3}) \end{cases} \tag{2.29}$$

With reference to figure 2.6, the wavevector's components assume different values in the vertices of the IBZ:

$$\begin{cases} \Gamma : (k_1 = 0, k_2 = 0) \\ X : (k_1 = \frac{\pi}{d_1}, k_2 = \frac{\pi}{d_1}) \\ M : (k_1 = \frac{4\pi}{3d_1}, k_2 = \frac{2\pi}{3d_1}) \end{cases} \tag{2.30}$$

The approach that can be used for solving problem (2.26) consists on fixing a real wavevector $\overline{\boldsymbol{k}}$ and ,through (2.26), determining the frequencies $\omega(\overline{\boldsymbol{k}})$. Throughout the present work, we always refer to this technique which is known as the inverse solution method. The obtained results can be:

- frequency intervals in which the solution exists and they are called pass bands
- frequency intervals in which the solution do not exist and they are called band-gaps. In this case, no real wavenumber can satisfy the Bloch-Floquet problem. In these ranges, the wavevector is complex, and in equation (2.23) real exponential terms appear which damped out the solution. This means that the elastic waves cannot propagate without attenuation.

2.3 Examples of discrete periodic metamaterials

2.3.1 1D monoatomic chain

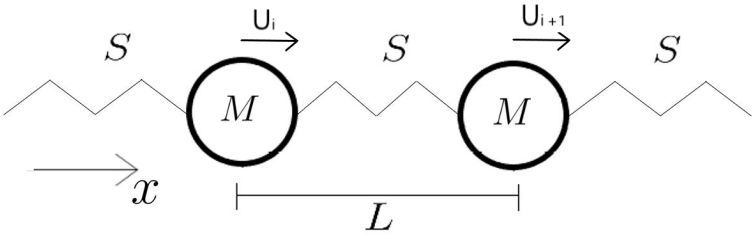

Figure 2.7. 1D monoatomic chain

Let us consider first the simple 1D monoatomic chain of figure 2.7 that can be used to understand the basis for writing the dispersion equations.

The dynamic equilibrium equation can be written along the x-axis as:

$$M\frac{\partial^2 U_i}{\partial t^2} = S(U_{i+1} - U_i) + S(U_{i-1} - U_i) \tag{2.31}$$

where M is the mass, S is the stiffness of the spring, U is the horizontal displacement of the mass and i is the index used to identify a specific mass in the lattice.

The solution in the form of Bloch waves in order to take into account the lattice periodicity is:

$$U(t,x) = \overline{U}(x)\exp(\mathrm{i}(\omega t - kx)) \tag{2.32}$$

where ω is the frequency and k the wave number. Moreover, $\overline{U}(x)$ is periodic of period L.
The displacement of the element i reads:

$$U_i(t) = U(t,x)\delta(x - iL) = \overline{U}(\omega)\exp(\mathrm{i}(\omega t - kiL)) \tag{2.33}$$

where δ is the Dirac delta.

It is possible to substitute the wave solution (2.33) at frequency ω in the dyamic equilibrium equation:

$$(-M\omega^2+2S)\overline{U}\exp(\mathrm{i}(\omega t-kiL)) = SU[\exp(\mathrm{i}(\omega t-k(i+1)L))+\exp(\mathrm{i}(\omega t-k(i-1)L))] \tag{2.34}$$

which can be simplified to:

$$\{(-M\omega^2 + 2S) - S[\exp(-\mathrm{i}kL) + \exp(\mathrm{i}kL)]\}\overline{U} = 0 \tag{2.35}$$

From equation 2.35, non-trivial solutions are obtained for:

$$\omega^2 = \omega^2(k) = \frac{2S}{M}(1 - \cos(kL)) \tag{2.36}$$

that gives the frequency of propagating Bloch's waves as a function of wave number. This is also called dispersion equation from which the dispersion curves are obtained.

2.3.2 2D mass-in-mass chain

In this subsection, a discrete mass-in-mass model will be developed in order to study the wave propagation and to derive the dispersion curves. The concept of effective mass will then be introduced to predict the existence of band gaps and polarization band gaps. As in [37], the discrete model is developed with reference to the lattice shown in figure 2.8.

The "mass-in-mass"–spring lattice, shown in figure 2.8, leads to anisotropic effective mass with two orthogonal principal directions x_1 and x_2. This anisotropic effective mass has an effect on the wave propagation in elastic metamaterials. This important effect is studied in the next sections.

With reference to figure 2.9, the discrete model is a mass-in-mass system in which the internal mass m is joined with the external mass M through two internal springs represented by stiffness s_1 along the direction x_1 and by stiffness s_2 along the direction x_2. This element of the lattice is linked within other elements through the

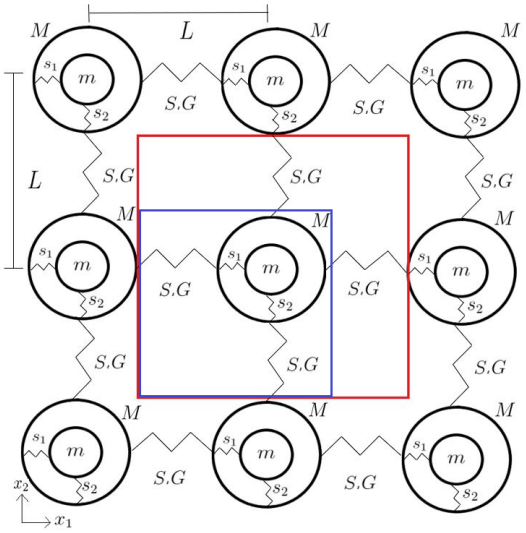

Figure 2.8. 2D "mass-in-mass"-spring lattice: the blue box indicates the unitary cell of side L, while the red one identifies a focus zone useful for the derivation of the dynamic equlibrium equations

external springs represented by axial stiffness S, shear stiffness G along the direction x_1 and x_2. The index i is referred to the horizontal direction x_1, whereas the index j is referred to the vertical direction x_2. The displacement components of mass M are U along x_1 and V along x_2. The displacement components of mass m are u along x_1 and v along x_2.

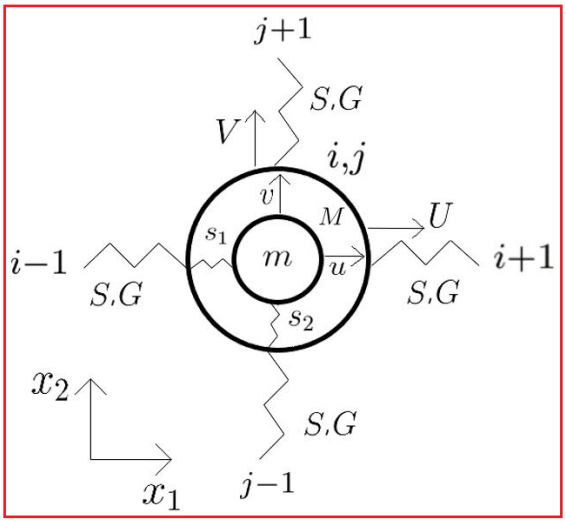

Figure 2.9. 2D "mass-in-mass"-spring lattice: focus zone (red box)

With reference to figure 2.9, the first step is to write the dynamic equilibrium equations of the mass M and m in the element (i, j) along the directions x_1 and x_2. The following equations are obtained:

Mass M along the direction x_1

$$\begin{aligned} M\frac{\partial^2 U_{i,j}}{\partial t^2} =& S(U_{i+1,j} + U_{i-1,j} - 2U_{i,j}) + s_1(u_{i,j} - U_{i,j}) + \\ &+ G(U_{i,j-1} + U_{i,j+1} - 2U_{i,j}) \end{aligned} \tag{2.37}$$

Mass m along the direction x_1

$$m\frac{\partial^2 u_{i,j}}{\partial t^2} = s_1(U_{i,j} - u_{i,j}) \tag{2.38}$$

Mass M along the direction x_2

$$\begin{aligned} M\frac{\partial^2 V_{i,j}}{\partial t^2} =& S(V_{i,j+1} + V_{i,j-1} - 2V_{i,j}) + s_2(v_{i,j} - V_{i,j}) + \\ &+ G(V_{i-1,j} + V_{i+1,j} - 2V_{i,j}) \end{aligned} \tag{2.39}$$

Mass m along the direction x_2

$$m\frac{\partial^2 v_{i,j}}{\partial t^2} = s_2(V_{i,j} - v_{i,j}) \tag{2.40}$$

In order to obtain the dispersion curves, a specific wave vector must be defined:

$$\boldsymbol{k} = \begin{bmatrix} k_1 \\ k_2 \end{bmatrix} \tag{2.41}$$

Due to the periodicity of the lattice, the reciprocal lattice to which the wave vectors belong is also periodic, with periodicity $2\pi/L$. The wavevector variation can hence be limited to the unit cell of the reciprocal lattice (FBZ). Exploiting the symmetries, one can restict the analysis to the boundary of the IBZ, as shown in figure 2.5 by the red line. The vertices of the IBZ are defined as in (2.27) and the components of the wavevector vary along each side. In the following for the discretization, 30 points will be considered along each side of the IBZ.

Bloch waves are used for accounting the lattice periodicity in order to define the waves propagation:

$$U_{i,j} = \overline{U}\exp(\mathsf{i}(\omega t - k_1 iL)) \tag{2.42}$$

$$u_{i,j} = \overline{u}\exp(\mathsf{i}(\omega t - k_1 iL)) \tag{2.43}$$

$$V_{i,j} = \overline{V}\exp(\mathsf{i}(\omega t - k_2 jL)) \tag{2.44}$$

$$v_{i,j} = \overline{v}\exp(\mathsf{i}(\omega t - k_2 jL)) \tag{2.45}$$

Bloch-Floquet's conditions have to be applied to the displacement components of mass M in order to take into account the presence of other cells in the lattice:

$$U_{i+1,j} = U_{i,j}\exp(-\mathsf{i}k_1 L) = \overline{U}\exp(\mathsf{i}(\omega t - k_1 iL))\exp(-\mathsf{i}k_1 L) \tag{2.46}$$

$$U_{i-1,j} = U_{i,j}\exp(\mathrm{i}k_1L) = \overline{U}\exp(\mathrm{i}(\omega t - k_1 iL))\exp(\mathrm{i}k_1L) \tag{2.47}$$

$$U_{i,j+1} = U_{i,j}\exp(-\mathrm{i}k_2L) = \overline{U}\exp(\mathrm{i}(\omega t - k_1 iL))\exp(-\mathrm{i}k_2L) \tag{2.48}$$

$$U_{i,j-1} = U_{i,j}\exp(\mathrm{i}k_2L) = \overline{U}\exp(\mathrm{i}(\omega t - k_1 iL))\exp(\mathrm{i}k_2L) \tag{2.49}$$

$$V_{i+1,j} = V_{i,j}\exp(-\mathrm{i}k_1L) = \overline{V}\exp(\mathrm{i}(\omega t - k_2 jL))\exp(-\mathrm{i}k_1L) \tag{2.50}$$

$$V_{i-1,j} = V_{i,j}\exp(\mathrm{i}k_1L) = \overline{V}\exp(\mathrm{i}(\omega t - k_2 jL))\exp(\mathrm{i}k_1L) \tag{2.51}$$

$$V_{i,j+1} = V_{i,j}\exp(-\mathrm{i}k_2L) = \overline{V}\exp(\mathrm{i}(\omega t - k_2 jL))\exp(-\mathrm{i}k_2L) \tag{2.52}$$

$$V_{i,j-1} = V_{i,j}\exp(\mathrm{i}k_2L) = \overline{V}\exp(\mathrm{i}(\omega t - k_2 jL))\exp(\mathrm{i}k_2L) \tag{2.53}$$

Taking the second partial derivative of equation (2.42) with respect to time and substituting the equations (2.42), (2.43), (2.46), (2.47), (2.48) and (2.49) in equation (2.37), we have:

$$\begin{aligned} -M\omega^2\overline{U}\exp(\mathrm{i}(\omega t - k_1 iL)) =& S\overline{U}\exp(\mathrm{i}(\omega t - k_1 iL))[\exp(-\mathrm{i}k_1L) + \exp(\mathrm{i}k_1L) - 2] + \\ &+ s_1\exp(\mathrm{i}(\omega t - k_1 iL))[\overline{u} - \overline{U}] + \\ &+ G\overline{U}\exp(\mathrm{i}(\omega t - k_1 iL))[\exp(-\mathrm{i}k_2L) + \exp(\mathrm{i}k_2L) - 2] \end{aligned} \tag{2.54}$$

Simplifying and making all the algebraic computations, we obtain:

$$\overline{U}[-M\omega^2 + 2S(1 - \cos(k_1L)) + s_1 + 2G(1 - \cos(k_2L))] + \overline{u}[-s_1] = 0 \tag{2.55}$$

Taking the second partial derivative of equation (2.43) with respect to time, substituting the equations (2.42) and (2.43) into equation (2.38) and, collecting all the terms, we have:

$$-m\omega^2\overline{u}\exp(\mathrm{i}(\omega t - k_1 iL)) = s_1\exp(\mathrm{i}(\omega t - k_1 iL))[\overline{U} - \overline{u}] \tag{2.56}$$

Simplifying equation (2.56), we have:

$$\overline{u}[-m\omega^2 + s_1] + \overline{U}[-s_1] = 0 \tag{2.57}$$

Equations (2.55) and (2.57) can be collected in a 2x2 algebraic system:

$$\begin{bmatrix} -M\omega^2 + 2S(1 - \cos(k_1L)) + s_1 + 2G(1 - \cos(k_2L)) & -s_1 \\ -s_1 & -m\omega^2 + s_1 \end{bmatrix} \begin{bmatrix} \overline{U} \\ \overline{u} \end{bmatrix} = \begin{bmatrix} 0 \\ 0 \end{bmatrix} \tag{2.58}$$

Dispersion equation along the direction x_1 Computing the determinant of the coefficients' matrix in the algebraic system (2.58) and putting it equal to zero, it is possible to obtain the dispersion equation along the direction x_1 in the form:

$$Mm\omega^4 - s_1(M+m)\omega^2 + 2S[s_1 - m\omega^2](1-\cos(k_1L)) + 2G[s_1 - m\omega^2](1-\cos(k_2L)) = 0 \tag{2.59}$$

Taking the second partial derivative of equation (2.44) with respect to time and substituting the equations (2.44), (2.45), (2.50), (2.51), (2.52) and (2.53) in equation (2.39), we have:

$$\overline{V}[-M\omega^2 + 2S(1-\cos(k_2L)) + s_2 + 2G(1-\cos(k_1L))] + \overline{v}[-s_2] = 0 \tag{2.60}$$

Taking the second partial derivative of equation (2.45) with respect to time and substituting the equations (2.44) and (2.45) into equation (2.40), we have:

$$\overline{v}[-m\omega^2 + s_2] + \overline{V}[-s_2] = 0 \tag{2.61}$$

Equations (2.60) and (2.61) can be collected in a 2x2 algebraic system:

$$\begin{bmatrix} -M\omega^2 + 2S(1-\cos(k_2L)) + s_2 + 2G(1-\cos(k_1L)) & -s_2 \\ -s_2 & -m\omega^2 + s_2 \end{bmatrix} \begin{bmatrix} \overline{V} \\ \overline{v} \end{bmatrix} = \begin{bmatrix} 0 \\ 0 \end{bmatrix} \tag{2.62}$$

Dispersion equation along the direction x_2 Computing the determinant of the coefficients' matrix in the algebraic system (2.62) and putting it equal to zero, it is possible to obtain the dispersion equation along the direction x_2 in the form:

$$Mm\omega^4 - s_2(M+m)\omega^2 + 2S[s_2 - m\omega^2](1-\cos(k_2L)) + 2G[s_2 - m\omega^2](1-\cos(k_1L)) = 0 \tag{2.63}$$

Equations (2.59) and (2.63) have to be solved in order to find the frequencies ω of propagating Bloch's waves as a function of the wavevector $\boldsymbol{k}$. Within the variation of the wavevector along the three sides of the IBZ, the frequencies ω can be obtained solving the biquadratic equations (2.59) and (2.63) with MATLAB. The obtained $\omega(\boldsymbol{k})$ are the so-called dispersion curves; in particular, for each direction, two dispersion curves will be achieved. When the internal stiffnesses s_1 and s_2 are equal, i.e., isotropic case, the dispersion diagram can be composed by pass and band gaps, while for different internal stiffnesses s_1 and s_2, i.e., anisotropic case, the dispersion diagram can be composed by pass and polarization band gaps along the direction x_1 and x_2.

Effective mass matrix Wave propagation in the "mass-in-mass"-spring lattice of figure 2.8 is thus governed by the two systems (2.58) and (2.62). Starting from this formulation, one can obtain an interesting interpretation in terms of effective masses.

In order to find the effective mass matrix, it is possible to solve the algebraic system (2.58) for $\overline{u}$ and the system (2.62) for $\overline{v}$:

$$\overline{u} = \frac{s_1}{s_1 - m\omega^2}\overline{U} \tag{2.64}$$

and

$$\overline{v} = \frac{s_2}{s_2 - m\omega^2}\overline{V} \tag{2.65}$$

Substituting (2.64) in the first row of the system (2.58) and (2.65) in the first row of the system (2.62), it is possible to derive these equations:

$$\omega^2[M + \frac{ms_1}{s_1 - m\omega^2}] = 2S(1 - \cos(k_1 L)) + 2G(1 - \cos(k_2 L)) \tag{2.66}$$

and

$$\omega^2[M + \frac{ms_2}{s_2 - m\omega^2}] = 2S(1 - \cos(k_2 L)) + 2G(1 - \cos(k_1 L)) \tag{2.67}$$

Equation (2.66) can be interpreted as the dynamic equilibrium equation in the direction x_1 of an equivalent resonator having an effective mass $m_{eff,11}$:

$$m_{eff,11} = M + \frac{ms_1}{s_1 - m\omega^2} \tag{2.68}$$

Analogously, equation (2.67) can be interpreted as the dynamic equilibrium equation in the direction x_2 of an equivalent resonator having an effective mass $m_{eff,22}$:

$$m_{eff,22} = M + \frac{ms_2}{s_2 - m\omega^2} \tag{2.69}$$

The effective mass matrix can be defined as:

$$M_{eff} = \begin{bmatrix} m_{eff,11} & 0 \\ 0 & m_{eff,22} \end{bmatrix} \tag{2.70}$$

The effective masses $m_{eff,11}$ and $m_{eff,22}$ are frequency-dependent and can be negative in some frequency intervals. These frequency ranges are coincident with the band gaps or polarization band gaps found in the dispersion diagrams.

Comparison between the dispersion curves and the effective mass The results obtained exploiting the dispersion analysis and those coming from the effective mass approach can be compared in order to identify the position and size of the band gaps for the isotropic case and of the polarization band gaps for the anisotropic case.

Dispersion curves versus effective mass: isotropic cases The input data for the example shown in figure 2.10 are: M=0.074 kg/m; m=0.0094 kg/m; s_1=s_2=630.22 N/m; S=10^8 N/m; G=$1.80 \cdot 10^6$ N/m; L=0.04 m. The resonance frequency is $\omega/2\pi$=41.21 Hz.

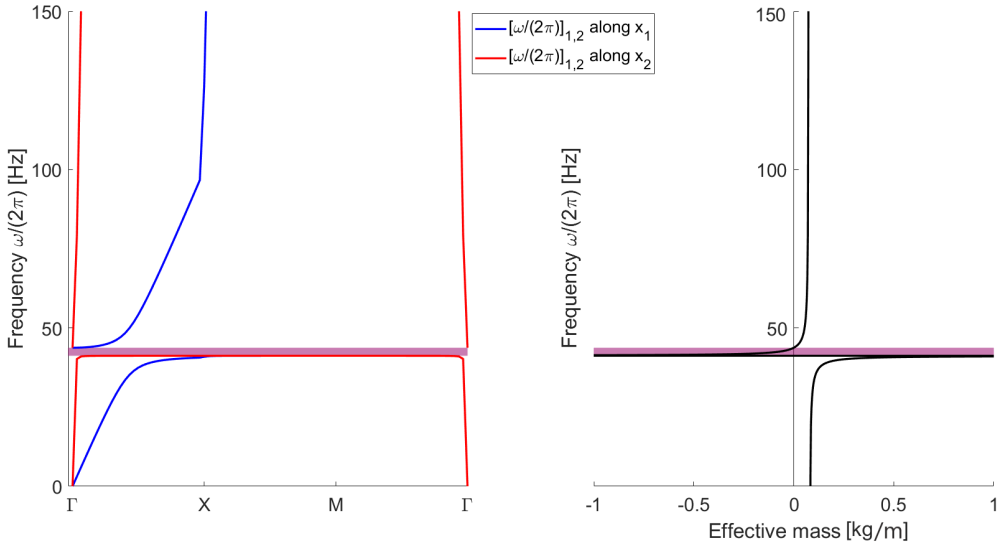

Figure 2.10. Dispersion curves versus effective mass: isotropic case with s_1=s_2=630.22 [N/m]

In this case, only one shaded region can be identified and this is a band gap, highlighted in purple. In this zone, waves cannot propagate without attenuation. The effective mass is equal in the two directions, as s_1=s_2 in equations (2.68), (2.69) and becomes negative in the same interval identifying the band gap.

Another example is shown in figure 2.11 corresponding to the following data: M=0.074 kg/m; m=0.0094 kg/m; s_2=s_1=1721.00 N/m; S=10^8 N/m; G=$1.80 \cdot 10^6$ N/m; L=0.04 m. The resonance frequency is $\omega/2\pi$=68.10 Hz.

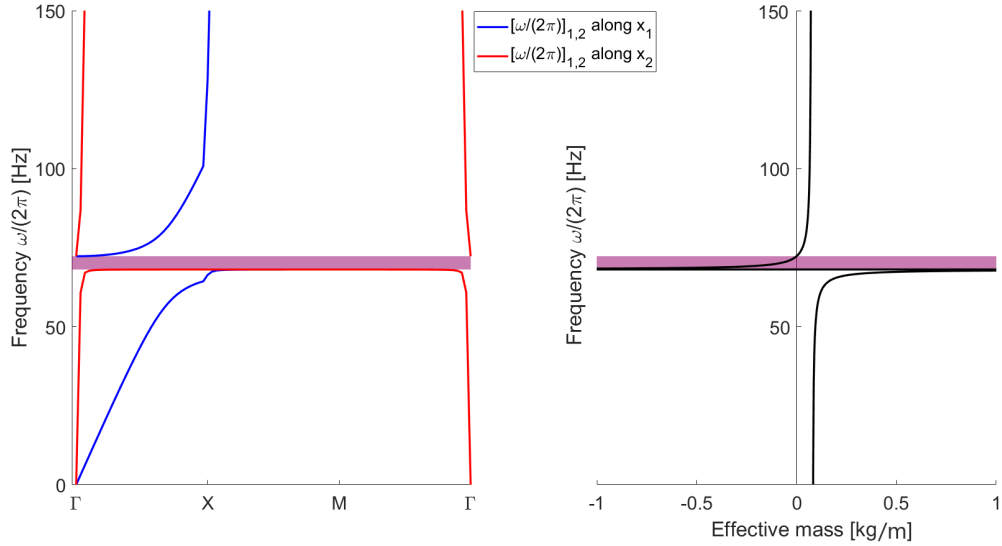

Figure 2.11. Dispersion curves versus effective mass: isotropic case with s_2=s_1=1721.00 [N/m]

Also in this case, only one shaded region can be identified and this is a band gap, highlighted in purple. In this zone, waves cannot propagate without attenuation and the effective mass is negative.

Dispersion curves versus effective masses: anisotropic case The input data for the example shown in figure 2.12 are: M=0.074 kg/m; m=0.0094 kg/m; s_1=630.22 N/m; s_2=1721.00 N/m; S=10^8 N/m; G=$1.80 \cdot 10^6$ N/m; L=0.04 m. The resonance frequencies are $\omega/2\pi$=41.21 Hz for the direction x_1 and $\omega/2\pi$=68.10 Hz for the direction x_2.

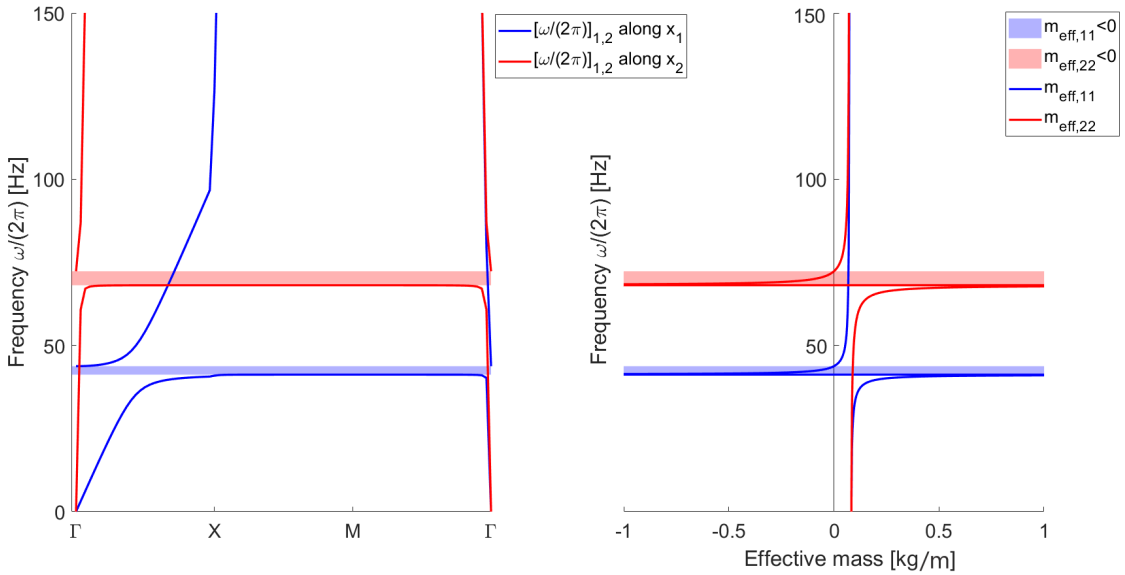

Figure 2.12. Dispersion curves versus effective masses: anisotropic case with s_1=630.22 [N/m] and s_2=1721.00 [N/m]

The effective mass is different in the two directions, as $s_1 \neq s_2$ in equations (2.68), (2.69) and becomes negative in different intervals identifying the polarization band gaps. Two different shaded regions can be distinguished:

- blue zone, in which the horizontal component of the effective mass ($m_{eff,11}$) is negative and this is a polarization band gap
- red zone, in which the vertical component of the effective mass ($m_{eff,22}$) is negative and also this is a polarization band gap.

Parametric discussion The influence of different parameters on the behaviour of the discrete model can be discussed by introducing two non-dimensional parameters:

$$\alpha = \frac{m}{M} \tag{2.71}$$

$$\beta = \frac{s_2}{s_1} \tag{2.72}$$

Dispersion equation along the direction x_1 The equation (2.59) can be rewritten in function of α and β in an implicit form:

$$\frac{\alpha M\omega^4}{\beta s_1}-\frac{(\alpha+1)\omega^2}{\beta}+[\frac{2S}{\beta M}-\frac{2S\alpha\omega^2}{\beta s_1}](1-\cos(k_1L))+[\frac{2G}{\beta M}-\frac{2G\alpha\omega^2}{\beta s_1}](1-\cos(k_2L))=0 \tag{2.73}$$

Dispersion equation along the direction x_2 Also the equation (2.63) can be rewritten in function of α and β in an implicit form:

$$\frac{\alpha M\omega^4}{\beta s_1}-(\alpha+1)\omega^2+[\frac{2S}{M}-\frac{2S\alpha\omega^2}{\beta s_1}](1-\cos(k_2L))+[\frac{2G}{M}-\frac{2G\alpha\omega^2}{\beta s_1}](1-\cos(k_1L))=0 \tag{2.74}$$

The goal is to obtain a relation in which the frequencies ω depend only on α and β. Since the frequencies ω depend also on the wavevector, it is useful to study a specific set of values for k_1L and k_2L. Moreover, some quantities are fixed for simplicity: M=0.074 kg/m; s_1=630.22 N/m.

Direction x_1 The first step is to find the 2 positive solutions $\omega_{1,2}$ of the biquadratic equation 2.73 with MATLAB. The 2 positive solutions depend on α, k_1L and k_2L but not on β. Since the dispersion curves are plotted only along the IBZ (figure 2.5), it is possible to restict the 2 positive solutions in this way:

$$\begin{cases} \Gamma X : \omega_{1,2}=\omega_{1,2}(k_1L=0,k_2L), & k_2L=\lambda\pi & \lambda\in[0,1] \\ XM : \omega_{1,2}=\omega_{1,2}(k_1L,k_2L=\pi), & k_1L=\lambda\pi & \lambda\in[0,1] \\ M\Gamma : \omega_{1,2}=\omega_{1,2}(k_1L,k_2L=k_1L), & k_1L=\lambda\pi & \lambda\in[0,1] \end{cases} \tag{2.75}$$

Along Γ X, the stationary points are obtained from:

$$\frac{d\omega_1}{d(k_2L)}=0 \qquad \text{and} \qquad \frac{d\omega_2}{d(k_2L)}=0 \tag{2.76}$$

After finding the values k_1L and k_2L, it is possible to put these results in the 2 positive solutions $\omega_{1,2}$ for all the 3 sides of the Irreducible Brilluoin Zone. Fixing for example α=0.1 [-] and this can be done for all the values, the next tables 2.1, 2.2 and 2.3 resume the results.

Table 2.1. Maximization and minimization discussion for k_2L along Γ X for α=0.1

	k_2L=0	$k_2L=\pi$
$\omega_1/2\pi$[Hz]	0	46.444
$\omega_2/2\pi$[Hz]	48.713	1569.963

Table 2.2. Maximization and minimization discussion for k_1L along XM for α=0.1

	k_1L=0	$k_1L = \pi$
$\omega_1/2\pi$[Hz]	46.444	46.446
$\omega_2/2\pi$[Hz]	1569.963	37036.063

Table 2.3. Maximization and minimization discussion for k_1L=k_2L along MΓ for α=0.1

	k_1L=k_2L=0	k_1L=k_2L=π
$\omega_1/2\pi$[Hz]	0	46.446
$\omega_2/2\pi$[Hz]	48.713	37036.063

From these results, it can be noticed that when the wavevector components are approaching 0, the frequencies $\omega_{1,2}$ are minimized; whereas, when they are approaching to π, the frequencies $\omega_{1,2}$ are maximized. In order to take the absolute maxima for the opening frequency ω_1, the values of the wave vector's components are:

$$k_1L = k_2L = \pi \tag{2.77}$$

In order to take the absolute minima for the closure frequency ω_2, the values of the wave vector's components are:

$$k_1L = k_2L = 0 \tag{2.78}$$

The solutions $\omega_{1,2}$ along the direction x_1 can be plotted in function of α.

Direction x_2 The same procedure can be applied to the the direction x_2, starting from the biquadratic equation 2.74. The results of of the wavevector components are the same expressed in the previous paragraph. In this case, the solutions $\omega_{1,2}$ along the direction x_2 can be plotted in function of α and β.

The solutions $\omega_{1,2}$ along the direction x_1 and along the direction x_2 are plotted in the next figures (2.13 and 2.14), fixing 4 cases of α=[0.1, 1, 3, 10]. The blue lines represent the opening and closure frequencies along direction x_1 independent from β, the red ones represent the opening and closure frequencies along direction x_2 dependent from β and the shaded area in purple represent the band gap zone. Moreover, the area between the blue and red lines, respectively, represent the polarization band gap zone.

With reference to figures 2.13 and 2.14, the band gap zone tend to expand with the increment of α and hence with the increment of the internal mass m, for fixed mass M. Since s_1 is fixed, the influence of β is relevant only for the opening and closure frequencies along direction x_2 that vary within s_2.

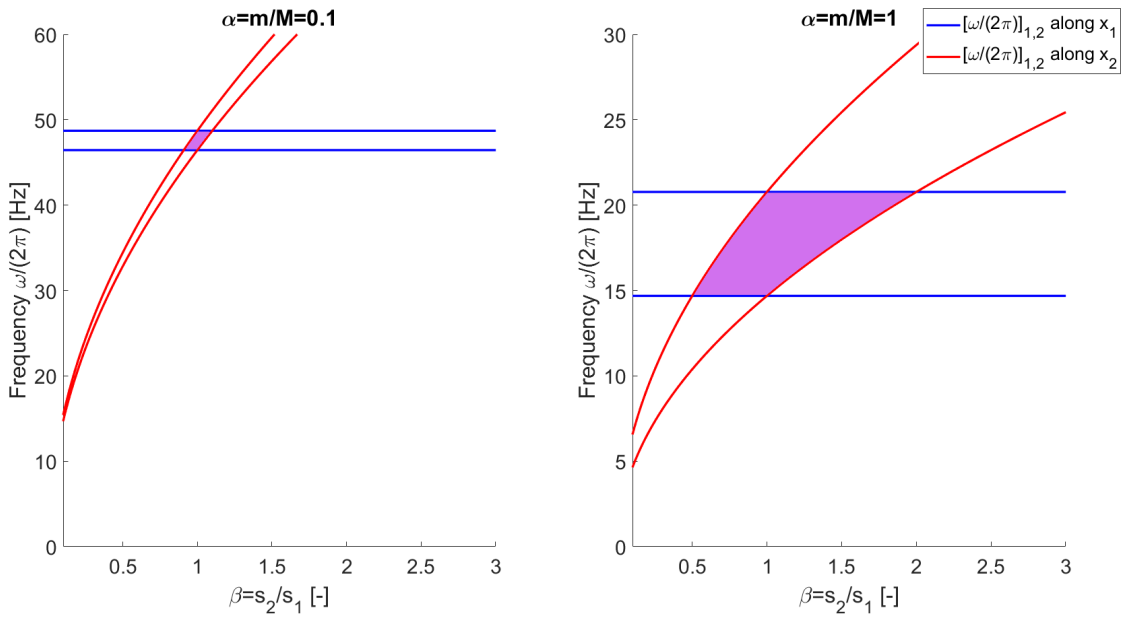

Figure 2.13. Opening and closure frequencies along x_1 and x_2 in function of β: cases with α=0.1, 1

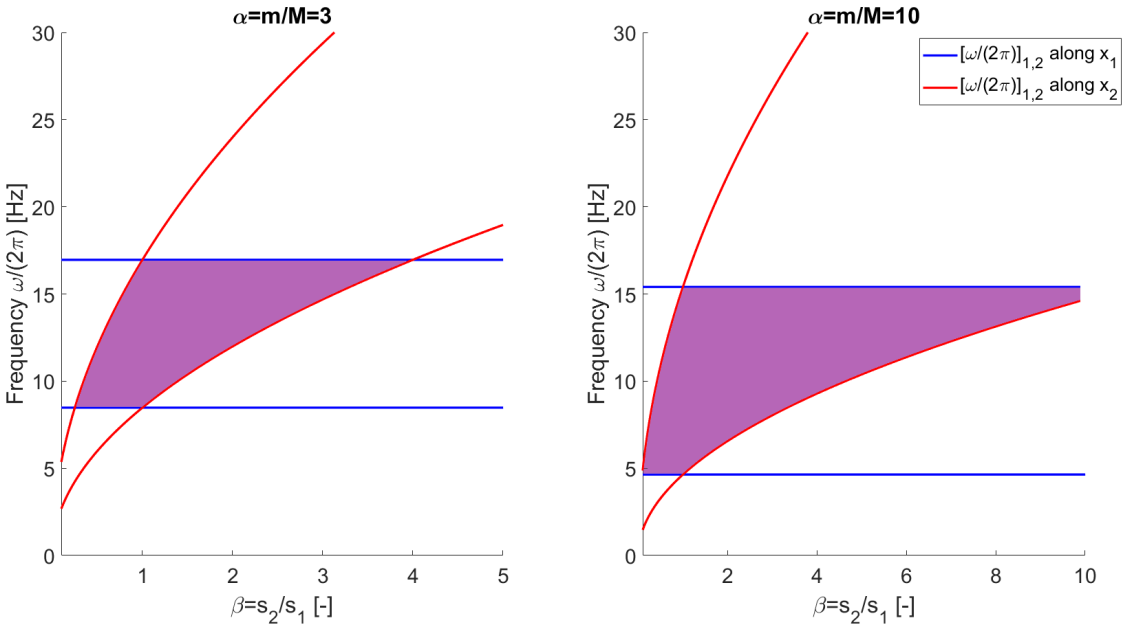

Figure 2.14. Opening and closure frequencies along x_1 and x_2 in function of β: cases with α=3, 10

Chapter 3

Dynamic homogenization of locally-resonant metamaterials

In this chapter, the asymptotic dynamic homogenization technique will be discussed for locally-resonant metamaterials. The formulation, for the in-plane wave propagation, is given in [7].

3.1 Problem formulation

A ternary locally resonant metamaterial is considered in which the unit cell is composed by a stiff matrix (m) containing a compliant coating (c) and an eccentric rigid cylindrical fiber (f), as shown in the figure 3.1. The material is endowed with a two-dimensional periodicity.

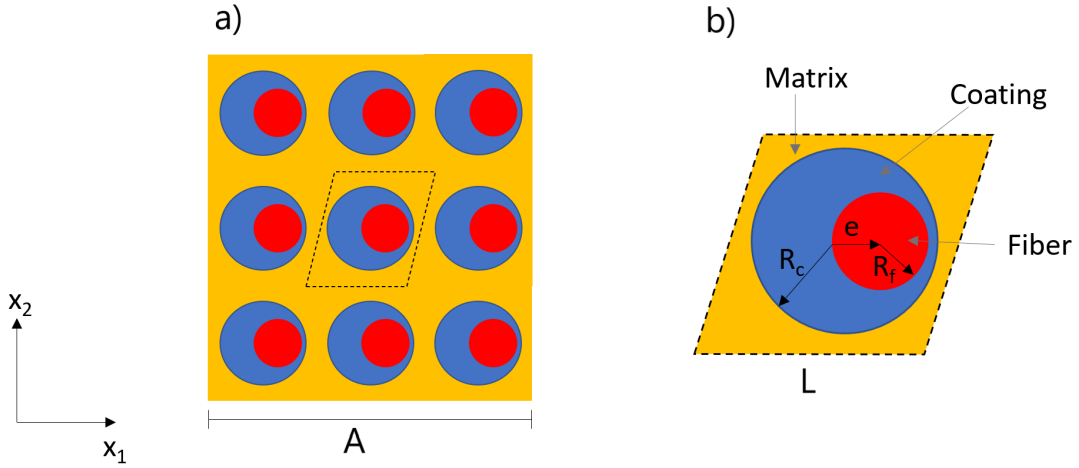

Figure 3.1. a) Geometry of locally resonant metamaterial b) Unit cell with eccentric fiber

The matrix and the coating are considered with a linear elastic isotropic behaviour, while the fiber is considered as rigid. The in-plane periodicity of the cylindrical body allows us to study the propagation of an in-plane wave in plane strain conditions. We call Ω^ϵ the section that can be obtained by the periodic repetition of the unit

cell Y^ϵ (figure 3.1). Then, $\boldsymbol{x} = x_1\boldsymbol{e}_1 + x_2\boldsymbol{e}_2$ is the macroscopic position vector with $\boldsymbol{e}_1$ the unit vector along axis x_1 and $\boldsymbol{e}_2$ the unit vector along axis x_2. Moreover, we assume the scale separation hypothesis for which the ratio $\epsilon = L/A \ll 1$, where A and L are the characteristic sizes of Ω^ϵ and Y^ϵ, respectively.

With reference to small strains and displacements hypothesis, the in-plane wave propagation in Ω^ϵ is governed by the Helmholtz equation:

$$\nabla \cdot [\mathbb{D}^\epsilon : \boldsymbol{\varepsilon}(\boldsymbol{u}^\epsilon)] + \rho^\epsilon \omega^2 \boldsymbol{u}^\epsilon = \boldsymbol{0} \tag{3.1}$$

where ω is the angular frequency, $\boldsymbol{u}(\boldsymbol{x}) = u_1(\boldsymbol{x})\boldsymbol{e}_1 + u_2(\boldsymbol{x})\boldsymbol{e}_2$ is the displacement field, $\boldsymbol{\varepsilon}(\boldsymbol{u}^\epsilon)$ is the small strain tensor, i.e., the symmetric part of the displacement gradient, whereas $\mathbb{D}^\epsilon(\boldsymbol{x})$ and $\rho^\epsilon(\boldsymbol{x})$ are the fourth order elastic stiffness tensor and mass density of the involved materials. For isotropic materials, the elastic stiffness tensor can be defined as:

$$\mathbb{D}^\epsilon = 2\mu^\epsilon \mathbb{I} + \lambda^\epsilon \boldsymbol{I} \otimes \boldsymbol{I} \tag{3.2}$$

where $\lambda^\epsilon(\boldsymbol{x})$ and $\mu^\epsilon(\boldsymbol{x})$ are the Lame's constants.

We define the stress field $\boldsymbol{\sigma}^\epsilon$ in Ω^ϵ as:

$$\boldsymbol{\sigma}^\epsilon = \mathbb{D}^\epsilon : \boldsymbol{\varepsilon}^\epsilon \tag{3.3}$$

with

$$\boldsymbol{\varepsilon}^\epsilon = \frac{1}{2}(\nabla \boldsymbol{u}^\epsilon + \nabla^T \boldsymbol{u}^\epsilon) \tag{3.4}$$

We further assume that there is high contrast between the stiffness of the matrix and that of the coating, while we consider the simplifying assumption of rigid fiber. The mass densities of the three materials are supposed to be of the same order of magnitude. These hypothesis are introduced as follow:

$$\lambda^\epsilon = \begin{cases} \lambda_m & \text{in } Y_m^\epsilon \\ \epsilon^2 \lambda_c & \text{in } Y_c^\epsilon, \end{cases} \quad \mu^\epsilon = \begin{cases} \mu_m & \text{in } Y_m^\epsilon \\ \epsilon^2 \mu_c & \text{in } Y_c^\epsilon \end{cases} \quad \text{and } \rho^\epsilon = \begin{cases} \rho_m & \text{in } Y_m^\epsilon \\ \rho_c & \text{in } Y_c^\epsilon \\ \rho_f & \text{in } Y_f^\epsilon \end{cases} \tag{3.5}$$

3.2 Asymptotic homogenization

With reference to the two-scale asymptotic homogenization technique, it is possible to define the homogenized domain Ω and the fast variable $\boldsymbol{y} = \boldsymbol{x}/\epsilon = y_1\boldsymbol{e}_1 + y_2\boldsymbol{e}_2$. The latter is defined in the re-scaled unit cell $Y = Y^\epsilon/\epsilon$ of the periodic media. The classical two-scale asymptotic method consists on expanding the field $\boldsymbol{u}^\epsilon$ in Ω^ϵ as:

$$\boldsymbol{u}^\epsilon(\boldsymbol{x}) = \boldsymbol{u}^0\left(\boldsymbol{x}, \frac{\boldsymbol{x}}{\epsilon}\right) + \epsilon \boldsymbol{u}^1\left(\boldsymbol{x}, \frac{\boldsymbol{x}}{\epsilon}\right) + \epsilon^2 \boldsymbol{u}^2\left(\boldsymbol{x}, \frac{\boldsymbol{x}}{\epsilon}\right) + o(\epsilon^2) \tag{3.6}$$

where the vector fields $\boldsymbol{u}^i(\boldsymbol{x}, \boldsymbol{y})$ are defined on $\Omega \times Y$ and are Y-periodic with respect to $\boldsymbol{y}$.

In the same manner, the stress field $\boldsymbol{\sigma}^\epsilon$ is expanded in Ω^ϵ as:

$$\boldsymbol{\sigma}^\epsilon(\boldsymbol{x}) = \epsilon^{-1}\boldsymbol{\sigma}^{-1}\left(\boldsymbol{x}, \frac{\boldsymbol{x}}{\epsilon}\right) + \boldsymbol{\sigma}^0\left(\boldsymbol{x}, \frac{\boldsymbol{x}}{\epsilon}\right) + \epsilon\boldsymbol{\sigma}^1\left(\boldsymbol{x}, \frac{\boldsymbol{x}}{\epsilon}\right) + \epsilon^2\boldsymbol{\sigma}^2\left(\boldsymbol{x}, \frac{\boldsymbol{x}}{\epsilon}\right) + o(\epsilon^2) \tag{3.7}$$

where the vector fields $\boldsymbol{\sigma}^i(\boldsymbol{x}, \boldsymbol{y})$ are defined on $\Omega \times Y$ and are Y-periodic with respect to $\boldsymbol{y}$.

For a vector $\boldsymbol{u}(\boldsymbol{x}, \boldsymbol{y})$, one denotes by $\boldsymbol{\varepsilon}_{\boldsymbol{x}}(\boldsymbol{u})$ the symmetric part of the gradient of $\boldsymbol{u}$ with respect to $\boldsymbol{x}$ and by $\boldsymbol{\varepsilon}_{\boldsymbol{y}}(\boldsymbol{u})$ the symmetric part of the gradient of $\boldsymbol{u}$ with respect to $\boldsymbol{y}$. In the same manner, for a tensor $\boldsymbol{\sigma}(\boldsymbol{x}, \boldsymbol{y})$, one denotes by $\nabla_{\boldsymbol{x}} \cdot \boldsymbol{\sigma}$ and $\nabla_{\boldsymbol{y}} \cdot \boldsymbol{\sigma}$ the divergence of $\boldsymbol{\sigma}$ with respect to $\boldsymbol{x}$ and $\boldsymbol{y}$, respectively. Moreover, the gradients and the divergences are computed with the chain rule. For the gradients, $\boldsymbol{\varepsilon}(\boldsymbol{u}) = \boldsymbol{\varepsilon}_{\boldsymbol{x}}(\boldsymbol{u}) + \epsilon^{-1}\boldsymbol{\varepsilon}_{\boldsymbol{y}}(\boldsymbol{u})$, whereas for the divergences, $\nabla \cdot \boldsymbol{\sigma} = \nabla_{\boldsymbol{x}} \cdot \boldsymbol{\sigma} + \epsilon^{-1}\nabla_{\boldsymbol{y}} \cdot \boldsymbol{\sigma}$.

From the expansion (3.6), one gets:

$$\boldsymbol{\varepsilon}(\boldsymbol{u}^\epsilon) = \epsilon^{-1}\boldsymbol{\varepsilon}_{\boldsymbol{y}}(\boldsymbol{u}^0) + [\boldsymbol{\varepsilon}_{\boldsymbol{y}}(\boldsymbol{u}^1) + \boldsymbol{\varepsilon}_{\boldsymbol{x}}(\boldsymbol{u}^0)] + \epsilon[\boldsymbol{\varepsilon}_{\boldsymbol{y}}(\boldsymbol{u}^2) + \boldsymbol{\varepsilon}_{\boldsymbol{x}}(\boldsymbol{u}^1)] + o(\epsilon) \tag{3.8}$$

and from the expansion (3.7), one gets:

$$\nabla \cdot \boldsymbol{\sigma}^\epsilon = \epsilon^{-2}\nabla_{\boldsymbol{y}} \cdot \boldsymbol{\sigma}^{-1} + \epsilon^{-1}\nabla_{\boldsymbol{y}} \cdot \boldsymbol{\sigma}^0 + (\nabla_{\boldsymbol{y}} \cdot \boldsymbol{\sigma}^1 + \nabla_{\boldsymbol{x}} \cdot \boldsymbol{\sigma}^0) + \epsilon(\nabla_{\boldsymbol{y}} \cdot \boldsymbol{\sigma}^2 + \nabla_{\boldsymbol{x}} \cdot \boldsymbol{\sigma}^1) + o(\epsilon) \tag{3.9}$$

The above expansions (3.6)-(3.9) are substituted into the governing equation (3.1). The terms of the same order in ϵ will be considered separately. At order -1, in $\Omega \times Y$, we have:

$$\nabla_{\boldsymbol{y}} \cdot \boldsymbol{\sigma}^0 = \mathbf{0} \tag{3.10}$$

while at order 0, in $\Omega \times Y$, we have:

$$\nabla_{\boldsymbol{y}} \cdot \boldsymbol{\sigma}^1 + \nabla_{\boldsymbol{x}} \cdot \boldsymbol{\sigma}^0 + \rho\omega^2\boldsymbol{u}^0 = \mathbf{0} \tag{3.11}$$

and at order 1, in $\Omega \times Y$, we have:

$$\nabla_{\boldsymbol{y}} \cdot \boldsymbol{\sigma}^2 + \nabla_{\boldsymbol{x}} \cdot \boldsymbol{\sigma}^1 + \rho\omega^2\boldsymbol{u}^1 = \mathbf{0} \tag{3.12}$$

Inserting (3.7) and (3.8) into (3.3)-(3.4) gives at order -1 in Y_m:

$$\boldsymbol{\varepsilon}_{\boldsymbol{y}}(\boldsymbol{u}^0) = \mathbf{0} \tag{3.13}$$

which implies that $\boldsymbol{u}^0$ depends only on $\boldsymbol{x}$ in $\Omega \times Y_m$:

$$\boldsymbol{u}^0(\boldsymbol{x}, \boldsymbol{y}) = \boldsymbol{U}^0(\boldsymbol{x}) \tag{3.14}$$

3.3 Motion in the matrix

Restricting the focus on the matrix only and with reference to (3.14), it is possible to derive the effective stiffness tensor through the homogenization procedure.

Firstly, the expansion of (3.3)-(3.4) gives, in $\Omega \times Y_m$, at order 0:

$$\boldsymbol{\sigma}^0 = \mathbb{D}_m : [\boldsymbol{\varepsilon}_{\boldsymbol{x}}(\boldsymbol{U}^0) + \boldsymbol{\varepsilon}_{\boldsymbol{y}}(\boldsymbol{u}^1)] \tag{3.15}$$

By considering (3.14) and using the periodic conditions that $\boldsymbol{u}^1$ and $\boldsymbol{\sigma}^0 \cdot \boldsymbol{N}$ must satisfy on the boundary of Y ($\boldsymbol{N}$ denotes the unit outer normal), by linearity, one derives that $\boldsymbol{u}^1$ can be expressed in $\Omega \times Y_m$ as:

$$\boldsymbol{u}^1(\boldsymbol{x}, \boldsymbol{y}) = \sum_{i,j=1}^{2} \varepsilon_{\boldsymbol{x},ij}(\boldsymbol{U}^0)\boldsymbol{\chi}^{ij}(\boldsymbol{y}) + \boldsymbol{U}^1(\boldsymbol{x}) \tag{3.16}$$

where $\varepsilon_{\boldsymbol{x},ij}$ is the component ij-th of $\boldsymbol{\varepsilon}_{\boldsymbol{x}}(\boldsymbol{U}^0)$ which can be interpreted as a constant eigenstrain within the cell and $\boldsymbol{\chi}^{ij}$, for $i, j = 1, 2$, are the displacement fields solutions of the so-called matrix cell problems. These linear elastic problems, that have to be solved only in the matrix, are written as:

$$\begin{cases} \nabla_{\boldsymbol{y}} \cdot [\mathbb{D}_m : (\boldsymbol{\varepsilon}_{\boldsymbol{y}}(\boldsymbol{\chi}^{ij}) + \boldsymbol{e}_i \odot \boldsymbol{e}_j)] = \boldsymbol{0} & \text{in } Y_m \\ [\mathbb{D}_m : (\boldsymbol{\varepsilon}_{\boldsymbol{y}}(\boldsymbol{\chi}^{ij}) + \boldsymbol{e}_i \odot \boldsymbol{e}_j)] \cdot \boldsymbol{N} = \boldsymbol{0} & \text{on } \partial Y_m \setminus \partial Y \\ \boldsymbol{\chi}^{ij} \text{ periodic} & \text{on } \partial Y \\ [\mathbb{D}_m : (\boldsymbol{\varepsilon}_{\boldsymbol{y}}(\boldsymbol{\chi}^{ij}) + \boldsymbol{e}_i \odot \boldsymbol{e}_j)] \cdot \boldsymbol{N} \text{ anti-periodic} & \text{on } \partial Y \end{cases} \tag{3.17}$$

where $\boldsymbol{\varepsilon}_{\boldsymbol{y}}(\boldsymbol{\chi}^{ij})$ is the small strain tensor, i.e., the symmetric part of the displacement gradient, $\boldsymbol{e}_i \odot \boldsymbol{e}_j = 1/2(\boldsymbol{e}_i \otimes \boldsymbol{e}_j + \boldsymbol{e}_j \otimes \boldsymbol{e}_i)$ is the symmetric part of the tensorial product between $\boldsymbol{e}_i$ and $\boldsymbol{e}_j$, which represents a uniform imposed eigenstrain and $\mathbb{D}_m$ is the elastic stiffness tensor of the matrix. Moreover, on $\partial Y_m \setminus \partial Y$, it is imposed the null traction condition and on ∂Y, periodicity conditions are defined for the traction and for the displacement fields $\boldsymbol{\chi}^{ij}$. Each matrix cell problem is defined up to a constant that can be fixed as:

$$\int_{Y_m} \boldsymbol{\chi}^{ij}(\boldsymbol{y}) d\boldsymbol{y} = \boldsymbol{0} \tag{3.18}$$

With reference to (3.14) and (3.15), the stress field $\boldsymbol{\sigma}^0$ can be defined, in $\Omega \times Y_m$, as:

$$\boldsymbol{\sigma}^0(\boldsymbol{x}, \boldsymbol{y}) = \sum_{i,j=1}^{2} \mathbb{D}_m : [\boldsymbol{\varepsilon}_{\boldsymbol{y}}(\boldsymbol{\chi}^{ij}(\boldsymbol{y})) + \boldsymbol{e}_i \odot \boldsymbol{e}_j)]\varepsilon_{\boldsymbol{x},ij}(\boldsymbol{U}^0) \tag{3.19}$$

Considering the average value of $\boldsymbol{\sigma}^0$ on Y and using (3.17), one obtains:

$$\langle \boldsymbol{\sigma}^0 \rangle(\boldsymbol{x}) := \frac{1}{|Y|} \int_Y \boldsymbol{\sigma}^0(\boldsymbol{x}, \boldsymbol{y}) d\boldsymbol{y} = \mathbb{D}^0 : \boldsymbol{\varepsilon}^0(\boldsymbol{U}^0) \tag{3.20}$$

where $\mathbb{D}^0$ is the fourth order homogenized stiffness tensor whose components are given by:

$$D^0_{ijhk} = \frac{1}{|Y|}\int_{Y_m} [\boldsymbol{\varepsilon}_{\boldsymbol{y}}(\boldsymbol{\chi}^{ij}) + \boldsymbol{e}_i \odot \boldsymbol{e}_j] : \mathbb{D}_m : [\boldsymbol{\varepsilon}_{\boldsymbol{y}}(\boldsymbol{\chi}^{hk}) + \boldsymbol{e}_h \odot \boldsymbol{e}_k] d\boldsymbol{y} \tag{3.21}$$

for $i, j, h, k \in \{1, 2\}$. In equation (3.21), the functions $\boldsymbol{\chi}^{ij}(\boldsymbol{y})$ represent the periodic displacement field of the re-scaled unit cell Y when it is subjected to a uniform eigenstrain $\boldsymbol{e}_i \odot \boldsymbol{e}_j$. The equation (3.21) can be interpreted as the homogenized stiffness of the holed periodic media.

3.4 Motion in the inclusions

With reference to the coating and the fiber only, we assume that the reference system $y_1 - y_2$ is centroidal for the fiber, so that:

$$\int_{Y_c \cup Y_f} \boldsymbol{y} d\boldsymbol{y} = \boldsymbol{0} \tag{3.22}$$

The fiber undergoes an in-plane rigid body motion within Y and one has that in $\Omega \times Y_f$:

$$\boldsymbol{u}^0(\boldsymbol{x}, \boldsymbol{y}) = \sum_{i=1}^{2} U^0_i(\boldsymbol{x})(\boldsymbol{\tau}^i + \psi^i \boldsymbol{y} \wedge \boldsymbol{e}_3) \tag{3.23}$$

where $\boldsymbol{\tau}^i$ and ψ^i for $i \in \{1, 2\}$ describe, respectively, the displacement of the centroid and the in-plane rotation of the fiber.

For exploiting the problem related to the coating, first of all, the expansion of (3.3)-(3.4) gives, in $\Omega \times Y_c$, at order 0:

$$\boldsymbol{\sigma}^0 = \boldsymbol{0} \tag{3.24}$$

Substituting equation (3.24) into (3.11), we obtain in $\Omega \times Y_c$:

$$\nabla_{\boldsymbol{y}} \cdot \boldsymbol{\sigma}^1 + \rho_c \omega^2 \boldsymbol{u}^0 = \boldsymbol{0} \tag{3.25}$$

where

$$\boldsymbol{\sigma}^1 = \mathbb{D}_c : \boldsymbol{\varepsilon}_{\boldsymbol{y}}(\boldsymbol{u}^0) \tag{3.26}$$

due to the expansion of the constitutive relation (3.3) at order 1. Substituting equation (3.26) into (3.25), we obtain the problem governing the motion of the coating:

$$\begin{cases} \nabla_{\boldsymbol{y}} \cdot [\mathbb{D}_c : \boldsymbol{\varepsilon}_{\boldsymbol{y}}(\boldsymbol{u}^0)] + \rho_c \omega^2 \boldsymbol{u}^0 = \boldsymbol{0} & \text{in } Y_c \\ \boldsymbol{u}^0 = \boldsymbol{U}^0 & \text{on } \partial Y_c \\ \boldsymbol{u}^0 = \sum_{i=1}^{2} U^0_i(\boldsymbol{x})(\boldsymbol{\tau}^i + \psi^i \boldsymbol{y} \wedge \boldsymbol{e}_3) & \text{on } \partial Y_f \end{cases} \tag{3.27}$$

The linearity of the problem (3.27) allows to search a displacement field defined in $\Omega \times Y_c$ as:

$$\boldsymbol{u}^0(\boldsymbol{x}, \boldsymbol{y}) = \sum_{i=1}^{2} U_i^0(\boldsymbol{x}) \boldsymbol{\eta}^i(\boldsymbol{y}) \tag{3.28}$$

where the displacement functions $\boldsymbol{\eta}^i$, for $i \in \{1, 2\}$, solve the differential problems:

$$\begin{cases} \nabla_{\boldsymbol{y}} \cdot [\mathbb{D}_c : \boldsymbol{\varepsilon}_{\boldsymbol{y}}(\boldsymbol{\eta}^i)] + \rho_c \omega^2 \boldsymbol{\eta}^i = \boldsymbol{0} & \text{in } Y_c \\ \boldsymbol{\eta}^i = \boldsymbol{e}_i & \text{on } \partial Y_c \setminus \partial Y_f \\ \boldsymbol{\eta}^i = \boldsymbol{\tau}^i + \psi^i \boldsymbol{y} \wedge \boldsymbol{e}_3 & \text{on } \partial Y_f \end{cases} \tag{3.29}$$

The displacements $\boldsymbol{\eta}^i$ depend on the frequency. It is important to take into account that on $\partial Y_c \setminus \partial Y_f$, it is applied a unitary displacement along directions $i \in \{1, 2\}$. $\boldsymbol{\tau}^i$ and ψ^i can be determined by enforcing the balance of linear and angular momentum of the fiber. The boundary ∂Y_f of the fiber is subjected to the stress $\boldsymbol{\sigma}^1$ developed by the coating, as shown in figure 3.2.

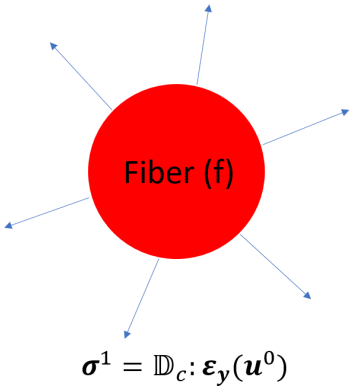

Figure 3.2. State of stress on ∂Y_f of the fiber

The equilibrium in weak form is defined by:

$$\begin{cases} \int_{\partial Y_f} \boldsymbol{\sigma}^1 \cdot \boldsymbol{N} d\boldsymbol{y} + \int_{Y_f} \rho_f \boldsymbol{u}^0 \omega^2 d\boldsymbol{y} = \boldsymbol{0} \\ \boldsymbol{e}_3 \cdot \int_{\partial Y_f} \boldsymbol{y} \wedge (\boldsymbol{\sigma}^1 \cdot \boldsymbol{N}) d\boldsymbol{y} + \int_{Y_f} \rho_f \boldsymbol{y} \wedge \boldsymbol{u}^0 \omega^2 d\boldsymbol{y} = 0 \end{cases} \tag{3.30}$$

Substituting (3.26) and (3.28) into (3.30), one obtains:

$$\begin{cases} \int_{\partial Y_f} [\mathbb{D}_c : \boldsymbol{\varepsilon}_{\boldsymbol{y}}(\boldsymbol{\eta}^i)] \cdot \boldsymbol{N} d\boldsymbol{y} + \rho_f |Y_f| \omega^2 \boldsymbol{\tau}^i = \boldsymbol{0} \\ \boldsymbol{e}_3 \cdot \int_{\partial Y_f} \boldsymbol{y} \wedge [\mathbb{D}_c : \boldsymbol{\varepsilon}_{\boldsymbol{y}}(\boldsymbol{\eta}^i)] \cdot \boldsymbol{N} d\boldsymbol{y} + \rho_f I_f \omega^2 \psi^i = 0 \end{cases} \tag{3.31}$$

for $i, j \in \{1, 2\}$ and with I_f the second polar moment of the fiber, defined as:

$$I_f = \int_{Y_f} ||\boldsymbol{y}||^2 d\boldsymbol{y} \tag{3.32}$$

Equations (3.29) and (3.31) define the inclusion cell problem. The solution of this problem is given by the fields $\boldsymbol{\eta}^i(\boldsymbol{y}, \omega)$, $\boldsymbol{\tau}^i(\omega)$ and $\psi^i(\omega)$.

3.5 Homogenized equation of motion

Integrating the equation (3.11), defined at order 0, over Y, leads to the following expressions for the different terms:

$$\int_Y \nabla_{\boldsymbol{y}} \cdot \boldsymbol{\sigma}^1 d\boldsymbol{y} = \int_{\partial Y} \boldsymbol{\sigma}^1 \boldsymbol{N} ds = \boldsymbol{0} \text{ by virtue of the periodic conditions (divergence theorem),} \tag{3.33}$$

$$\langle \nabla_{\boldsymbol{x}} \cdot \boldsymbol{\sigma}^0 \rangle = \nabla_{\boldsymbol{x}} \cdot [\mathbb{D}^0 : \boldsymbol{\varepsilon}_{\boldsymbol{x}}(\boldsymbol{U}^0)] \text{ by virtue of (3.20) and} \tag{3.34}$$

$$\langle \rho \boldsymbol{u}^0 \rangle = \boldsymbol{\rho}^0(\omega) \boldsymbol{U}^0 \text{ by virtue of (3.14) and (3.28).} \tag{3.35}$$

With (3.33), (3.34) and (3.35), the homogenized Helmholtz equation of the periodic media in Ω is:

$$\nabla_{\boldsymbol{x}} \cdot [\mathbb{D}^0 : \boldsymbol{\varepsilon}_{\boldsymbol{x}}(\boldsymbol{U}^0)] + \omega^2 \boldsymbol{\rho}^0(\omega) \cdot \boldsymbol{U}^0 = \boldsymbol{0} \tag{3.36}$$

where $\boldsymbol{\rho}^0(\omega)$ is the effective mass density tensor, which is symmetric. The components of $\boldsymbol{\rho}^0(\omega)$ are given by:

$$\rho^0_{ij}(\omega) = \rho_{st}\delta_{ij} + \rho_c \frac{|Y_c|}{|Y|}\left(\frac{1}{|Y_c|}\int_{Y_c} \eta^i_j(\boldsymbol{y}, \omega) d\boldsymbol{y} - 1\right) + \rho_f \frac{|Y_f|}{|Y|}(\tau^i_j(\omega) - 1) \tag{3.37}$$

where δ_{ij} is the Kronecker's delta and ρ_{st} the static mass density, which is defined as:

$$\rho_{st} = \rho_m \frac{|Y_m|}{|Y|} + \rho_c \frac{|Y_c|}{|Y|} + \rho_f \frac{|Y_f|}{|Y|} \tag{3.38}$$

3.6 Effective dispersion properties

In order to obtain the disperion relation of the homogenized media, one can consider the propagation of the wave:

$$\boldsymbol{U}^0(\boldsymbol{x}) = \boldsymbol{p} \exp(\mathrm{i}\boldsymbol{k} \cdot \boldsymbol{x}) \tag{3.39}$$

where $\boldsymbol{p}$ is the polarization vector, $\boldsymbol{k} = k\boldsymbol{n}$ is the wavevector, k the wavenumber and $\boldsymbol{n}$ the propagation direction. In particular, $\boldsymbol{n}$ is:

$$\boldsymbol{n} = n_1 \boldsymbol{e}_1 + n_2 \boldsymbol{e}_2 = \cos\theta \boldsymbol{e}_1 + \sin\theta \boldsymbol{e}_2 \tag{3.40}$$

where $\theta \in [0, 2\pi]$ is the angle of propagation of the elastic wave, with respect to $\boldsymbol{e}_1$.

Substituting (3.39) into the effective Helmholtz equation (3.36), it is possible to obtain the effective dispersion relation:

$$[\boldsymbol{Q}^0(\boldsymbol{n}) - c^2 \boldsymbol{\rho}^0(\omega)] \cdot \boldsymbol{p} = \boldsymbol{0} \tag{3.41}$$

where $c = \omega/k$ is the phase velocity and $\boldsymbol{Q}^0(\boldsymbol{n})$ is the second order effective acoustic tensor:

$$\boldsymbol{Q}^0(\boldsymbol{n}) = \boldsymbol{n} \cdot \mathbb{D}^0 \cdot \boldsymbol{n} \tag{3.42}$$

$\boldsymbol{Q}^0(\boldsymbol{n})$ is a second order symmetric tensor due to the minor and major simmetries of $\mathbb{D}^0$ that can be noted in equation (3.21).

The eigenvalues of problem 3.41 are phase velocities and the associated eigenvectors are polarization directions. In our two-dimensional problem, three different kind of frequency intervals can be defined:

- Case 1: pass bands, in which both the principal mass components of the effective mass density tensor, i.e., ρ_I^0 and ρ_{II}^0, are positive. This implies that c_1^2 and c_2^2 are positive and, thus, equation (3.41) admits two real postive wave velocities c_1, c_2. In these frequency intervals, elastic waves can propagate.

- Case 2: band-gaps, when ρ_I^0 and ρ_{II}^0 are negative. This implies that c_1^2 and c_2^2 are negative and, therefore, equation (3.41) has no real solution. In these frequency intervals, elastic waves cannot propagate without attenuation.

- Case 3: polarization bands, when ρ_I^0 and ρ_{II}^0 have different sign. This implies that c_1^2 and c_2^2 have opposite sign and, thus, equation (3.41) admits a unique real positive solution. In these frequency intervals, elastic waves can propagate with a unique polarization vector which is mainly aligned with the principal direction of the positive mass.

Chapter 4

Evaluation of the homogenized properties

In this chapter, it is defined the evaluation of the homogenized properties for a ternary locally resonant metamaterial. In particular, we consider a circular fiber that can be eccentric or perfectly centered with respect to the coating. These two inclusions are embedded in matrix that can be square or rhomboidal, as depicted in figure 4.1. For the perfectly centered fiber, the horizontal eccentricity e is null, while for the eccentric fiber, the horizontal eccentricity is e=1.5 mm.

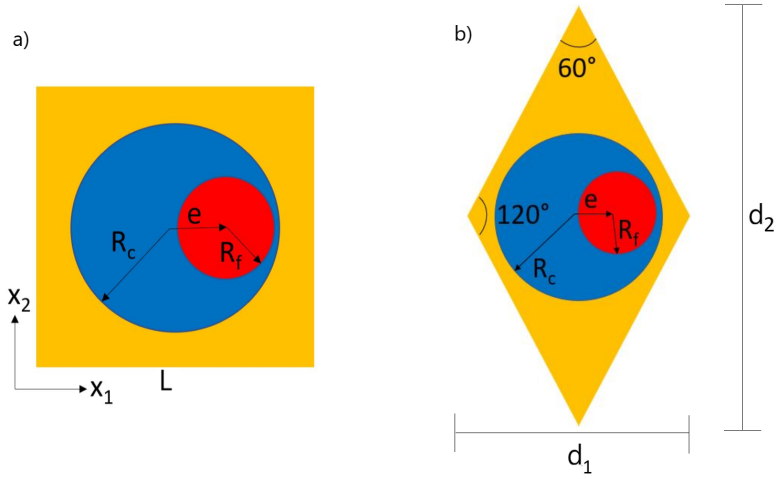

Figure 4.1. a) Square unit cell with eccentric fiber b) Rhomboidal unit cell with eccentric fiber

We consider also a rhomboidal shape for the matrix, having the same surface of the square one, because we will perform significant comparison between the two.

The geometrical and material properties are listed in the table 4.1.

Table 4.1. Geometrical and material properties

Constituents	E [MPa]	ν [-]	ρ [kg/m^3]
Matrix (m) - Epoxy (L=21 mm d_1=22.56 mm d_2=39.08 mm)	3600	0.37	1180
Coating (c) - Rubber (R_c=7.5 mm)	0.118	0.469	1300
Fiber (f) - Lead (R_f=5 mm)	14000	0.42	11340

4.1 Effective stiffness

4.1.1 Square unit cell with circular inclusions

For the homogenized stiffness of the square unit cell with circular inclusions, the domain to consider in the plane $x_1 - x_2$ is only the matrix, as obtained from the homogenization approach (section 3.3). Figure 4.2 shows the domain taken into consideration.

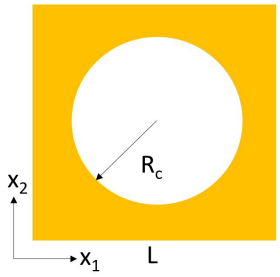

Figure 4.2. Square unit cell of the periodic media with holes instead of inclusions

The components of the effective stiffness tensor are given by equation (3.21). The anelastic strain $\boldsymbol{e}_i \odot \boldsymbol{e}_j$ is imposed in COMSOL Multiphysics with periodicity conditions on the opposite sides of the cell, as defined in the matrix cell problem (3.17). With a surface integration over the matrix area, it is possible to take out the averaged stress tensor that can be divided by the total area of the cell in order to obtain the effective stiffness tensor. In the plane $x_1 - x_2$, the components of the effective stiffness tensor can be expressed, according to the Voigt's notation, as:

$$[\mathbb{D}^0] = \begin{bmatrix} D^0_{1111} & D^0_{1122} & D^0_{1112} \\ D^0_{2211} & D^0_{2222} & D^0_{2212} \\ D^0_{1211} & D^0_{1222} & D^0_{1212} \end{bmatrix} \tag{4.1}$$

In this case, the numerical values obtained are:

$$[\mathbb{D}^0] = \begin{bmatrix} 1.8003e+09 & 5.4683e+08 & 0 \\ 5.4683e+08 & 1.8003e+09 & 0 \\ 0 & 0 & 2.6544e+08 \end{bmatrix} \text{Pa} \tag{4.2}$$

Even if the unit cell is doubly symmetric, which implies $D^0_{1111} = D^0_{2222}$, it can be observed that $\mathbb{D}^0$ is anisotropic.

Validation of the effective stiffness With reference to the square cell, in order to check if the homogenized stiffness is accurate, it is possible to compare the real model with the homogenized one. This comparison is here performed through two static tests simulated with COMSOL Multiphysics:

- a tension test along direction x_1
- a non-pure shear test

Tension test along direction x_1 For the real model, a 10×10 pattern with holes is considered. The material properties assigned to the pattern are related to the epoxy matrix. The boundary conditions are:

- null horizontal displacement on the left side
- null vertical displacement on the lower point of the left side
- unitary horizontal displacement at the right side

Through finite element analysis, we compute and compare the following quantities:

- the averaged vertical displacement at the upper side
- the total horizontal reaction at the right side
- the elastic strain energy of the whole domain

For the homogenized model, the geometry is equal to the real one without holes. The important modification is related to the material properties; in fact, the anisotropic effective stiffness tensor, obtained before in equation (4.2), is introduced to the model. The boundary conditions and outputs are defined as in the real model. The figure 4.3 shows the contour of displacement along x_1 for the real model and for the homogenized one. The table 4.2 resumes the numerical values of the outputs.

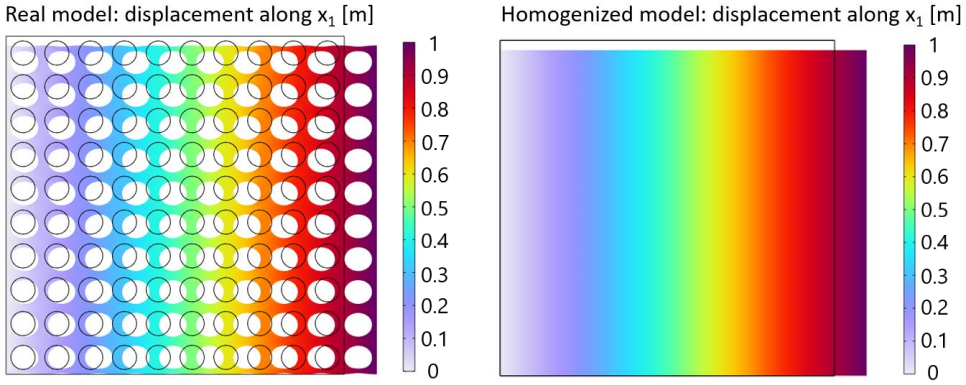

Figure 4.3. Tension test along direction x_1 for the square cell: comparison of the contour of displacement along x_1 between real and homogenized model

Table 4.2. Tension test along direction x_1 for the square cell: outputs

	Real model	Homogenized model	$\overline{e}$[%]
Vertical displacement at the upper side [m]	-0.30489	-0.30374	0.38
Horizontal reaction at the right side [N]	1.6168e+09	1.6342e+09	1.06
Elastic strain energy [J/m]	8.0842e+08	8.1710e+08	1.06

The relative errors $\overline{e}$ are very low and, thus, the effective stiffness provided by homogenization is accurate.

Non-pure shear test For the real model, a 10×10 pattern with holes is considered. The material properties assigned to the pattern are related to the epoxy matrix. In a first case, the boundary conditions are:

- null horizontal and vertical displacement on the left side
- unitary vertical displacement at the right side

Through finite element analysis, we compute and compare the following quantities:

- the averaged vertical displacement at the upper side
- the total vertical reaction at the right side
- the elastic strain energy of the whole domain

For the homogenized model, the geometry is equal to the real one without holes. The important change is related to the material properties; in fact, the anisotropic effective stiffness tensor (4.2) is introduced to the model. The boundary conditions and outputs are defined as in the real model. Table 4.3 resumes the numerical values of the outputs. Figure 4.4 shows the contour of displacement along x_2 for the real model and for the homogenized one.

Table 4.3. Non-pure shear test for the square cell: outputs (case 1)

	Real model	Homogenized model	$\overline{e}$[%]
Vertical displacement at the upper side [m]	0.46025	0.46199	0.38
Vertical reaction at the right side [N]	1.4809e+08	1.4762e+08	0.32
Elastic strain energy [J/m]	7.4046e+07	7.3808e+07	0.32

The relative errors $\overline{e}$ are very low and, therefore, the effective stiffness provided by homogenization is accurate.

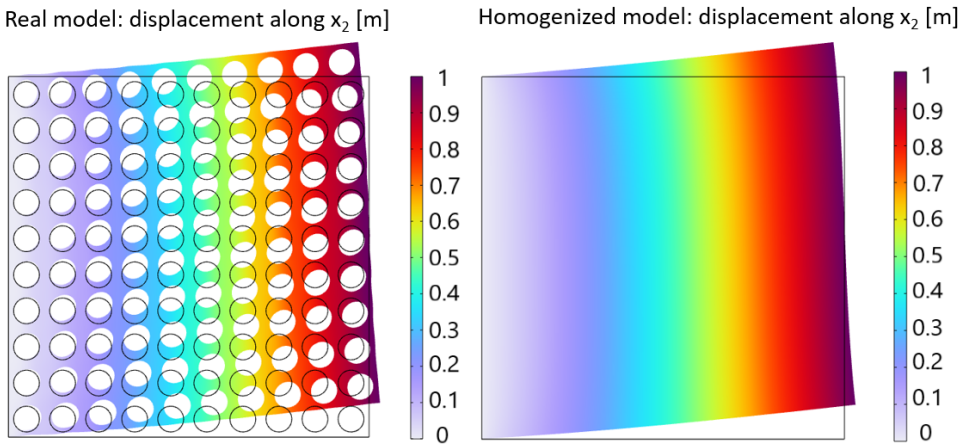

Figure 4.4. Non-pure shear test for the square cell: comparison of the contour of displacement along x_2 between real and homogenized model (case 1)

Moreover, with respect to the previous case, i.e., tension test along direction x_1, there is a modification on the constraints applied on the left side, whereas the number of cells is maintained equal. For this first non-pure shear test, if the vertical displacement on the left side is not null, with a 10×10 pattern, the relative errors are very high. This lead to a consideration about the number of cells that have to be used in order to obtain low relative errors, maintaining the same costraints of the previous case, i.e., tension test along direction x_1, on the left side. Therefore, a second non-pure shear test consists on using the same data of the first one, but with null vertical displacement only on the lower point of the left side. The geometrical pattern, used for having low relative errors, is now 40×40.

Figure 4.5 shows the contour of displacement along x_2 for the real model and for the homogenized one. Table 4.4 resumes the numerical values of the outputs.

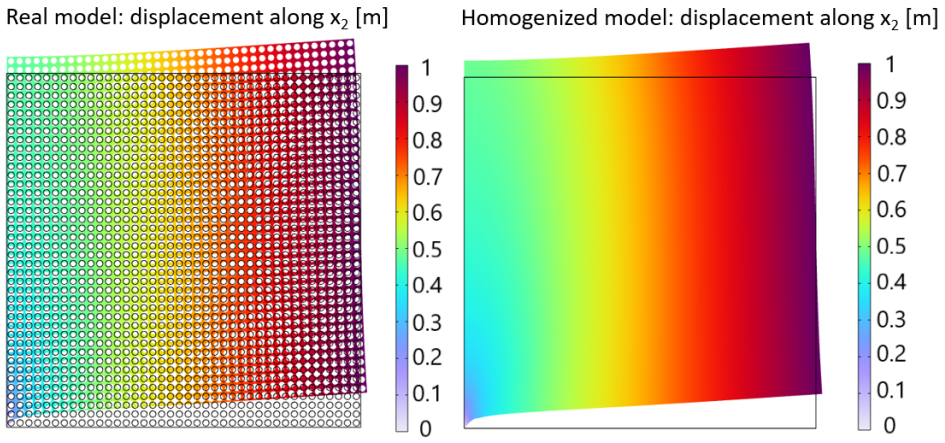

Figure 4.5. Non-pure shear test for the square cell: comparison of the contour of displacement along x_2 between real and homogenized model (case 2)

Table 4.4. Non-pure shear test for the square cell: outputs (case 2)

	Real model	Homogenized model	$\overline{e}$[%]
Vertical displacement at the upper side [m]	0.68697	0.69188	0.71
Vertical reaction at the right side [N]	9.0249e+07	8.9048e+07	1.33
Elastic strain energy [J/m]	4.5125e+07	4.4524e+07	1.34

The relative errors $\overline{e}$ are very low and, thus, the effective stiffness provided by homogenization is accurate.

4.1.2 Rhomboidal unit cell with circular inclusions

As for the square unit cell with circular inclusions, also for the homogenized stiffness of the rhomboidal one, the domain to consider in the plane $x_1 - x_2$ is only the matrix. Figure 4.6 shows the domain taken into consideration.

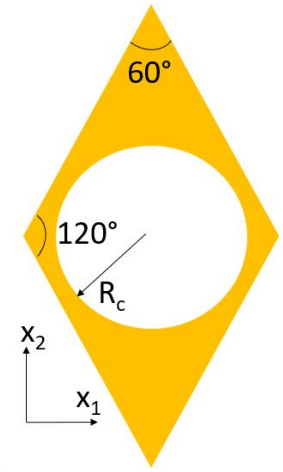

Figure 4.6. Rhoboidal unit cell of the periodic media with holes instead of inclusions

The procedure for obtaining the components of the effective stiffness tensor is the same of the one developed for the square unit cell (explained in subsection 4.1.1). In this case, the numerical values obtained for the effective stiffness tensor are:

$$[\mathbb{D}^0] = \begin{bmatrix} 1.6399e+09 & 7.4186e+08 & 0 \\ 7.4186e+08 & 1.6399e+09 & 0 \\ 0 & 0 & 4.4902e+08 \end{bmatrix} \text{Pa} \tag{4.3}$$

It can be observed that $\mathbb{D}^0$ is anisotropic but with $D^0_{1111} = D^0_{2222}$.

Validation of the effective stiffness With reference to the rhomboidal cell, in order to check if the homogenized stiffness is accurate, it is possible to compare the real model with the homogenized one. This comparison is here performed through three static tests simulated with COMSOL Multiphysics:

- a tension test along direction x_1
- a tension test along direction x_2
- a non-pure shear test

Tension test along direction x_1 For the real model, a 10×10 pattern with holes is considered. The material properties assigned to the pattern are related to the epoxy matrix. The boundary conditions and the outputs are the ones defined in subsection 4.1.1 for the tension test along direction x_1.

For the homogenized model, the geometry is equal to the real one without holes. The important modification is related to the material properties; in fact, the anisotropic effective stiffness tensor, obtained before in equation (4.3), is introduced to the model. The boundary conditions and outputs are defined as in the real model. The figure 4.7 shows the contour of displacement along x_1 for the real model and for the homogenized one. The table 4.5 resumes the numerical values of the outputs.

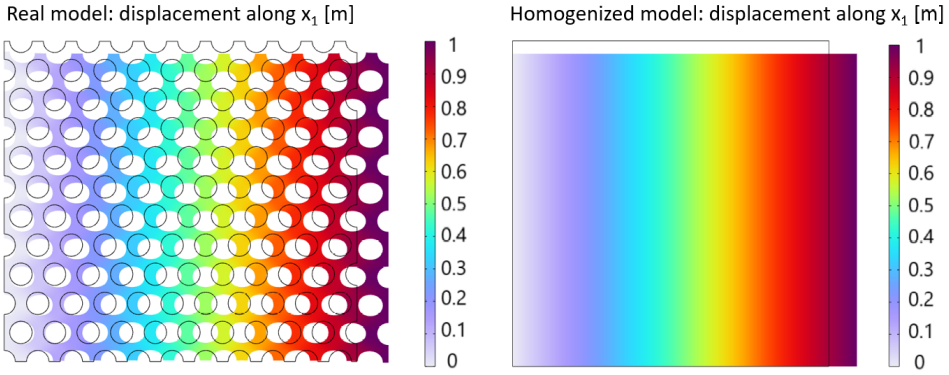

Figure 4.7. Tension test along direction x_1 for the rhomboidal cell: comparison of the contour of displacement along x_1 between real and homogenized model

Table 4.5. Tension test along direction x_1 for the rhomboidal cell: outputs

	Real model	Homogenized model	$\overline{e}$[%]
Vertical displacement at the upper side [m]	-0.37742	-0.41037	8.03
Horizontal reaction at the right side [N]	1.2588e+09	1.1832e+09	6.01
Elastic strain energy [J/m]	6.2939e+08	5.9159e+08	6.01

The relative errors $\overline{e}$ are not so low and they are higher than the ones obtained for the square cell (table 4.2). This is due to the change of the geometrical pattern that influences the static response, under specific costraints and displacements. A solution could be the addition of more cells in order to decrease the relative errors.

Tension test along direction x_2 For the real model, a 20×20 pattern with holes is considered. The material properties assigned to the pattern are related to the epoxy matrix. The boundary conditions are:

- null vertical displacement on the lower side
- null horizontal displacement on the right point of the lower side
- unitary vertical displacement at the upper side

Through finite element analysis, we compute and compare the following quantities:

- the averaged horizontal displacement at the left side
- the total vertical reaction at the upper side
- the elastic strain energy of the whole domain

For the homogenized model, the geometry is equal to the real one without holes. The important modification is related to the material properties; in fact, the anisotropic effective stiffness tensor, obtained before in equation (4.3), is introduced to the model. The boundary conditions and outputs are defined as in the real model. The figure 4.8 shows the contour of displacement along x_2 for the real model and for the homogenized one. The table 4.6 resumes the numerical values of the outputs.

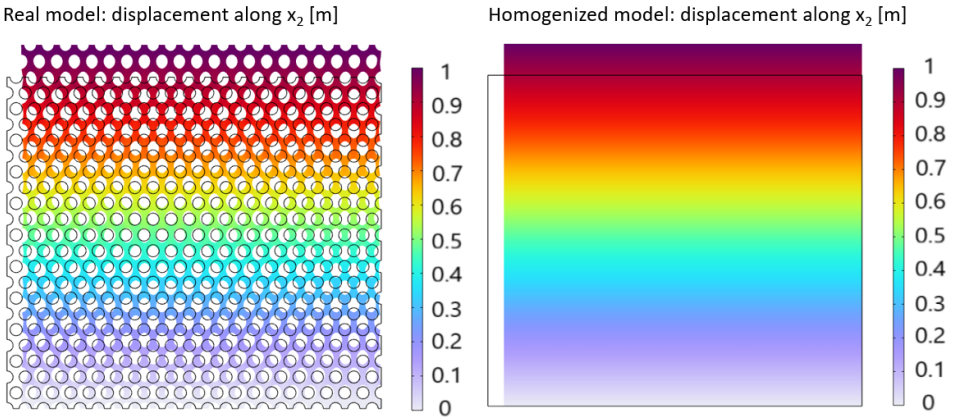

Figure 4.8. Tension test along direction x_2 for the rhomboidal cell: comparison of the contour of displacement along x_2 between real and homogenized model

Table 4.6. Tension test along direction x_2 for the rhomboidal cell: outputs

	Real model	Homogenized model	$\bar{e}$[%]
Horizontal displacement at the left side [m]	0.47457	0.50993	6.93
Vertical reaction at the upper side [N]	1.5393e+09	1.4702e+08	4.49
Elastic strain energy [J/m]	7.6967e+08	7.3512e+08	4.49

The relative errors are lower than the previous case, i.e., tension test along direction x_1, due to the increasing number of cells but they are higher with respect to ones obtained for the square cell (table 4.2).

Non-pure shear test For the real model, a 20×20 pattern with holes is considered. The material properties assigned to the pattern are related to the epoxy matrix. The boundary conditions and the outputs are the ones defined in subsection 4.1.1 for the first non-pure shear test (case 1).

For the homogenized model, the geometry is equal to the real one without holes. The important modification is related to the material properties; in fact, the anisotropic effective stiffness tensor, obtained before in equation (4.3), is introduced to the model. The boundary conditions and outputs are defined as in the real model. The figure 4.9 shows the contour of displacement along x_2 for the real model and for the homogenized one. The table 4.7 resumes the numerical values of the outputs.

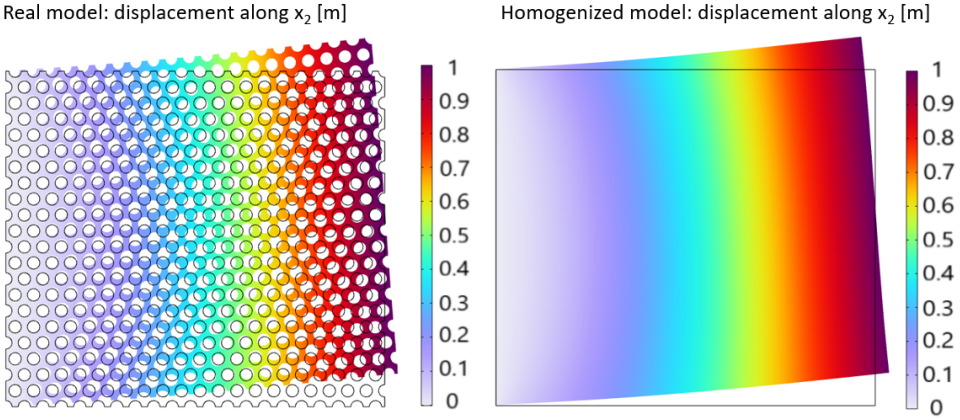

Figure 4.9. Non-pure shear test for the rhomboidal cell: comparison of the contour of displacement along x_2 between real and homogenized model

Table 4.7. Non-pure shear test for the rhomboidal cell: outputs

	Real model	Homogenized model	$\overline{e}$[%]
Vertical displacement at the upper side [m]	0.45223	0.44757	1.03
Vertical reaction at the right side [N]	1.5219e+08	1.3952e+08	8.33
Elastic strain energy [J/m]	7.6096e+07	6.9758e+07	8.33

The relative errors for the reaction and the elastic strain energy are the highest found in all the analysis and this is especially due to the type of test applied to the model. On the other side, for the displacement, the relative error is very low.

4.2 Effective mass density

For the effective mass density, we can make reference to the coating and fiber only, as defined in the homogenization approach (subsections 3.4 and 3.5). Figure 4.10 shows the domain taken into consideration.

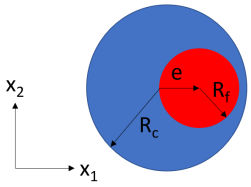

Figure 4.10. Circular inclusions: coating with eccentric fiber

A first scenario that can be analyzed is the one with a perfectly centered fiber with respect to the coating and with reference to figure 4.10, the horizontal eccentricity e is null. A second scenario consists on an eccentric fiber with respect to the coating and with reference to figure 4.10, the horizontal eccentricity is e=1.5 mm.

4.2.1 Perfectly centered fiber

In this first scenario in which the fiber is perfectly centered, COMSOL Multiphysics is employed for computing the numerical solution of the inclusion cell problems (3.29) and (3.31). Then, the evaluation of the effective dynamic mass density is performed through equation (3.37).

Since $x_1 - x_2$ (axis of symmetry) is the principal mass reference system, the extra-diagonal components of equation (3.37) are null. Due to null eccentricity and perfect symmetry, the diagonal components of equation (3.37) are equal, i.e., $\rho^0_{11} = \rho^0_{22} = \rho^0$. In this case, the effective mass density tensor is isotropic.

In the case of perfectly centered fiber, i.e., null horizontal eccentricity, figure 4.11 shows the normalized effective mass density obtained through equation (3.37).

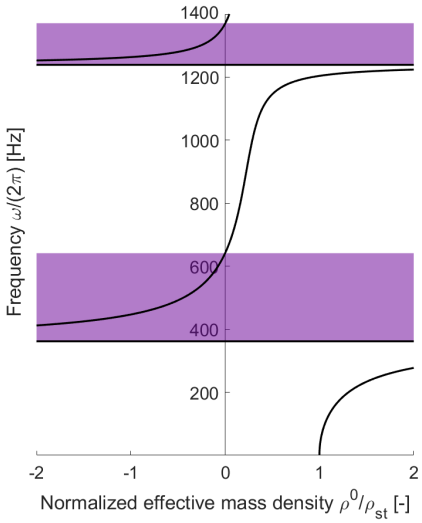

Figure 4.11. Normalized effective mass density for the perfectly centered fiber (null horizontal eccentricity)

With reference to figure 4.11, the frequency intervals shaded in purple are the ones in which the normalized effective mass density is negative.

4.2.2 Eccentric fiber

A second scenario is the case in which the fiber has an eccentricity, e.g. horizontal, with respect to the center of the cell. Also in this case, COMSOL Multiphysics is employed for computing the numerical solution of the inclusion cell problems (3.29) and (3.31). Then, the evaluation of the effective dynamic mass density is performed through equation (3.37).

$x_1 - x_2$ is the principal mass reference system and, thus, the extradiagonal components of equation (3.37) are null. In this case, the effective mass density tensor is anisotropic, i.e., $\rho^0_{11} \neq \rho^0_{22}$.

In the case of eccentric fiber, i.e., horizontal eccentricity e=1.5 mm, figure 4.12 shows the normalized effective mass density obtained through equation (3.37).

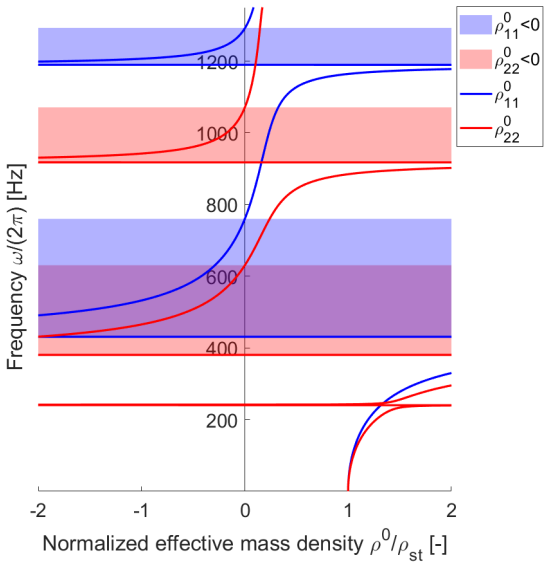

Figure 4.12. Normalized effective mass density for the eccentric fiber (horizontal eccentricity e=1.5 mm)

With reference to figure 4.12, three different shaded regions can be distinguished:

- blue zone, in which $\rho^0_{11} < 0$ and $\rho^0_{22} > 0$
- red zone, in which $\rho^0_{22} < 0$ and $\rho^0_{11} > 0$
- purple zone, in which $\rho^0_{11} < 0$ and $\rho^0_{22} < 0$.

4.3 Band-gaps prediction by Bloch-Floquet analysis

In this section, we compare the normalized effective mass densities with the dispersion curves obtained through Bloch-Floquet analysis. The procedure for obtaining the dispersion curves and the theoretical framework for Bloch-Floquet analysis is explained in the section 2.2. The aim is to verify that the total band-gaps predicted by Bloch-Floquet analysis are in good agreement with the ones obtained by the normalized effective mass densities.

4.3.1 Perfectly centered fiber

With reference to the case of perfectly centered fiber, the domains to consider for defining the dispersion curves are shown in figure 4.1 but with null horizontal eccentricity. The dispersion curves, obtained numerically with COMSOL Multiphysics, are defined for the square and the rhomboidal unit cell. The Bloch-Floquet problem (2.26) is solved numerically with COMSOL Multiphysics through an inverse solution method, as described in section 2.2.

Figure 4.13 shows, on the left, the dispersion curves of the square unit cell with perfectly centered fiber, obtained through Bloch-Floquet analysis. In the same figure, in the center, there are the dispersion curves of the rhomboidal unit cell with perfectly centered fiber, obtained through Bloch-Floquet analysis. On the right of the same figure, there is the normalized effective mass density for the perfectly centered fiber, described in the subsection 4.2.1.

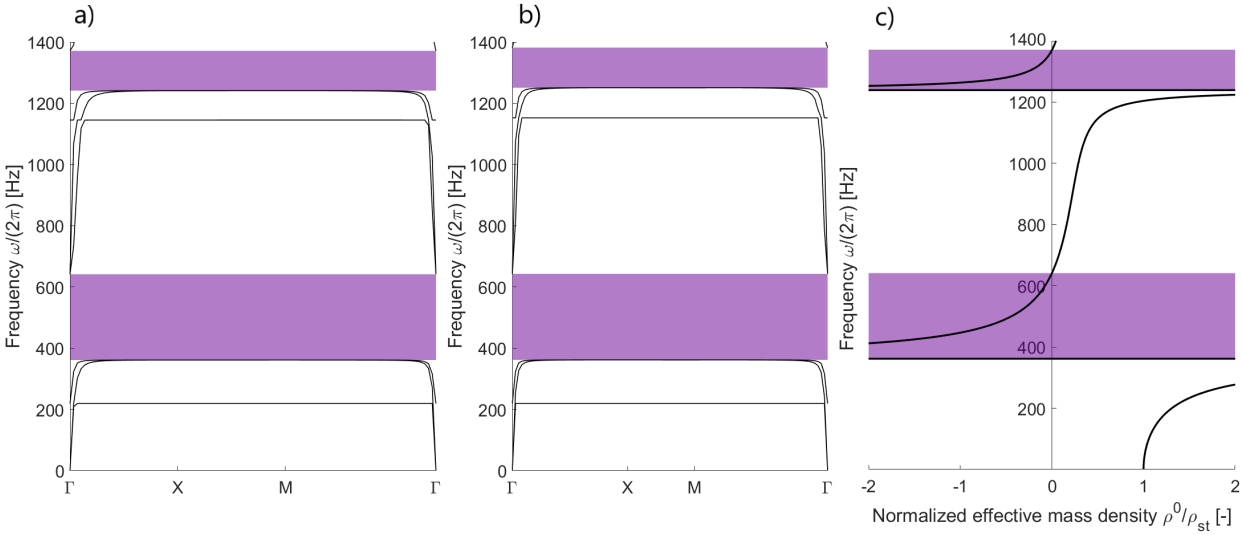

Figure 4.13. a) Dispersion curves of the square unit cell with perfectly centered fiber b) Dispersion curves of the rhomboidal unit cell with perfectly centered fiber c) Normalized effective mass density for the perfectly centered fiber

With reference to figure 4.13, the frequency intervals shaded in purple are the total band-gaps. For the dispersion curves, these bands represent the frequency intervals in which waves cannot propagate, whereas for the plot on the right, the

frequency intervals in which the normalized effective density is negative. Comparing the plots, from a qualitative point of view, these zones are in good agreement.

4.3.2 Eccentric fiber

With reference to the case of eccentric fiber, the domains to consider for defining the dispersion curves are shown in figure 4.1. The dispersion curves, obtained numerically with COMSOL Multiphysics, are defined for the square and the rhomboidal unit cell. The Bloch-Floquet problem (2.26) is solved numerically with COMSOL Multiphysics through an inverse solution method, as described in section 2.2.

Figure 4.14 shows, on the left, the dispersion curves of the square unit cell with eccentric fiber, obtained through Bloch-Floquet analysis. In the same figure, in the center, there are the dispersion curves of the rhomboidal unit cell with eccentric fiber, obtained through Bloch-Floquet analysis. On the right of the same figure, there is the normalized effective mass density for the eccentric fiber, described in the subsection 4.2.2.

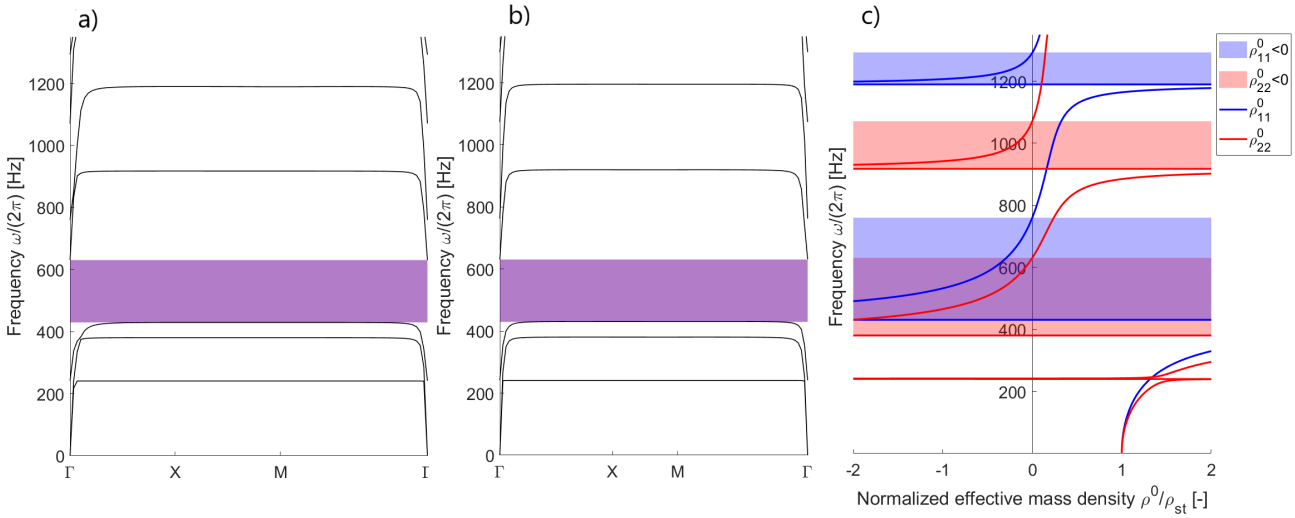

Figure 4.14. a) Dispersion curves of the square unit cell with eccentric fiber b) Dispersion curves of the rhomboidal unit cell with eccentric fiber c) Normalized effective mass density for the eccentric fiber

With reference to figure 4.14, the frequency intervals shaded in purple are the total band-gaps. For the dispersion curves, these bands represent the frequency intervals in which waves cannot propagate, whereas for the plot on the right, the frequency intervals in which $\rho^0_{11} < 0$ and $\rho^0_{22} < 0$. Comparing the plots, from a qualitative point of view, these zones are in good agreement. With reference to figure 4.14 c), the regions shaded in red and blue, in which ρ^0_{11} and ρ^0_{22} have different sign, represent the polarization bands.

Dispersion surfaces for the square unit cell with eccentric fiber Due to the eccentricity of the fiber, in order to check that the path $\Gamma XM\Gamma$ along the IBZ is

sufficient to identify band-gaps, we reconstruct the dispersion surface on the whole FBZ. The latter, in this case, is a square of side $2\pi/L$. To obtain the dispersion surfaces, a numerical Bloch-Floquet analysis can be performed with COMSOL Multiphysics. The Bloch-Floquet periodicity conditions are applied on the opposite sides of the cell. Figure 4.15 shows the dispersion surfaces in a 3D view, on the FBZ of the square unit cell.

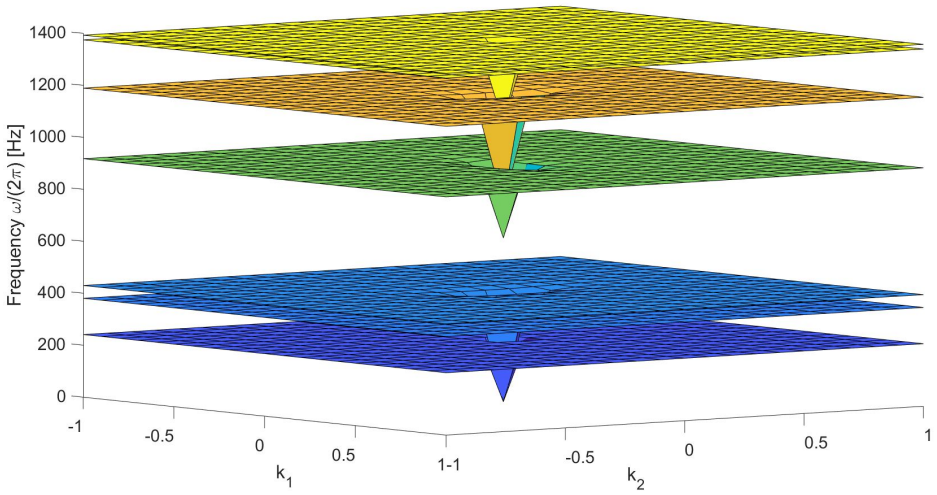

Figure 4.15. Dispersion surfaces for the square unit cell with eccentric fiber on FBZ, 3D view

At this point, the dispersion curves obtained along the IBZ can be compared with the dispersion surfaces represented in a lateral view, as shown in figure 4.16. The lateral view of figure 4.16 (b) is defined in order to facilitate the comparison with the dispersion curves along the IBZ.

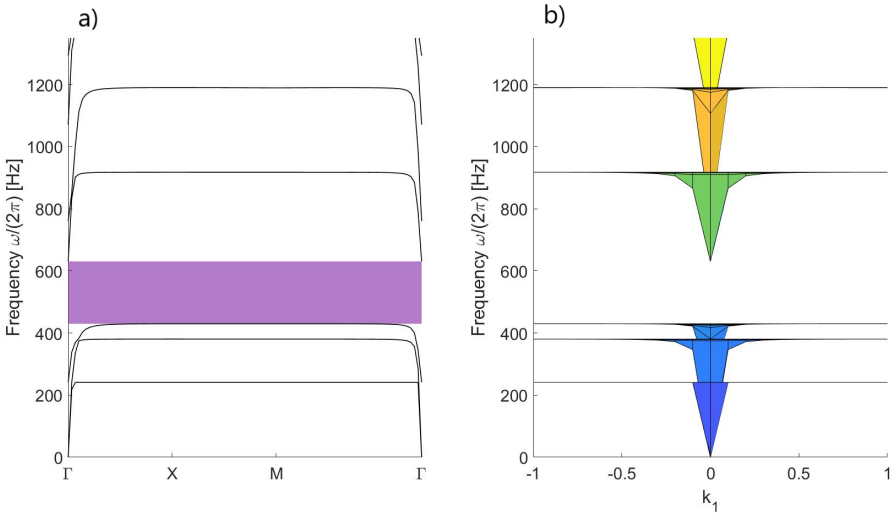

Figure 4.16. Comparison between dispersion curves along the IBZ a) and dispersion surfaces on FBZ, lateral view b) for the square unit cell with eccentric fiber

Observing figure 4.16, the total band-gap in purple and the other resonance frequencies are equal in both of the graphs. Even if the fiber is eccentric and the unit cell is no more doubly symmentic, the dispersion curves along the IBZ are sufficient for the identification of band-gaps.

Dispersion surfaces for the rhomboidal unit cell with eccentric fiber As for the square unit cell, due to the eccentricity of the fiber, in order to check that the path $\Gamma XM\Gamma$ along IBZ is sufficient to identify band-gaps, we reconstruct the dispersion surface on the whole FBZ. The latter, in this case, is a regular hexagon of side $4\pi/3d_1$. To obtain the dispersion surfaces, a numerical Bloch-Floquet analysis can be performed with COMSOL Multiphysics. The Bloch-Floquet periodicity conditions are applied on the opposite sides of the cell. Figure 4.17 shows the dispersion surfaces in a 3D view, on the FBZ of the rhomboidal unit cell.

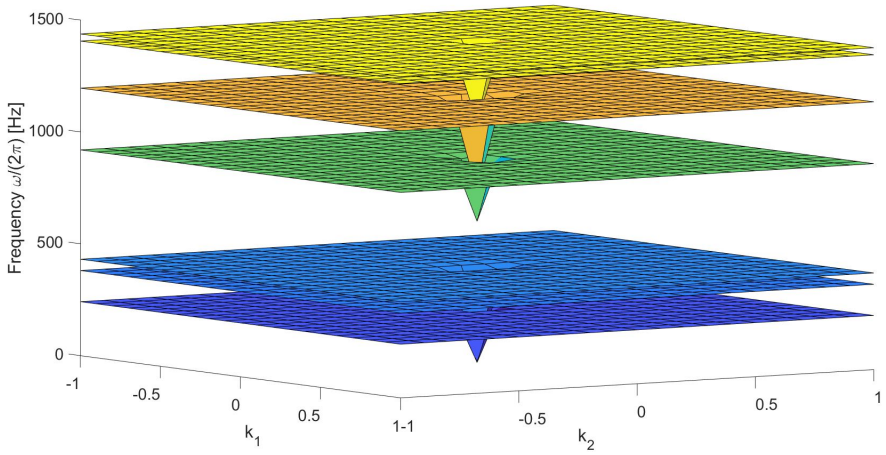

Figure 4.17. Dispersion surfaces for the rhomboidal unit cell with eccentric fiber on FBZ, 3D view

At this point, the dispersion curves obtained along the IBZ can be compared with the dispersion surfaces represented in a lateral view, as shown in figure 4.18. The lateral view of figure 4.18 (b) is defined in order to facilitate the comparison with the dispersion curves along the IBZ.

Observing figure 4.18, the total band-gap in purple and the other resonance frequencies are equal in both of the graphs. Even if the fiber is eccentric and the unit cell is no more doubly symmentic, the dispersion curves along the IBZ are sufficient for the identification of band-gaps.

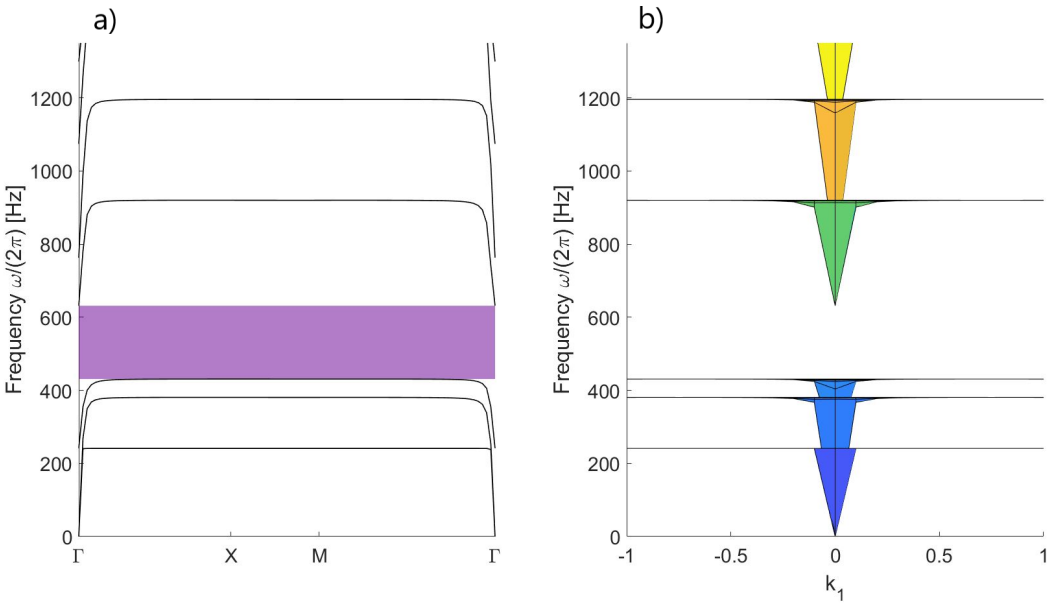

Figure 4.18. Comparison between dispersion curves along the IBZ a) and dispersion surfaces on FBZ, lateral view b) for the rhomboidal unit cell with eccentric fiber

4.4 Effective dispersion properties

In this section, exploiting the effective properties computed in sections 4.1 and 4.2, we discuss the effective dispersion behaviour of the equivalent homogenized media. In particular, this discussion will be focused on a comparison of phase velocities and polarization vectors involved in two different geometrical pattern of the unit metamaterial cell: square and rhomboidal. The theoretical framework about the effective dispersion properties is discussed in the section 3.6.

4.4.1 Square unit cell with eccentric fiber

We consider the square unit cell with eccentric fiber, i.e., horizontal eccentricity e=1.5 mm (figure 4.1 (a)). The anisotropic effective stiffness tensor is the one obtained in equation (4.2). In this case, the components of the effective acoustic tensor, through equation (3.42), are given by:

$$[\boldsymbol{Q}^0] = \begin{bmatrix} D^0_{1111}n_1^2 + D^0_{1212}n_2^2 & (D^0_{1122} + D^0_{1212})n_1n_2 \\ (D^0_{1122} + D^0_{1212})n_1n_2 & D^0_{1212}n_1^2 + D^0_{2222}n_2^2 \end{bmatrix} \tag{4.4}$$

With reference to the section 3.6, we focus on the polarization bands (case 3), where $\rho^0_I = \rho^0_{11}$ and $\rho^0_{II} = \rho^0_{22}$ have different sign.

In a first scenario, with reference to figure 4.12, we consider the polarization band in which $\rho^0_{11} < 0$ and $\rho^0_{22} > 0$. A first frequency can be selected when the contrast between the two diagonal components of the effective mass density tensor is low.

For example, at frequency $\omega/2\pi$=1270 Hz, the effective mass tensor is given by the following entries:

$$[\boldsymbol{\rho}^0] = \begin{bmatrix} -175.65 & 0 \\ 0 & 417.59 \end{bmatrix} \text{kg/m}^3 \tag{4.5}$$

with $|\rho^0_{11}/\rho^0_{22}| = 0.42$.

A second frequency can be selected when the contrast between the two diagonal components of the effective mass density tensor is high. For example at frequency $\omega/2\pi$=1200 Hz, the effective mass tensor is given by the following entries:

$$[\boldsymbol{\rho}^0] = \begin{bmatrix} -5.24e+03 & 0 \\ 0 & 325.85 \end{bmatrix} \text{kg/m}^3 \tag{4.6}$$

with $|\rho^0_{11}/\rho^0_{22}| = 16.08$.

In these two selected frequencies, the effective dispersion relation (3.41) admits a unique real positive solution because c_1^2 and c_2^2 have opposite sign. This eigenvalue, from a physical point of view, is the phase velocity. The associated eigenvector is the polarization vector which is mainly aligned with the principal direction of positive mass. Figure 4.19 shows the two polar diagrams fixed at the two frequencies $\omega/2\pi$=1270 Hz and $\omega/2\pi$=1200 Hz. These polar diagrams show the phase velocities (black line) and the polarization directions (red line) within different propagation directions (blue line).

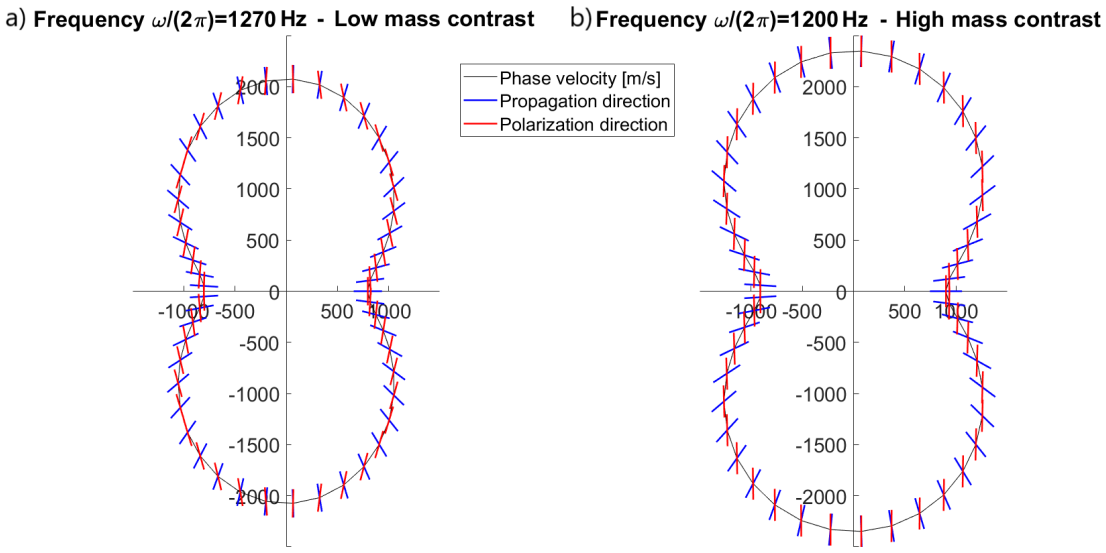

Figure 4.19. Square unit cell with eccentric fiber: phase velocities (black line) and polarization directions (red line) within different propagation directions (blue line) when $\rho^0_{11}<0$ and $\rho^0_{22}>0$. a) Low mass contrast b) High mass contrast

Since the effective stiffness and mass tensors are anisotropic, the magnitude of the phase velocity depends on the angle of propagation. A comment can be done on the polarization directions that, differently than an isotropic homogenous case

(figure 2.2), are not completely parallel or orthogonal to the propagation directions. This means that the propagating waves are not longiudinal or shear waves, but they belong to a mixed type of them. From the comparison between the two polar diagrams, it is possible to note that, when the mass contrast becomes higher (figure 4.19 (right)), the polarization directions tend to be fully verticalized. This lead to consider that the polarization directions are strongly depedent from the mass contrast in the effective mass density tensor. Moreover, with an higher mass contrast, the phase velocity's trend tend to expand but without changing the shape.

In a second scenario, with reference to figure 4.12, we consider the polarization band in which $\rho^0_{22} < 0$ and $\rho^0_{11} > 0$. A first frequency can be selected when the contrast between the two diagonal components of the effective mass density tensor is low. For example, at frequency $\omega/2\pi$=1000 Hz, the effective mass tensor is given by the following entries:

$$[\boldsymbol{\rho}^0] = \begin{bmatrix} 702.55 & 0 \\ 0 & -531.71 \end{bmatrix} \text{kg/m}^3 \tag{4.7}$$

with $|\rho^0_{22}/\rho^0_{11}| = 0.76$.

A second frequency can be selected when the contrast between the two diagonal components of the effective mass density tensor is high. For example at frequency $\omega/2\pi$=920 Hz, the effective mass tensor is given by the following entries:

$$[\boldsymbol{\rho}^0] = \begin{bmatrix} 491.56 & 0 \\ 0 & -3.26e+04 \end{bmatrix} \text{kg/m}^3 \tag{4.8}$$

with $|\rho^0_{22}/\rho^0_{11}| = 66.32$.

In these two selected frequencies, the effective dispersion relation (3.41) admits a unique real positive solution because c_1^2 and c_2^2 have opposite sign. This eigenvalue, from a physical point of view, is the phase velocity. The associated eigenvector is the polarization vector which is mainly aligned with the principal direction of positive mass. Figure 4.20 shows the two polar diagrams fixed at the two frequencies $\omega/2\pi$=1000 Hz and $\omega/2\pi$=920 Hz. These polar diagrams show the phase velocities (black line) and the polarization directions (red line) within different propagation directions (blue line).

With reference to figure 4.20, the polarization directions, with an higher mass contrast (figure 4.20 b), tend to be fully horizontalized.

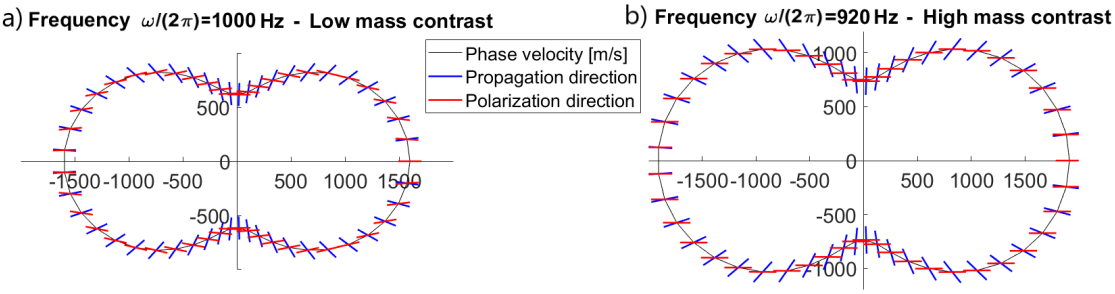

Figure 4.20. Square unit cell with eccentric fiber: phase velocities (black line) and polarization directions (red line) within different propagation directions (blue line) when $\rho^0_{22}<0$ and $\rho^0_{11}>0$. a) Low mass contrast b) High mass contrast

4.4.2 Rhomboidal unit cells with eccentric fiber

In this subsection, we compare the polar diagrams obtained with reference to four different geometrical configurations of the rhomboidal unit cell (figure 4.21). The matrix areas of these different configurations are kept equal to the one of the square unit cell, with no modifications on the areas of the coating and of the fiber.

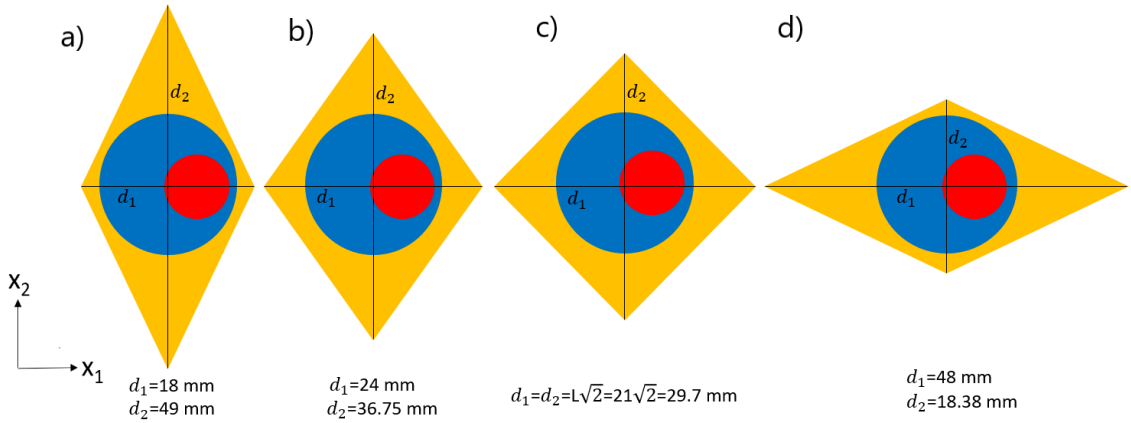

Figure 4.21. Rhmoboidal unit cells: geometrical configurations

As shown in 4.1.2 for the rhomboidal unit cell with angles at 60° and 120°, the procedure for obtaining the effective stiffness tensor can be performed also with these new geometrical configurations. In particular for the rhomboidal unit cell with d_1=18 mm and d_2=49 mm, the components of the anisotropic effective stiffness tensor are:

$$[\mathbb{D}^0] = \begin{bmatrix} 2.0605e+09 & 5.1685e+08 & 0 \\ 5.1685e+08 & 1.3919e+09 & 0 \\ 0 & 0 & 2.0489e+08 \end{bmatrix} \text{Pa} \tag{4.9}$$

For the rhomboidal unit cell with d_1=24 mm and d_2=36.75 mm:

$$[\mathbb{D}^0] = \begin{bmatrix} 1.5441e+09 & 8.0104e+08 & 0 \\ 8.0104e+08 & 1.6072e+09 & 0 \\ 0 & 0 & 5.0816e+08 \end{bmatrix} \text{Pa} \tag{4.10}$$

For the rhomboidal unit cell with d_1=d_2=29.7 mm (that is simply the square unit cell rotated by 45°):

$$[\mathbb{D}^0] = \begin{bmatrix} 1.4391e+09 & 9.0807e+08 & 0 \\ 9.0807e+08 & 1.4391e+09 & 0 \\ 0 & 0 & 6.2676e+08 \end{bmatrix} \text{Pa} \tag{4.11}$$

For the rhomboidal unit cell with d_1=48 mm and d_2=18.38 mm:

$$[\mathbb{D}^0] = \begin{bmatrix} 1.4439e+09 & 5.3878e+08 & 0 \\ 5.3878e+08 & 2.0249e+09 & 0 \\ 0 & 0 & 2.2844e+08 \end{bmatrix} \text{Pa} \tag{4.12}$$

The effective acoustic tensor must be defined as in equation (4.4) for all the four different cases.

With reference to the section 3.6, we focus on the polarization bands (case 3), where $\rho_I^0 = \rho_{11}^0$ and $\rho_{II}^0 = \rho_{22}^0$ have different sign.

In a first scenario, with reference to figure 4.12 (the horizontal eccentricity of the fiber is always e=1.5 mm), we consider the polarization band in which $\rho_{11}^0 < 0$ and $\rho_{22}^0 > 0$. The frequency is chosen at $\omega/2\pi$=1200 Hz. The anisotropic effective mass density tensor is defined in equation (4.6) and it is equal for all the four cases.

In this selected frequency, the effective dispersion relation (3.41) admits a unique real positive solution because c_1^2 and c_2^2 have opposite sign. This eigenvalue, from a physical point of view, is the phase velocity. The associated eigenvector is the polarization vector which is mainly aligned with the principal direction of positive mass. Figure 4.22 shows the four polar diagrams fixed at the frequency $\omega/2\pi$=1200 Hz. These polar diagrams show the phase velocities (black line) and the polarization directions (red line) within different propagation directions (blue line).

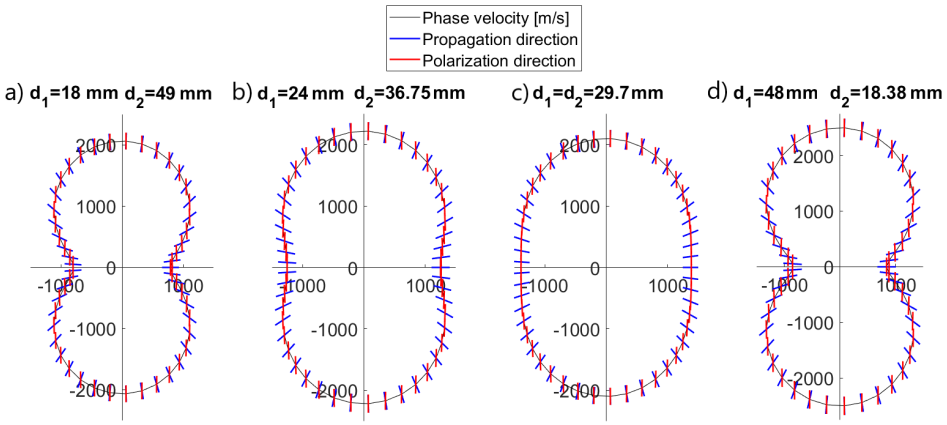

Figure 4.22. Rhomboidal unit cells with eccentric fiber: phase velocities (black line) and polarization directions (red line) within different propagation directions (blue line) when ρ_{11}^0<0 and ρ_{22}^0>0 (frequency $\omega/2\pi$=1200 Hz)

With reference to figure 4.22, it is possible to observe that the shape of phase velocities changes within different geometrical configurations of the rhomboidal unit cell. This is especially due to the variation of the effective stiffness tensor for the four different cases. It can be noticed that the angle of propagation in which there is the more relevant change of shape of the phase velocity is θ=0°. We can analyze the equation (3.41) by components. At this angle, the effective acoustic tensor is diagonal, i.e., $(D^0_{1122} + D^0_{1212})n_1n_2 = 0$ with $n_2 = \sin\theta = \sin 0 = 0$. Since only $\rho^0_{22}>0$, only the component $D^0_{1212}n_1^2 + D^0_{2222}n_2^2$ of the effective acoustic tensor must be taken into account. At this angle, the component of the effective stiffness tensor which is influent for the change of shape of the phase velocity is D^0_{1212}, i.e, $D^0_{1212}n_1^2 + D^0_{2222}n_2^2 = D^0_{1212}$ with $n_1 = \cos\theta = \cos 0 = 1$ and $n_2 = \sin\theta = \sin 0 = 0$. As shown in equations (4.9), (4.10), (4.11) and (4.12), the component D^0_{1212} increases from the first geometrical configuration to the third one but decreseas in the fourth one. In fact, phase velocity, at a null angle of propagation, increases from the first to the third case and but decreases in the fourth geometrical case.

At frequency $\omega/2\pi$=1200 Hz, another interesting case is the one in which is possible to compare the polar diagram of figure 4.19 b) and the polar diagram of figure 4.22 c). The first one represents the polar diagram with reference to the square unit cell and the second one with reference to the square unit cell rotated by 45°. The substantial difference between these two cases is the position of the fiber; in fact, in the square unit cell its position is on the horizontal axis of symmetry, whereas in the rotated square cell is on the horizontal diagonal. This provoke a misalignment of both effective stiffness and effective mass density tensors. However, also in this comparison, with reference to equations (4.2) and (4.11), the component D^0_{1212} of the effective stiffness tensor influences the phase velocities' trends. In the case of rotated square unit cell, phase velocity at a null angle of propagation increases with respect to the one obtained with the square unit cell, as happen for the component D^0_{1212}.

In a second scenario, with reference to figure 4.12 (the horizontal eccentricity of the fiber is always e=1.5 mm), we consider the polarization band in which $\rho^0_{22} < 0$ and $\rho^0_{11} > 0$. The frequency is chosen at $\omega/2\pi$=920 Hz. The anisotropic effective mass density tensor is defined in equation (4.8) and it is equal for all the four cases.

In this selected frequency, the effective dispersion relation (3.41) admits a unique real positive solution because c_1^2 and c_2^2 have opposite sign. This eigenvalue, from a physical point of view, is the phase velocity. The associated eigenvector is the polarization vector which is mainly aligned with the principal direction of positive mass. Figure 4.23 shows the four polar diagrams fixed at the frequency $\omega/2\pi$=920 Hz. These polar diagrams show the phase velocities (black line) and the polarization directions (red line) within different propagation directions (blue line).

With reference to figure 4.23, also in these cases, the component D^0_{1212} of the effective stiffness tensor is the most influent for the phase velocity's trend. The only aspect to consider is that now the angle of propagation to consider is θ=90° and the component $D^0_{1111}n_1^2 + D^0_{1212}n_2^2$ of the effective acoustic tensor must be taken into account because only $\rho^0_{11} > 0$.

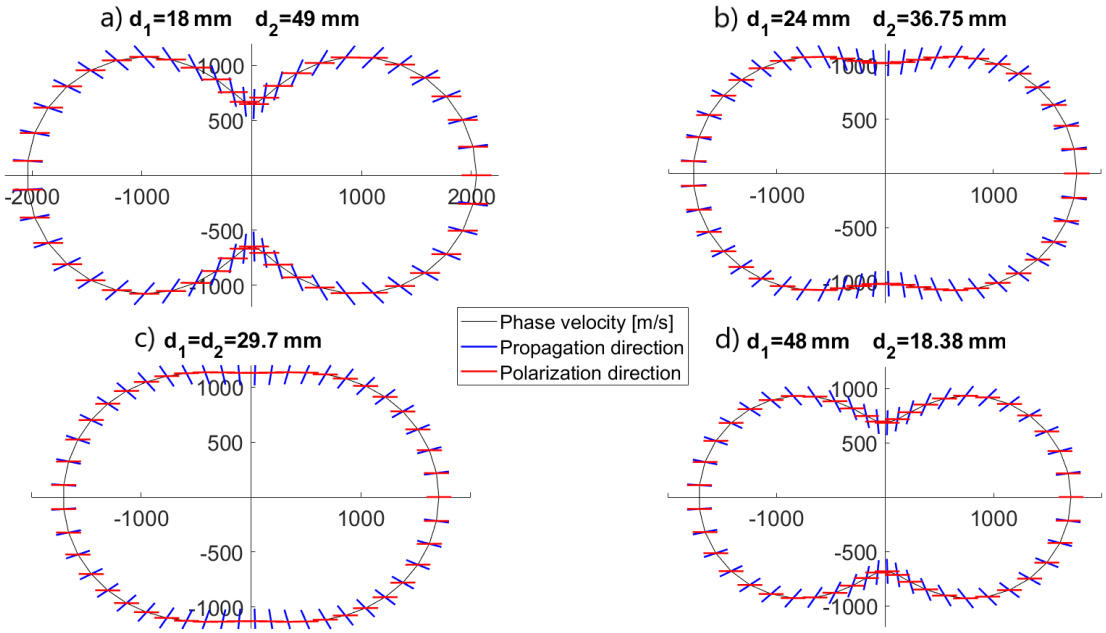

Figure 4.23. Rhomboidal unit cells with eccentric fiber: phase velocities (black line) and polarization directions (red line) within different propagation directions (blue line) when $\rho^0_{22}<0$ and $\rho^0_{11}>0$ (frequency $\omega/2\pi$=920 Hz)

4.5 Parametric discussion

Another purpose of this thesis is to analyze the effects of geometric parameters related to the metamaterial taken into consideration and study the influence of them on band gaps and polarization bands. In particular, the effects provided by the geometric parameters can be analyzed studying the variation of the effective mass density tensor's components. In order to obtain these components, COMSOL Multiphysics is used to implement the numerical evaluation described in subsection 4.2.2. The eccentricity of the fiber is horizontal along $\boldsymbol{e}_1$, $x_1 - x_2$ is the principal mass reference system and the components of the anisotropic effective mass density tensor are $\rho^0_{11}\neq\rho^0_{22}$.

A first scenario is devoted to the influence of the fiber radius R_f variation on ρ^0_{11} and ρ^0_{22}. The radius of the coating is fixed as $R_c = 7.5$ mm and the horizontal eccentricity of the fiber is kept at $e = 1.5$ mm. The scheme of this first case in shown in figure 4.24. From a practical point of view, it is possible to perform numerical evaluations of $\rho^0_{11}(\omega/2\pi)$ and $\rho^0_{22}(\omega/2\pi)$ for different values of the ratio R_f/R_c. For each value of the ratio R_f/R_c, three special frequency ranges could be distinguished:

- polarization band in which $\rho^0_{11} < 0$ and $\rho^0_{22} > 0$
- polarization band in which $\rho^0_{22} < 0$ and $\rho^0_{11} > 0$
- band gap in which $\rho^0_{11} < 0$ and $\rho^0_{22} < 0$.

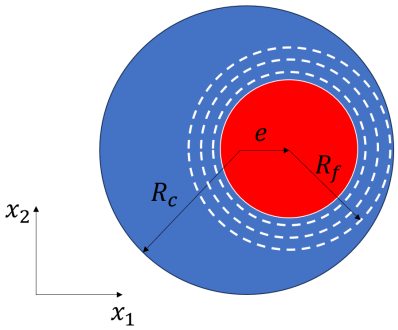

Figure 4.24. Fiber radius R_f variation, maintaining fixed the coating radius R_c and the horizontal eccentricity e of the fiber

Figure 4.25 shows, within some values of the ratio R_f/R_c, the qualitative trend of these particular frequency zones. The polarization bands in which $\rho^0_{11} < 0$ and $\rho^0_{22} > 0$ are depicted in blue, the polarization bands with $\rho^0_{22} < 0$ and $\rho^0_{11} > 0$ are represented in red and the band gaps in which $\rho^0_{11} < 0$ and $\rho^0_{22} < 0$ are the purple zones.

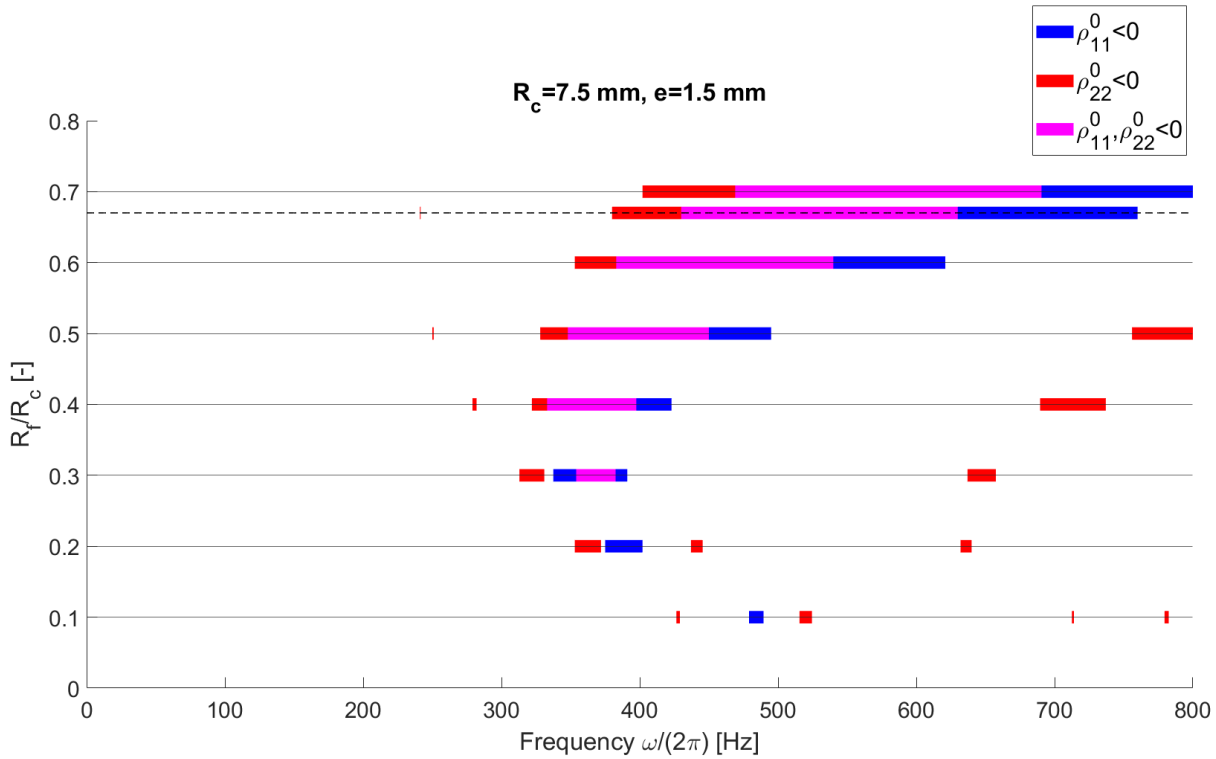

Figure 4.25. Frequency bands in which $\rho^0_{11} < 0$ and $\rho^0_{22} > 0$ (blue), $\rho^0_{22} < 0$ and $\rho^0_{11} > 0$ (red) and $\rho^0_{11} < 0$ and $\rho^0_{22} < 0$ (purple) for different values of the ratio R_f/R_c

With reference to figure 4.25, it is possible to notice a clear qualitative trend of the band gap, depicted in purple, within the ratio R_f/R_c. Increasing the latter, the polarization bands, represented in blue and red, tend to amplify their size in order to provide the band gap. For higher values of R_f/R_c, the band gap tends to

increase its size. In general, another aspect to observe is that the band gap, achieved by the intersection of the two polarization bands, occurs at higher frequencies as the ratio R_f/R_c increases. For low values of the ratio R_f/R_c, the polarization bands are fully separated with short sizes and the band gap is not achieved. The case in which $R_f/R_c = 0.8$ is not useful for real applications because the contact between the coating and the fiber occurs. Furthermore, the dashed line represents the original study case of figure 4.1 in which $R_f = 5$ mm and $R_f/R_c = 0.67$.

A second scenario is devoted to the influence of the horizontal eccentricity e variation, related to the fiber, on ρ^0_{11} and ρ^0_{22}. The radius of the coating is fixed as $R_c = 7.5$ mm and the radius of the fiber is kept at $R_f = 5$ mm. The scheme of this second case in shown in figure 4.26.

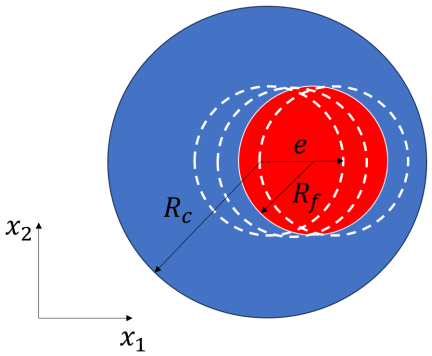

Figure 4.26. Horizontal eccentricity e variation, related to the fiber, maintaining fixed the coating radius R_c and the fiber radius R_f

From a practical point of view, it is possible to perform numerical evaluations of $\rho^0_{11}(\omega/2\pi)$ and $\rho^0_{22}(\omega/2\pi)$ for different values of the ratio e/e_{max}, where $e_{max} = R_c - R_f = 2.5$ mm is the horizontal eccentricity for which the contact between the coating and the fiber occurs.

Figure 4.27 shows, within some values of the ratio e/e_{max}, the qualitative trend of the polarization bands in which $\rho^0_{11} < 0$ and $\rho^0_{22} > 0$ (blue), of the polarization bands with $\rho^0_{22} < 0$ and $\rho^0_{11} > 0$ (red) and of the band gaps in which $\rho^0_{11} < 0$ and $\rho^0_{22} < 0$ (purple).

With reference to figure 4.27, it is possible to observe the qualitative trend of the band gap, depicted in purple, within the ratio e/e_{max}. Increasing the latter, the polarization bands, represented in blue and red, tend to be more separated with a lower possibility to provide the band gap. For higher values of e/e_{max}, the band gap tends to decrease its size. In general, another aspect to notice is that the band gap, achieved by the intersection of the two polarization bands, occurs at higher frequencies as the ratio e/e_{max} increases. For the ratio $e/e_{max} = 0$, the effective mass density tensor is isotropic, i.e., $\rho^0_{11} = \rho^0_{22} = \rho^0$, and, thus, only the band gap is achieved. A limit case is shown for the ratio $e/e_{max} = 0.99$, in which it can be observed that the polarization bands are fully separated and the band gap is not

provided. The case in which $e/e_{max} = 1$ is not useful in real applications because the contact between the coating and the fiber occurs. Moreover, the dashed line represents the original study case of figure 4.1 in which $e = 1.5$ mm and $e/e_{max} = 0.6$.

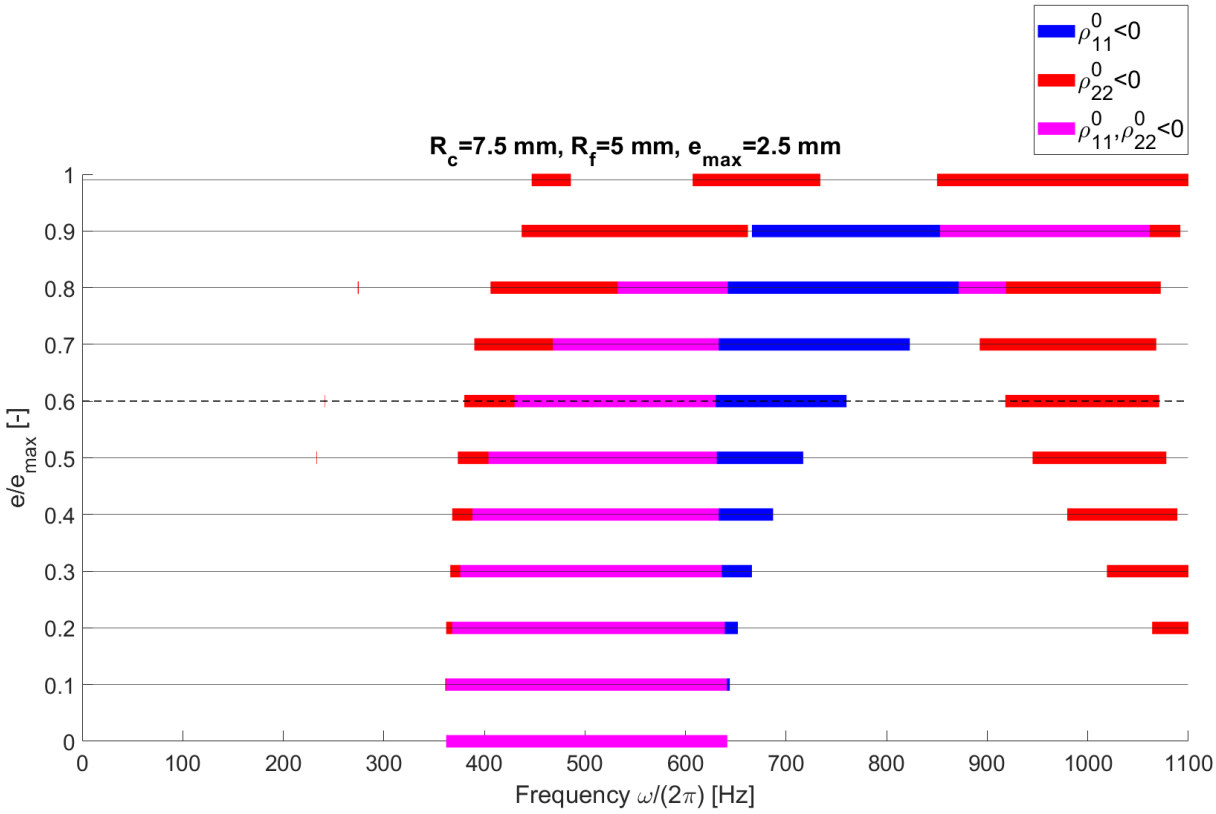

Figure 4.27. Frequency bands in which $\rho^0_{11} < 0$ and $\rho^0_{22} > 0$ (blue), $\rho^0_{22} < 0$ and $\rho^0_{11} > 0$ (red) and $\rho^0_{11} < 0$ and $\rho^0_{22} < 0$ (purple) for different values of the ratio e/e_{max}

Another interesting aspect is that figure 4.25 and 4.27 can be used in a combined way in order to provide a proper geometric configuration of the metamaterial for specific purposes. For example, in the next chapter 5, the purpose is to provide well separated polarization bands. A proper combination of R_f and e can be identified in order to satisfy this request. In particular, making reference to figure 4.25 and 4.27, the design choice can be the use of a lower R_f and an higher e with respect to the original study case of figure 4.1 in which the polarization bands are not separated, as shown in figure 4.12.

This parametric discussion is strictly linked with an important open topic which is the metamaterial optimization, as explained in chapter 6. In particular, the aim of the optimization is to provide, among several geometric and material parameters, a suitable design configuration of the metamaterial in order to satisfy specific requests and purposes. A request can be, for example, the achivement of specific configurations of band gaps and polarization bands within proper frequency ranges.

Chapter 5

Transmission analyses

This chapter is devoted to the transmission analyses of different locally-resonant metamaterials with anisotropic mass density. As depicted in figure 5.1, we consider three different kind of unit cell, all characterized by the side $L = 21$ mm, the coating radius $R_c = 7.5$ mm, the fiber radius $R_f = 3.5$ mm and the eccentricity $e = 3.25$ mm, with three different angles of inclination θ of the eccentricity with respect to $\boldsymbol{e}_1$. The material properties are the same shown in table 4.1. The first case, shown in figure 5.1 a, consists of horizontally eccentric fiber ($\theta = 0°$), the second case, shown in figure 5.1 b, consists of eccentric fiber with $\theta = 45°$ and the third case, shown in figure 5.1 c, consists of vertically eccentric fiber ($\theta = 90°$).

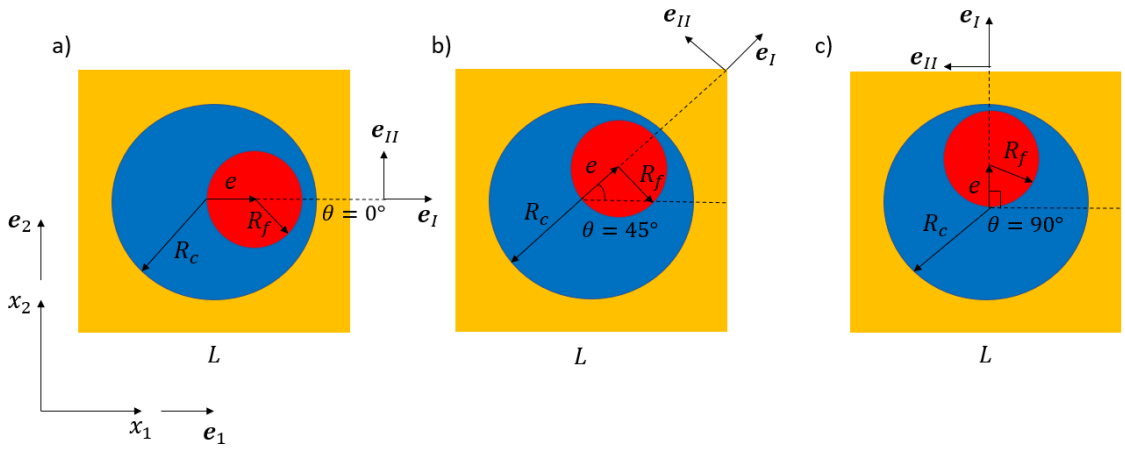

Figure 5.1. Unit cell of the three different kind of metamaterial considered with a) $\theta = 0°$ b) $\theta = 45°$ c) $\theta = 90°$.

The evaluation of the frequency-dependent effective dynamic mass density is performed numerically following the procedure developed in subsection 4.2.2. The unit vectors related to the principal mass reference system are $\boldsymbol{e}_I - \boldsymbol{e}_{II}$ and ρ^0_I, ρ^0_{II} are the eigenvalues of the equivalent frequency-dependent mass density tensor, obtained through the two scale homogenization approach. Figure 5.2 shows the normalized effective mass density represented by ρ^0_I and ρ^0_{II}. In the first case (figure 5.1 a), $x_1 - x_2$ is the principal mass reference system, i.e., $\rho^0_I = \rho^0_{11}$ and $\rho^0_{II} = \rho^0_{22}$. In the second case (figure 5.1 b), the principal mass reference system $\boldsymbol{e}_I - \boldsymbol{e}_{II}$ is rotated by

45° with respect to $\boldsymbol{e}_1 - \boldsymbol{e}_2$. For the third case (figure 5.1 c), $\boldsymbol{e}_I - \boldsymbol{e}_{II}$ is rotated by 90° with respect to $\boldsymbol{e}_1 - \boldsymbol{e}_2$. In the latter case, $\rho^0_I = \rho^0_{22}$ and $\rho^0_{II} = \rho^0_{11}$.

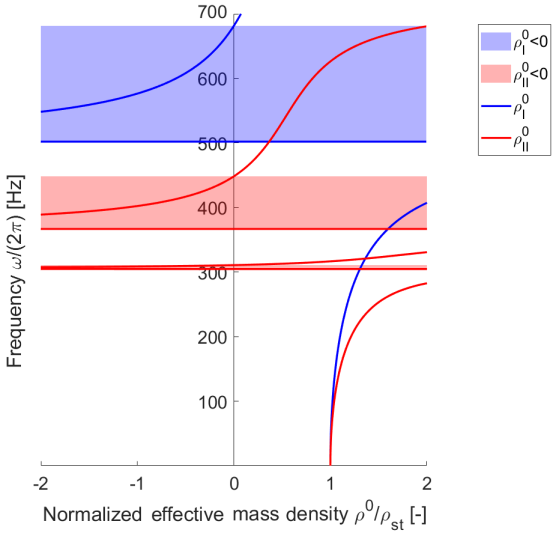

Figure 5.2. Principal values of the effective mass density tensor for $L = 21$ mm, $R_c = 7.5$, $R_f = 3.5$ mm and $e = 3.25$ mm.

With reference to figure 5.2, the regions shaded in red and in blue represent the polarization bands. In the blue zone, one has ρ^0_I <0 and ρ^0_{II} >0, whereas in the red zones, ρ^0_{II} <0 and ρ^0_I >0.

In the next sections, we will show the effect of the polarization bands on the transmission analyses for different configurations of the locally-resonant metamaterial. These transmission analyses are carried out numerically with the finite element software COMSOL Multiphysics. In particular, we will consider three study cases in which the locally-resonant metamaterial is composed by the unit cells shown in figures 5.1 a ($\theta = 0°$), 5.1 c ($\theta = 90°$) and 5.1 b ($\theta = 45°$).

5.1 Eccentric fibers with θ=0°

5.1.1 $\boldsymbol{e}_I$-transmission analysis

As a first case, we consider a locally-resonant metamaterial composed by an array of 40×1 cells with horizontally eccentric fibers ($\theta = 0°$). In this case, the principal mass directions $\boldsymbol{e}_I$ and $\boldsymbol{e}_{II}$ concides with $\boldsymbol{e}_1$ and $\boldsymbol{e}_2$ respectively. The imposed boundary conditions are:

- a unitary horizontal displacement on the left side of the array
- a fixed vertical displacement of the mean point of the left side of the array.

Through the finite element analysis, it is evaluated $\langle u \rangle$, i.e., the average value of the horizontal displacement, on the right side of the array. Figure 5.3 shows the

configuration of the metamaterial within the imposed boundary conditions and the evaluated output.

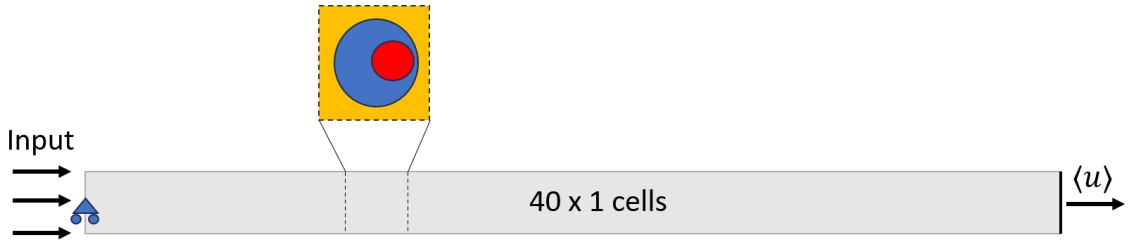

Figure 5.3. Array of 40×1 cells with horizontally eccentric fibers ($\theta = 0°$), employed in the $\boldsymbol{e}_I$-transmission analysis.

Figure 5.4 shows the semi-logarithmic transmission spectrum of $|\langle u \rangle|$, as a function of the frequency, with a black line. The blue shaded region is the frequency interval in which $\rho_I^0 < 0$ and the red shaded regions are the ones in which $\rho_{II}^0 < 0$. The polarization bands are the same depicted in figure 5.2.

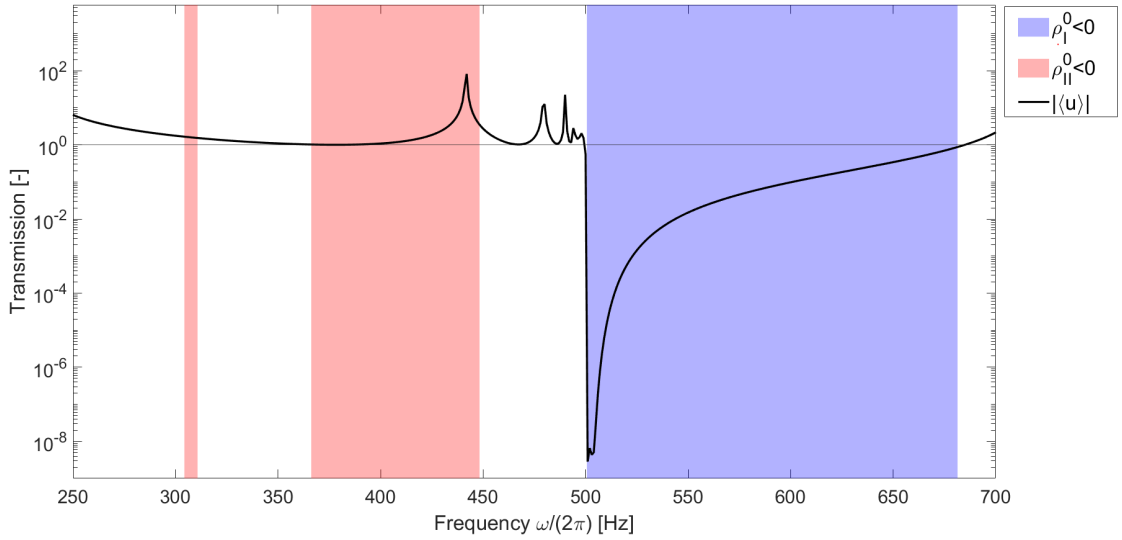

Figure 5.4. Transmission spectrum of $|\langle u \rangle|$ as a function of frequency for the array of 40×1 cells (θ=0°) with imposed $\boldsymbol{e}_I$-displacement.

With reference to figure 5.4, taking into consideration that the propagating waves are polarized in the $\boldsymbol{e}_I$-direction, in the blue zone ($\rho_I^0 < 0$) $|\langle u \rangle|$ is absorbed. In the white and red zones, in which $\rho_I^0 > 0$, the absorption does not take place. The trend of $|\langle u \rangle|$ at the opening frequency of the blue band is due to the absorption which takes place in very few cells. In the red zone, in which $\rho_{II}^0 < 0$, the wave polarization direction is oriented with the principal direction of the positive mass ρ_I^0 and, since this direction is horizontal, $|\langle u \rangle|$ is not absorbed.

In the blue polarization band, the activated local resonance mechanism is the one of the resonance mode, related to the inclusion, at the opening frequency of the polarization band. As shown for the first cell of the array in figure 5.5 a), at a frequency close to the opening of this band ($\omega/2\pi = 505$ Hz), the displacements associated to the matrix and to the fiber (resonating mass) are in phase opposition. The wave absorption occurs within few cells and this can be noticed from the contour plot of figure 5.5 a) in which u, i.e., the horizontal component of the displacement field, decreases in amplitude up to a null value after few cells. The absorption can be observed making reference to the matrix only. As shown for the first cell of the array in figure 5.5 b), also at a frequency near to the closure of this band ($\omega/2\pi = 681$ Hz), the displacements of the matrix and the fiber are in phase opposition. Making reference to the matrix only, as shown in figure 5.5 c), the local resonance mechanism is active also in the last cells of the array and, thus, the full absorption is not achieved within 40 cells but it requires a larger number.

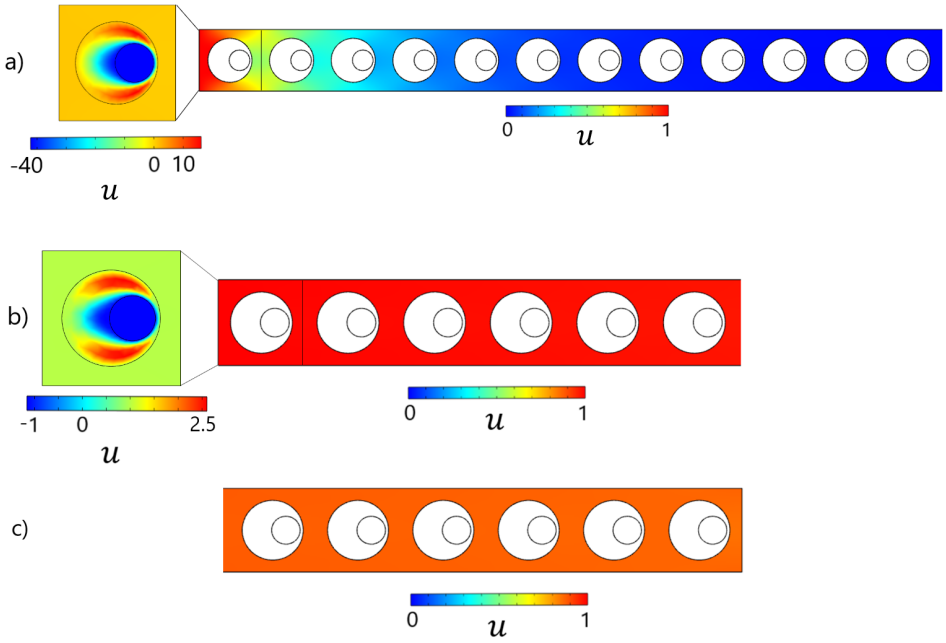

Figure 5.5. a) Contour plot of the horizontal displacement in the first twelve cells of the array at frequency $\omega/2\pi = 505$ Hz b) Contour plot of the horizontal displacement in the first six cells of the array at frequency $\omega/2\pi = 681$ Hz c) Contour plot of the horizontal displacement in the last six cells of the array at frequency $\omega/2\pi = 681$ Hz.

In order to show a case in which the displacement of the fiber is in phase with respect to the displacement related to the matrix, in the second red polarization band (ρ^0_{II} <0), the peak in transmission is taken into account at the frequency $\omega/2\pi = 442$ Hz. Figure 5.6 shows that the displacement of the fiber is amplified with respect to the displacement of the matrix.

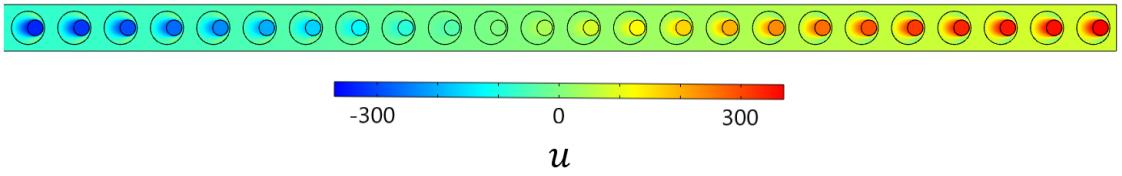

Figure 5.6. Contour plot of the horizontal displacement in the last twentyfour cells of the array at frequency $\omega/2\pi = 442$ Hz.

5.1.2 e_{II}-transmission analysis

We now consider the same media employed in subsection 5.1.1 but with different boundary conditions:

- a unitary vertical displacement on the left side of the array
- a fixed horizontal displacement of the mean point of the left side of the array.

Moreover, it is evaluated $\langle v \rangle$, i.e., the average value of the vertical displacement, on the right side of the array. Figure 5.7 shows the configuration of the metamaterial within the imposed boundary conditions and the evaluated output.

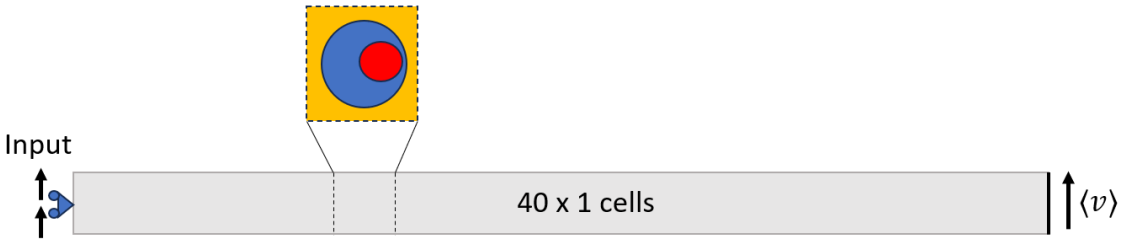

Figure 5.7. Array of 40×1 cells with horizontally eccentric fibers ($\theta = 0°$), employed in the $\boldsymbol{e}_{II}$-transmission analysis.

For this second case, figure 5.8 shows the semi-logarithmic transmission spectrum of $|\langle v \rangle|$ as a function of the frequency. With reference to figure 5.8, taking into account that the propagating waves are polarized in the $\boldsymbol{e}_{II}$-direction, in the red zones ($\rho^0_{II} < 0$) $|\langle v \rangle|$ is absorbed. In the blue and white zones, in which $\rho^0_{II} > 0$, the absorption does not occur. The trend of $|\langle v \rangle|$ at the opening frequencies of the red bands is due to the absorption that takes place in very few cells. In the blue zone, in which $\rho^0_I < 0$, the wave polarization direction is oriented with the principal direction of the positive mass ρ^0_{II} and, since this direction is vertical, $|\langle v \rangle|$ is not absorbed.

In the red polarization bands, the activated local resonance mechanisms are the ones of the resonance modes, related to the inclusion, at the opening frequencies of the polarization bands. As shown for the first cell of the array in figure 5.9 a), at a frequency close to the opening of the second band ($\omega/2\pi = 371$ Hz), the

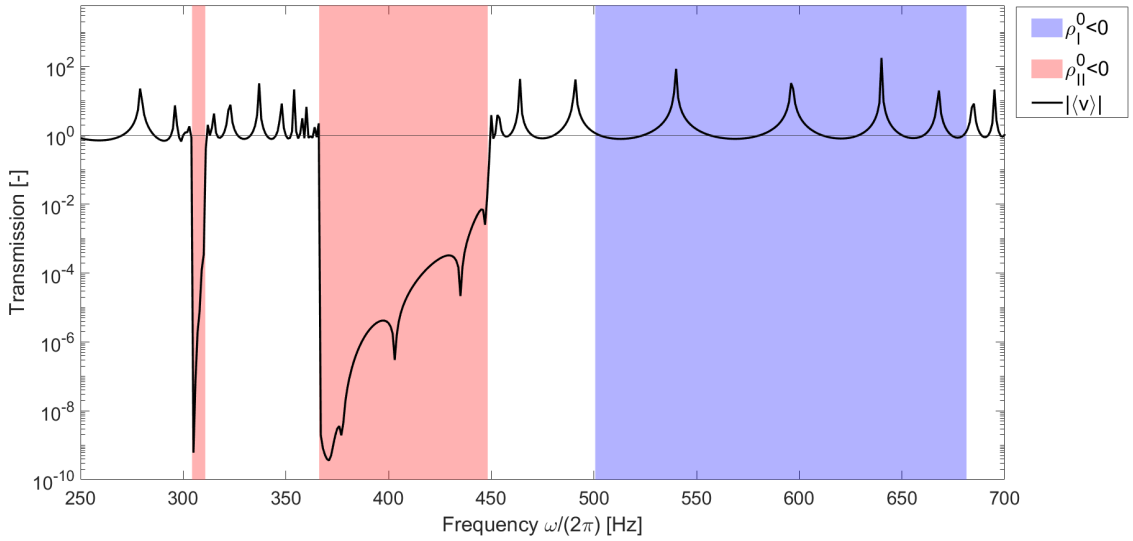

Figure 5.8. Transmission spectrum of $|\langle v \rangle|$ as a function of the frequency for the array 40×1 cells (θ=0°) and the imposed $\boldsymbol{e}_{II}$-displacement.

displacements associated to the matrix and to the fiber are in phase opposition. The absorption of the wave occurs within few cells and this can be noticed from the contour plot of figure 5.9 a) in which v, i.e., the vertical component of the displacement field, decreases in amplitude up to a null value after few cells. The absorption can be noticed making reference to the matrix only. As shown for the first cell of the array in figure 5.9 b), at a frequency near to the closure of the second band ($\omega/2\pi = 447$ Hz), the displacements of the matrix and the fiber are in phase opposition. Differently than the case in subsection 5.1.1, as shown in figure 5.9 b), the full absorption is achieved but with a larger number of cells with respect to the ones provided in $\omega/2\pi = 371$ Hz.

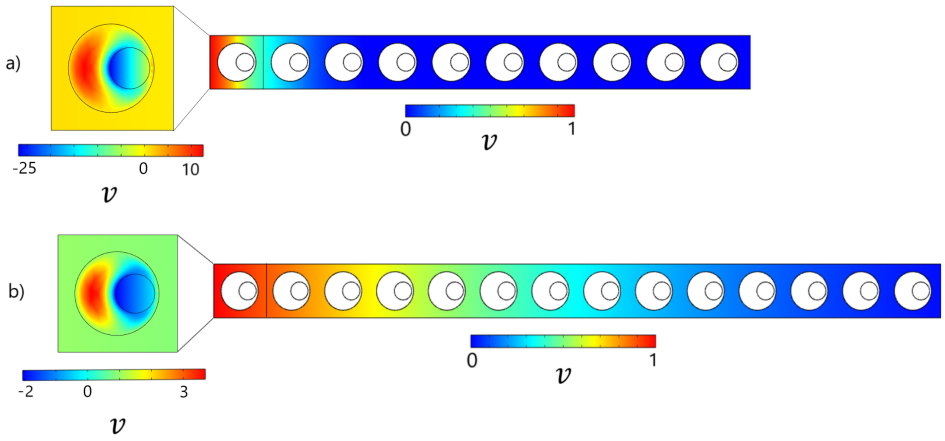

Figure 5.9. a) Contour plot of the vertical displacement in the first ten cells of the array at frequency $\omega/2\pi = 371$ Hz b) Contour plot of the vertical displacement in the first fourteen cells of the array at frequency $\omega/2\pi = 447$ Hz.

5.2 Eccentric fibers with θ=90°

5.2.1 e_I-transmission analysis

Firstly, we consider an array of 40×1 cells with vertically eccentric fibers (θ=90°). In this new case, the principal mass directions $\boldsymbol{e}_I$ and $\boldsymbol{e}_{II}$ are oriented as $\boldsymbol{e}_2$ and $\boldsymbol{e}_1$ respectively. We impose the following boundary conditions:

- a unitary vertical displacement on the left side of the array
- a fixed horizontal displacement of the mean point of the left side of the array.

The evaluation of $\langle v \rangle$, i.e., the average value of the vertical displacement, is defined on the right side of the array through the finite element analysis. Figure 5.10 shows the metamaterial taken into consideration within the boundary conditions and the related output.

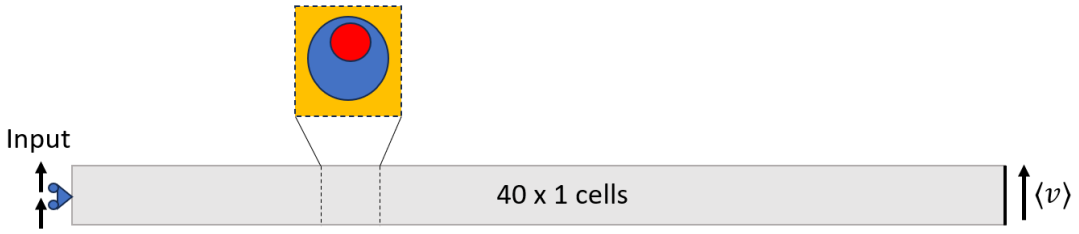

Figure 5.10. Array of 40×1 cells with vertically eccentric fibers ($\theta = 90°$), employed in the $\boldsymbol{e}_I$-transmission analysis.

Figure 5.11 shows the semi-logarithmic transmission spectrum of $|\langle v \rangle|$ as a function of the frequency and the polarization bands are the same shown in figure 5.2.

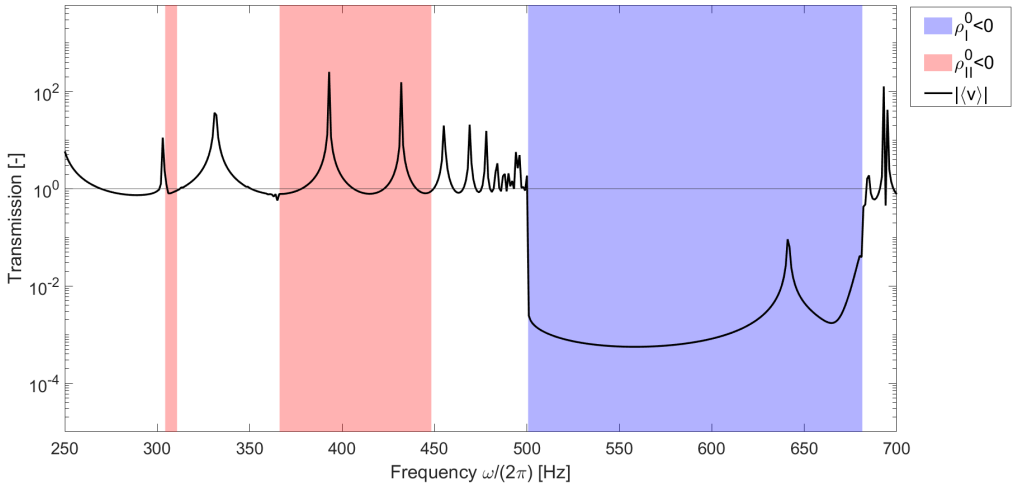

Figure 5.11. Transmission spectrum of $|\langle v \rangle|$ as a function of the frequency for the array 40×1 cells (θ=90°) and the imposed $\boldsymbol{e}_I$-displacement.

With reference to figure 5.11, the propagating waves are polarized in the $\boldsymbol{e}_I$-direction; therefore, in the blue zone, in which $\rho_I^0 < 0$, $|\langle v \rangle|$ is absorbed, while in the other zones, in which $\rho_I^0 > 0$, the wave absorption does not occur. The trend of $|\langle v \rangle|$ at the opening frequency of the blue band is due to the fact that absorption takes place in very few cells.

5.2.2 $\boldsymbol{e}_{II}$-transmission analysis

We now take into consideration the same metamaterial discussed in subsection 5.2.1 but with the following boundary conditions:

- a unitary horizontal displacement on the left side of the array
- a fixed vertical displacement of the mean point of the left side of the array.

$\langle u \rangle$, i.e., the average value of the horizontal displacement, is evaluated on the right side of the array through the finite element analysis and figure 5.12 shows the configuration of the metamaterial with the new boundary conditions and the relative output.

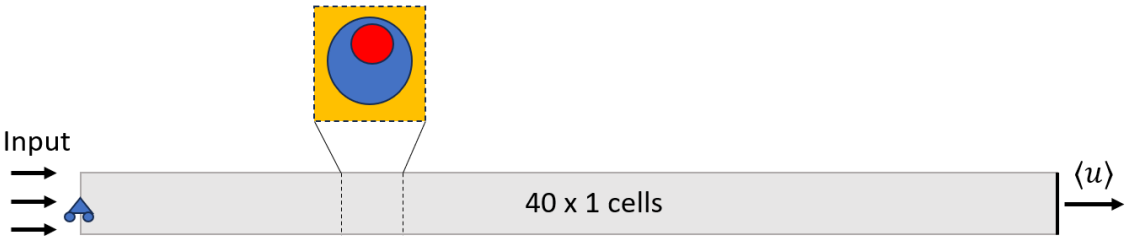

Figure 5.12. Array of 40×1 cells with vertically eccentric fibers ($\theta = 90°$), employed in the $\boldsymbol{e}_{II}$-transmission analysis.

For this new case, figure 5.13 shows the semi-logarithmic transmission spectrum of $|\langle u \rangle|$ as a function of the frequency.

With reference to figure 5.13, it is important to remind that the propagating waves are now polarized in the $\boldsymbol{e}_{II}$-direction and, thus, in the red zones ($\rho_{II}^0 < 0$) $|\langle u \rangle|$ is absorbed. In the other zones, in which $\rho_{II}^0 > 0$, the absorption does not take place. The trend of $|\langle u \rangle|$ at the opening frequencies of the red bands is due to the absorption that occurs in very few cells. In figure 5.13, due to the presence of some off-curve points, are shown two close-up in red obtained by performing finite element analyses with a finer frequency discretization.

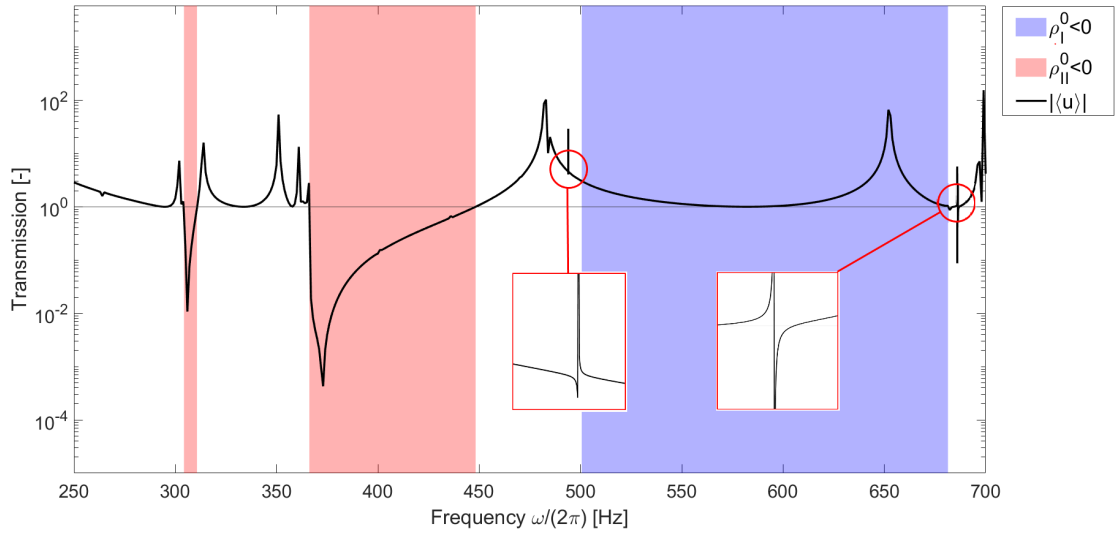

Figure 5.13. Transmission spectrum of $|\langle u \rangle|$ as a function of the frequency for the array 40×1 cells (θ=90°) and the imposed $\boldsymbol{e}_{II}$-displacement. The close-up in red represent a more refined trends of $|\langle u \rangle|$ at two different frequencies.

5.3 Eccentric fibers with θ=45°

We now consider a two-dimensional locally-resonant metamaterial, as shown in figure 5.14, constituted of an array of 7×21 cells having eccentric fibers with $\theta = 45°$. In this case, $\boldsymbol{e}_I$ is inclined by 45° with respect to $\boldsymbol{e}_1$, while $\boldsymbol{e}_{II}$ is inclined by -45°. For the transmission analysis, we consider the following boundary conditions:

- a unitary displacement along $\boldsymbol{e}_I$ on the left edge of the three central cells
- fixed displacement along $\boldsymbol{e}_{II}$ on the mid-point of the left edge of the media.

The response of the metamaterial is evaluated in terms of the displacement components along $\boldsymbol{e}_I$, i.e., $\langle u\cos(45°) + v\sin(45°)\rangle$, where u is the horizontal displacement and v is the vertical displacement and along $\boldsymbol{e}_{II}$, i.e., $\langle -u\sin(45°) + v\cos(45°)\rangle$, in the two points P_1 and P_2, as shown in figure 5.14.

Figure 5.15 shows the semi-logarithmic transmission spectrum of $|\langle u\cos(45°) + v\sin(45°)\rangle|$ in P_1 as a function of the frequency. The polarization bands are the same depicted in figure 5.2. With reference to figure 5.15, it is important to take into account that the propagating waves are polarized in the $\boldsymbol{e}_I$-direction; therefore, in the blue zone (ρ_I^0 <0) $|\langle u\cos(45°) + v\sin(45°)\rangle|$ is mainly absorbed. Also in this case, the trend of $|\langle u\cos(45°) + v\sin(45°)\rangle|$ at the opening frequency of the blue band is affected by an absorption which takes place in very few cells. However, differently than the cases described in sections 5.1 and 5.2, in three different frequencies, $|\langle u\cos(45°) + v\sin(45°)\rangle|$ is not absorbed but shows some peaks of amplification. The reason is related to the presence of global resonant modes of the matrix only.

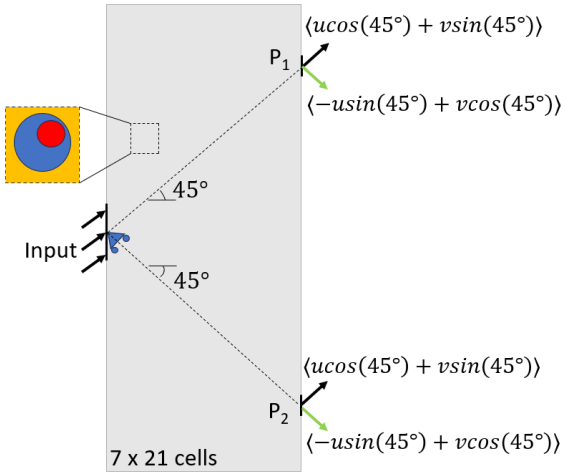

Figure 5.14. Media of 7×21 cells and eccentric fibers with $\theta = 45°$, employed in the inclined transmission analysis.

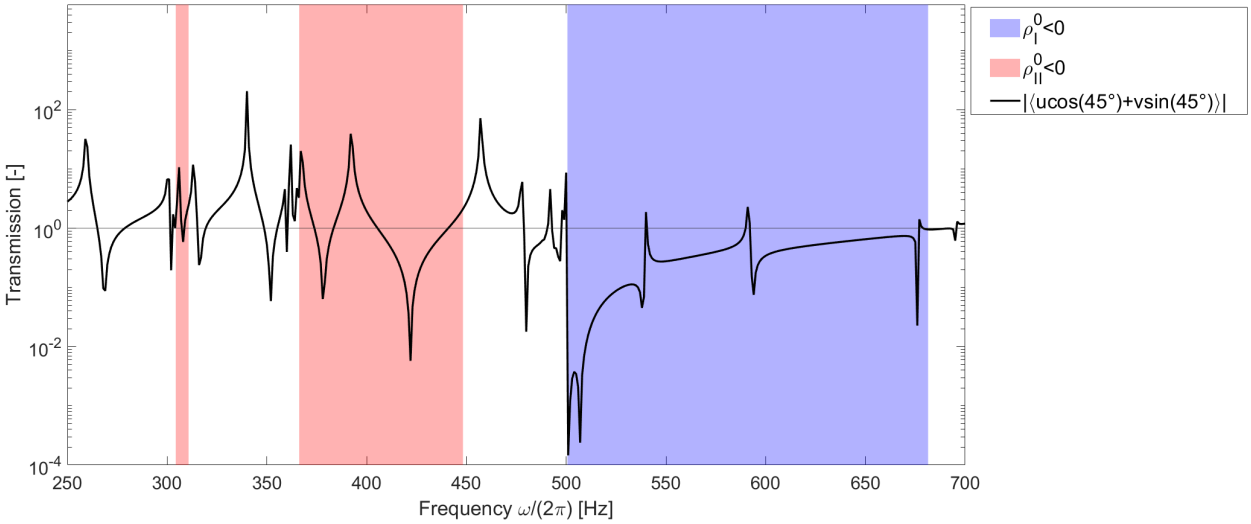

Figure 5.15. Transmission spectrum of $|\langle u\cos(45°) + v\sin(45°)\rangle|$ in P_1 as a function of the frequency for the inclined transmission analysis.

The frequency responses of the three peaks of amplification, which occur in the blue band, are shown in figure 5.16. These peaks are associated to global resonant modes of the matrix only.

However, these modes, in correspondence of the three peaks, are the cause of the amplification of the wave in a polarization band in which the expected result is an absorption. A possible solution, to reduce such a problem, could be to consider a larger domain for the transmission analysis of the metamaterial, which however would increase the computational burden.

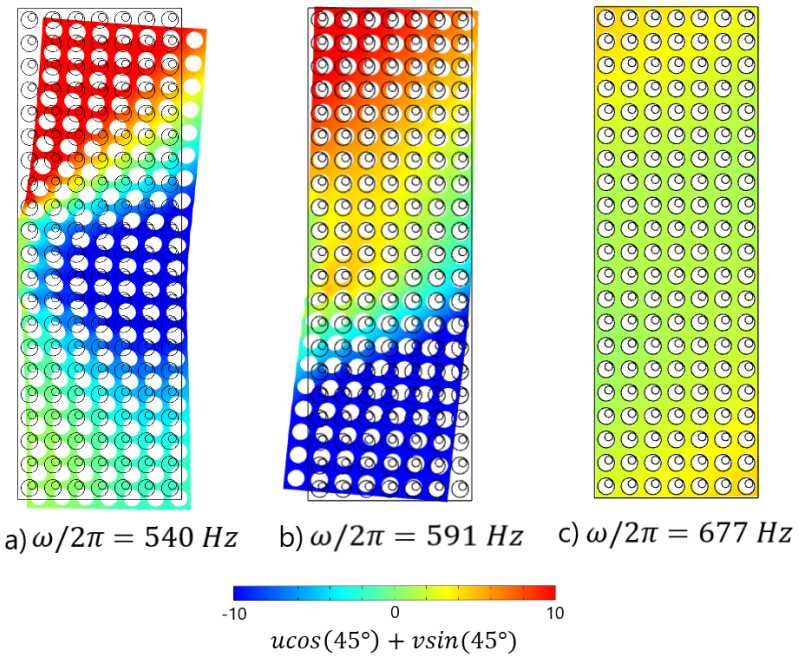

Figure 5.16. Contour plot of $u\cos(45°)+v\sin(45°)$ on the deformed shape for: a) $\omega/2\pi = 540$ Hz b) $\omega/2\pi = 591$ Hz c) $\omega/2\pi = 677$ Hz.

In this blue polarization band, when the global resonant modes occur, the absorption is not achieved but it is always provided that $|\langle -u\sin(45°)+v\cos(45°)\rangle| > |\langle u\cos(45°)+ +v\sin(45°)\rangle|$ in P_1, as shown in figure 5.17. The latter shows the close-up view of the transmission spectrum of figure 5.15 at three different frequency ranges which contain the peaks of amplification. In order to provide a more accurate trend for the peaks, it has been developed a more refined frequency discretization in the finite element analysis.

With reference to figure 5.17, it is possible to notice that in the $\boldsymbol{e}_{II}$-direction in which $\rho^0_{II} > 0$, the propagation is always higher than in the $\boldsymbol{e}_I$-direction in which $\rho^0_I < 0$. This effect is pronounced at the opening of the blue band (a) but it is reduced in (b) and (c). The peaks of the green curve, in all the three cases, have the same order of magnitude, while the values of the peaks related to the black curve increase from figure 5.17 a) to figure 5.17 c). The most important aspect to consider is that, observing the close-up view of figure 5.17, mode conversion can be achieved within the polarization band. The displacement $|\langle -u\sin(45°) + v\cos(45°)\rangle|$, represented by the green curve, is oriented as $\boldsymbol{e}_{II}$ which is orthogonal to $\boldsymbol{e}_I$. These results are very important because they ensure the achievement of one of the aims of the thesis.

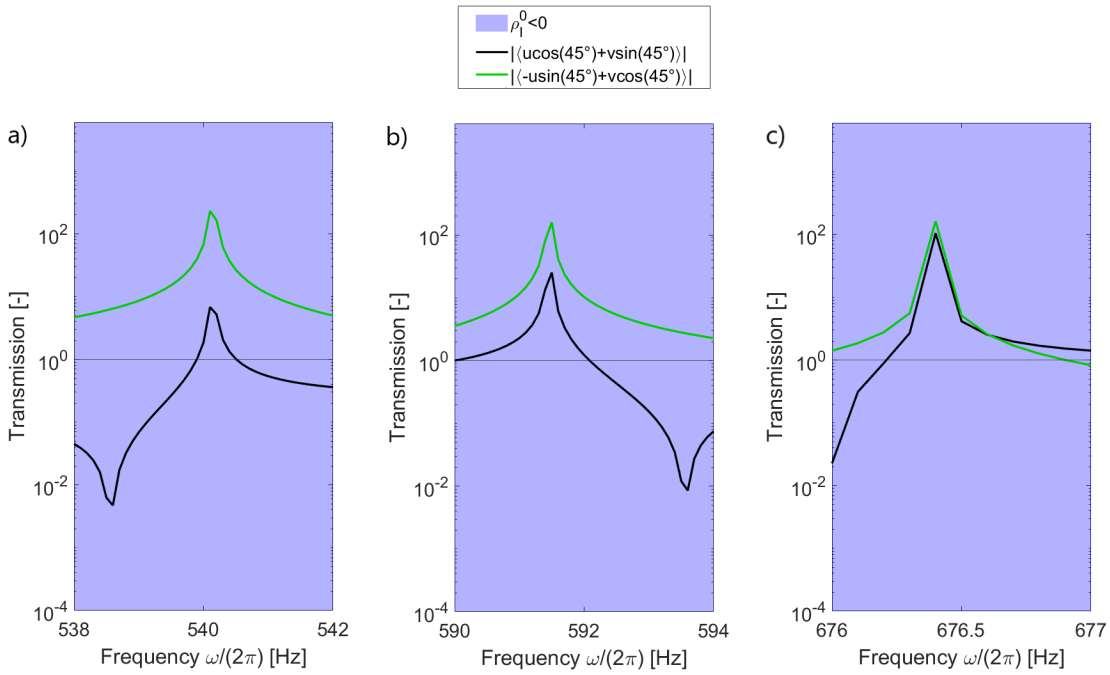

Figure 5.17. Close-up view of the transmission spectrum of figure 5.15 at frequencies: a) $\omega/2\pi = 540.1$ Hz b) $\omega/2\pi = 591.5$ Hz c) $\omega/2\pi = 676.4$ Hz. The black line is $|\langle u\cos(45°) + v\sin(45°)\rangle|$ and the green line is $|\langle -u\sin(45°) + v\cos(45°)\rangle|$.

Focusing our attention on point P_2, figure 5.18 shows the semi-logarithmic transmission spectrum of $|\langle -u\sin(45°) + v\cos(45°)\rangle|$ in P_2 as a function of the frequency.

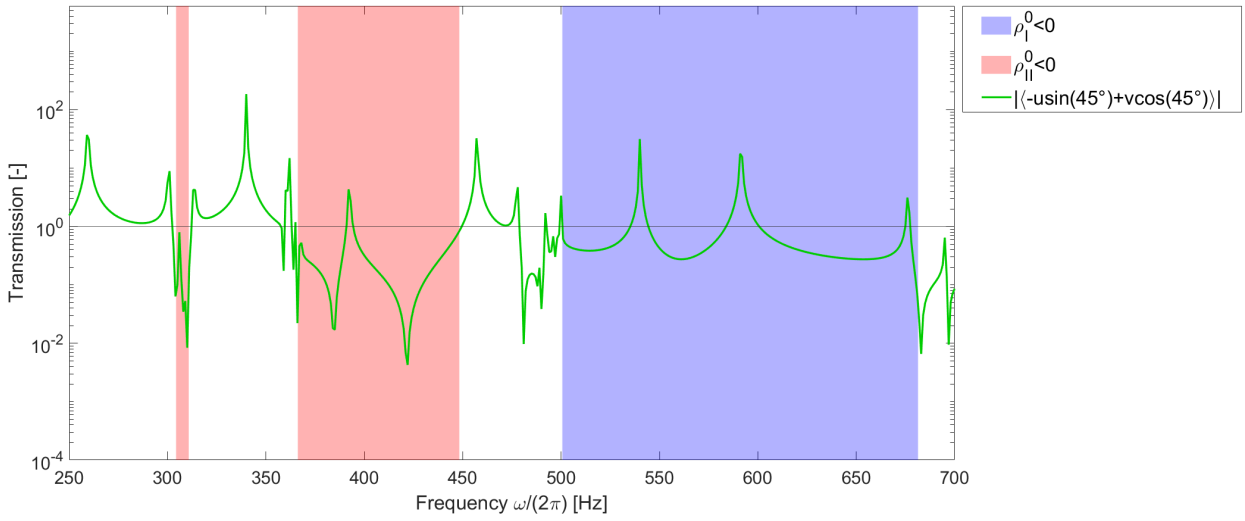

Figure 5.18. Transmission spectrum of $|\langle -u\sin(45°) + v\cos(45°)\rangle|$ in P_2 as a function of the frequency for the inclined transmission analysis.

With reference to figure 5.18, the propagating waves are now polarized in the

$\boldsymbol{e}_{II}$-direction and, thus, in the red zones (ρ^0_{II} <0) $|\langle -u\sin(45°) + v\cos(45°)\rangle|$ is mainly absorbed. At the opening frequencies of the red bands, the trend of $|\langle -u\sin(45°) + v\cos(45°)\rangle|$ is probably affected by global resonant modes since normally, at the opening of the bands, the wave absorption occurs in very few cells. Moreover, at a frequency of the second red band, $|\langle -u\sin(45°) + v\cos(45°)\rangle|$ is not absorbed but shows a peak of amplification due to the presence of a global resonant mode of the matrix only.

The frequency responses of the peaks, that occur at the opening frequencies of the red bands, and the peak of amplification, which occurs in the second red band, are shown in figure 5.19. These peaks are related to global resonant modes of the matrix only.

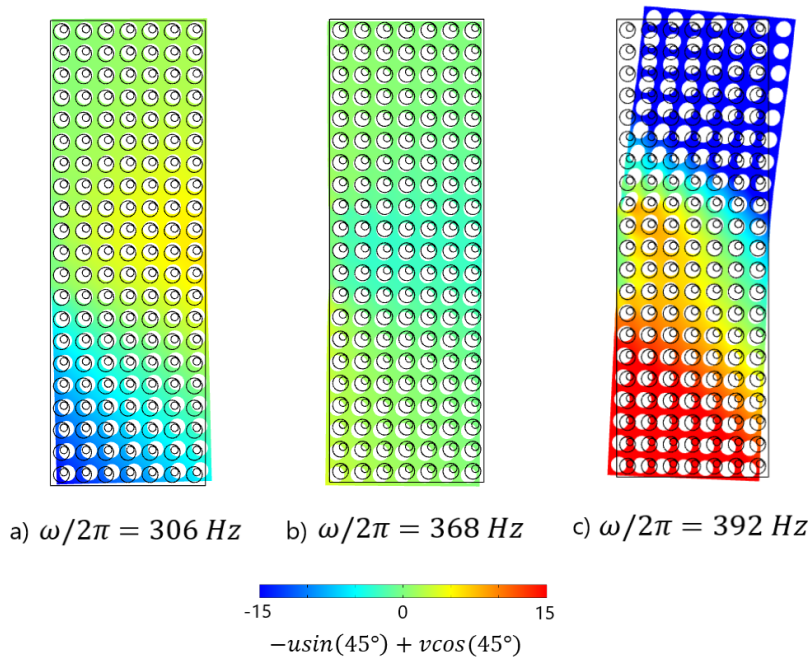

Figure 5.19. Contour plot of $-u\sin(45°) + v\cos(45°)$ on the deformed shape for: a) $\omega/2\pi =$ 306 Hz b) $\omega/2\pi = 368$ Hz c) $\omega/2\pi = 392$ Hz.

Also in this case, in order to reduce this problem, a solution could be to take into account a larger media for the transmission analysis. However, the computational burden would considerably increase.

In these red polarization bands, in correspondence of the frequencies in which global resonant modes occur, the absorption is not reached; however, it is always confirmed that $|\langle u\cos(45°) + v\sin(45°)\rangle| > |\langle -u\sin(45°) + v\cos(45°)\rangle|$ in P_2, as shown in figure 5.20. The latter shows the close-up view of the transmission spectrum of figure 5.18 at three different frequency intervals which include the peaks taken into consideration. Also in this case, it has been performed a more refined frequency discretization in the finite element analysis for obtaining a more accurate trend of

the peaks.

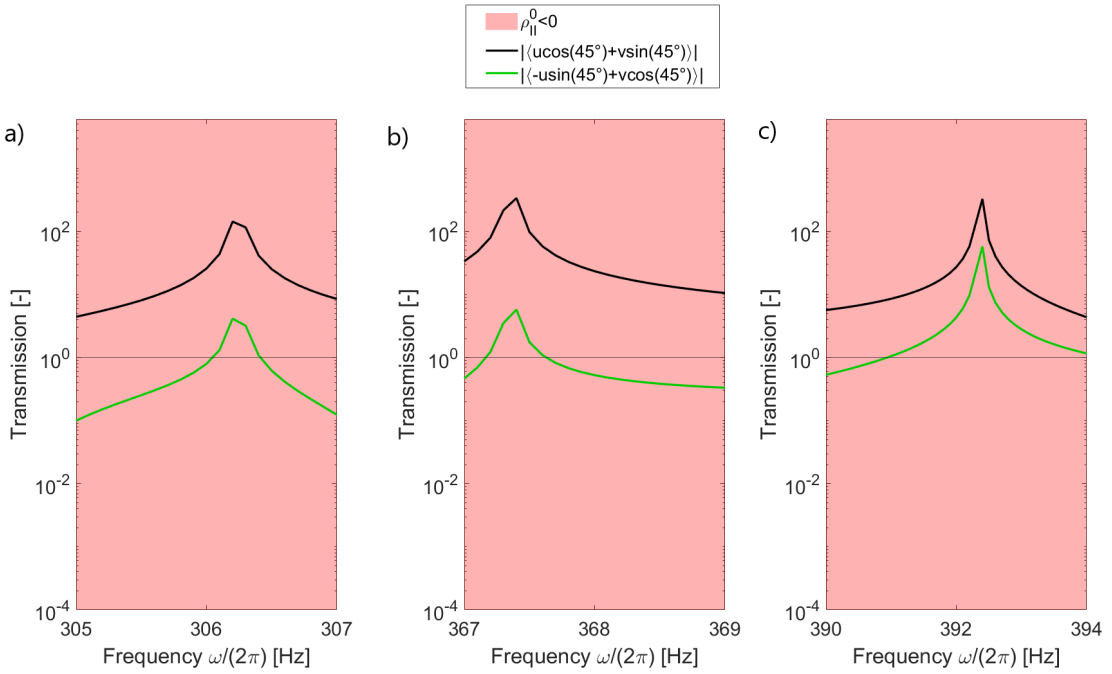

Figure 5.20. Close-up view of the transmission spectrum of figure 5.18 at frequencies: a) $\omega/2\pi = 306.2$ Hz b) $\omega/2\pi = 367.4$ Hz c) $\omega/2\pi = 392.4$ Hz. The green line is $|\langle -u\sin(45°) + v\cos(45°)\rangle|$ and the black line is $|\langle u\cos(45°) + v\sin(45°)\rangle|$.

With reference to figure 5.20 a) and b), the refined frequency discretization shows that the peaks at the opening frequencies of the red bands are actually of amplification. As shown in figure 5.20, in the $\boldsymbol{e}_I$-direction ($\rho_I^0 > 0$), the propagation is always greater than in the $\boldsymbol{e}_{II}$-direction ($\rho_{II}^0 < 0$). With reference to the second red band, the values of the peaks related to the green curve increase from figure 5.20 b) to figure 5.20 c), while the peaks of the black curve have the same order of magnitude. Observing the close-up view of figure 5.20, mode-converting mechanisms can be obtained inside the polarization bands. $|\langle u\cos(45°) + v\sin(45°)\rangle|$, represented by the black line, is directed as $\boldsymbol{e}_I$ which is orthogonal to $\boldsymbol{e}_{II}$. Also for this case, these results are meaningful because they guarantee the achievement of one of the goals of the work.

Chapter 6

Conclusions and further developments

The present work, focused on polarization control of elastic waves in anisotropic locally resonant metamaterials, has two main aims. The first one consists on studying the effect of the equivalent anisotropic dynamic mass density tensor, obtained through the homogenization approach, on band gaps and polarization bands. Through the study of the eingenvalues of the effective mass density tensor, the effects of several geometric parameters, related to the metamaterial taken into consideration, are highlighted. The second aim, which represents the core of the work since it is strictly related to real applications, is to demonstrate that the polarization bands, predicted by the homogenization technique, can effectively provide the polarization conversion of elastic waves and allow for mode-converting mechanisms.

We consider a ternary locally resonant metamaterial in which the unit cell, periodically repeated, is composed by a stiff matrix, a soft cylindrical coating and a heavy eccentric cylindrical fiber. The two-scale asymptotic homogenization technique is implemented in order to obtain the anisotropic dynamic mass density tensor. The study of the eigenvalues of this tensor allows us to predict band gaps and polarization bands. Furthermore, the band gaps can be qualitatively compared with the ones obtained by the Bloch-Floquet analysis. The results show that these frequency intervals are in good agreement from a qualitative point of view. The most important aspect to take into account is the role of the homogenized mass density tensor in the effective dispersion properties of the periodic media. In particular, the sign of the two principal mass components of this tensor governs the elastic wave propagation. Elastic waves can propagate in the case in which both the mass components are positive (pass bands) and they cannot propagate without attenuation when both the principal mass components are negative (band gaps). In the polarization bands, in which the mass components have a different sign, elastic waves can propagate with a unique polarization vector which direction is close to the principal direction of the positive mass component. From the numerical results, it is possible also to observe that, when the ratio between the negative and the positive mass tends to infinity, the polarization direction coincides with the principal direction of the positive mass. This ratio tends to infinity when the opening of the polarization bands occurs.

With reference to the second aim, several numerical transmission analyses have been developed for different geometric configurations of the locally resonant metamaterial. Starting from simple monodimensional arrays, the transmission spectra show that the polarization bands, predicted by the homogenization, act as filters that are able to absorb a wave with a polarization direction that is orthogonal to the one provided by the wave itself. At the opening of these polarization bands, it is shown that the wave is attenuated very efficiently in the first few cells. However, for the cases in which the eccentricity of the fiber is horizontal or vertical in the plane, mode-conversion cannot be achieved. In order to demonstrate the possibility to generate mode-converting mechanisms, a bidimensional array has been considered in which the eccentricity of the fiber is inclined by 45° with respect to the horizontal axis of the plane. In this case, global structural modes occur in the polarization bands in which the expected result is a wave absorption. These global structural modes take place since the geometry of the bidimensional array is finite. One can consider to extend the geometric configuration of the array but the time requested for the finite element analysis could be very long. Even if the global structural modes affect the results, mode-converting mechanisms are achieved in the polarization bands. It is shown that these bands provide a preferential wave polarization direction that is orthogonal to the direction in which the wave should be absorbed. This is an important result because mode-converting mechanisms are able to generate, e.g. [23], shear waves from a initial propagation of longitudinal waves. Shear waves, as shown in literature, are very useful in the civil engineering field, such as in non-destructive testing methods. Ultrasonic shear-wave tomography is a very diffuse technique that is able to detect cracks and delaminations in the reinforced concrete structures. Shear waves provide an higher resolution since they are slower than the longitudinal waves.

We studied the effects of two main geometric parameters, related to the metamaterial taken into account, on band gaps and polarization bands. In particular, it was possible to implement several numerical evaluations of the effective mass density tensor within different values of these geometric parameters. Band gaps and polarization bands, identified by the components of this tensor, can be compared for different values of the geometric parameters. With reference to the influence of the fiber radius with a fixed fiber eccentricity, it was possible to notice that for low values of this geometric parameter, the polarization bands are fully separated with short sizes and, thus, the band gaps are not achieved. While for higher values of the fiber radius, the polarization bands are larger and overlap providing the band gaps. The other case which has been analyzed is the one related to the influence of the fiber eccentricity with a fixed fiber radius. In the latter case, it was possible to notice that, increasing this geometric parameter, the polarization bands tend to be more separated with a lower possibility to achieve full band gaps. This is an expected result since the effective mass density tensor tends to be more anisotropic when the fiber eccentricity increases. When this geometric parameter is null, the effective mass density tensor becomes isotropic and, thus, only the band gap is obtained. Another interesting aspect is that these two separated analyses can be used in combined way in order to provide a suitable geometric configuration of the metamaterial for specific purposes. Furthermore, these parametric analyses can be extended also considering other material parameters.

The previous parametric discussion is strictly linked with an open topic which is the metamaterial optimization. Iterative optimization algorithms, such as genetic algorithms, can be numerically implemented in order to provide a suitable geometric configuration of the metamaterial useful for specific aims. The aim of these algorithms is to satisfy an objective function finding the optimal combination of several design variables. In the context of this thesis, an objective function can be related to the achievement of maximum mode-conversion in specific polarization bands and the design variables can be the geometric parameters related to the metamaterial, such as the angle of the fiber eccentricity.

Bibliography

[1] Kwek Tze Tan, HH Huang, and CT Sun. "Blast-wave impact mitigation using negative effective mass density concept of elastic metamaterials". In: *International Journal of Impact Engineering* 64 (2014), pp. 20–29.

[2] Luca D'Alessandro et al. "Low frequency 3D ultra-wide vibration attenuation via elastic metamaterial". In: *Scientific reports* 9.1 (2019), p. 8039.

[3] C Sugino, M Ruzzene, and A Erturk. "Merging mechanical and electromechanical bandgaps in locally resonant metamaterials and metastructures". In: *Journal of the Mechanics and Physics of Solids* 116 (2018), pp. 323–333.

[4] Jeonghoon Park, Dongwoo Lee, and Junsuk Rho. "Recent advances in non-traditional elastic wave manipulation by macroscopic artificial structures". In: *Applied Sciences* 10.2 (2020), p. 547.

[5] Claudia Comi and Larissa Driemeier. "Wave propagation in cellular locally resonant metamaterials". In: *Latin American Journal of Solids and Structures* 15 (2018).

[6] MARCO MOSCATELLI. "Locally resonant materials: wave propagation analyses and application to impact absorbers". In: (2018).

[7] Claudia Comi and Jean-Jacques Marigo. "Homogenization approach and Bloch-Floquet theory for band-gap prediction in 2D locally resonant metamaterials". In: *Journal of Elasticity* 139.1 (2020), pp. 61–90.

[8] JL Auriault and G Bonnet. "Dynamique des composites élastiques périodiques". In: *Arch. Mech* 37.4-5 (1985), pp. 269–284.

[9] J-L Auriault and Claude Boutin. "Long wavelength inner-resonance cut-off frequencies in elastic composite materials". In: *International Journal of Solids and Structures* 49.23-24 (2012), pp. 3269–3281.

[10] Jean-Jacques Marigo et al. "Effective dynamic properties of a row of elastic inclusions: the case of scalar shear waves". In: *Journal of elasticity* 128.2 (2017), pp. 265–289.

[11] Kim Pham, Agnes Maurel, and Jean-Jacques Marigo. "Two scale homogenization of a row of locally resonant inclusions-the case of anti-plane shear waves". In: *Journal of the Mechanics and Physics of Solids* 106 (2017), pp. 80–94.

[12] Richard V Craster, Julius Kaplunov, and Aleksey V Pichugin. "High-frequency homogenization for periodic media". In: *Proceedings of the Royal Society A: Mathematical, Physical and Engineering Sciences* 466.2120 (2010), pp. 2341–2362.

[13] T Antonakakis, Richard V Craster, and Sébastien Guenneau. "Homogenisation for elastic photonic crystals and dynamic anisotropy". In: *Journal of the Mechanics and Physics of Solids* 71 (2014), pp. 84–96.

[14] David Faraci, Claudia Comi, and Jean-Jacques Marigo. "Band gaps in metamaterial plates: asymptotic homogenization and Bloch-Floquet approaches". In: *Journal of Elasticity* 148.1 (2022), pp. 55–79.

[15] Léon Nicholas Brillouin. "Wave propagation in periodic structures: electric filters and crystal lattices". In: *(No Title)* (1953).

[16] Mats Åberg and Peter Gudmundson. "The usage of standard finite element codes for computation of dispersion relations in materials with periodic microstructure". In: *The Journal of the Acoustical Society of America* 102.4 (1997), pp. 2007–2013.

[17] A Srikantha Phani, J Woodhouse, and NA Fleck. "Wave propagation in two-dimensional periodic lattices". In: *The Journal of the Acoustical Society of America* 119.4 (2006), pp. 1995–2005.

[18] Grégoire Allaire, Marc Briane, and Muthusamy Vanninathan. "A comparison between two-scale asymptotic expansions and Bloch wave expansions for the homogenization of periodic structures". In: *SEMA journal* 73 (2016), pp. 237–259.

[19] Guy Bonnet and Vincent Monchiet. "Negative refraction of elastic waves on a metamaterial with anisotropic local resonance". In: *Journal of the Mechanics and Physics of Solids* 169 (2022), p. 105060.

[20] Garrett N Manion and Thomas J Stokkermans. "Polarization of Light". In: *StatPearls [Internet]*. StatPearls Publishing, 2023.

[21] Arnaud Burtin, Niels Hovius, and Jens M Turowski. "Seismic monitoring of torrential and fluvial processes". In: *Earth Surface Dynamics* 4.2 (2016), pp. 285–307.

[22] Luca D'Alessandro et al. "3D auxetic single material periodic structure with ultra-wide tunable bandgap". In: *Scientific reports* 8.1 (2018), p. 2262.

[23] Joshua Minwoo Kweun et al. "Transmodal Fabry-Pérot resonance: theory and realization with elastic metamaterials". In: *Physical review letters* 118.20 (2017), p. 205901.

[24] Pangil Choi et al. "Application of ultrasonic shear-wave tomography to identify horizontal crack or delamination in concrete pavement and bridge". In: *Construction and Building Materials* 121 (2016), pp. 81–91.

[25] MO Si-Chaib, H Djelouah, and M Bocquet. "Applications of ultrasonic reflection mode conversion transducers in NDE". In: *NDT & E International* 33.2 (2000), pp. 91–99.

[26] Georgios Sarris et al. "Fatigue State Characterization of Steel Pipes Using Ultrasonic Shear Waves". In: *IEEE Transactions on Ultrasonics, Ferroelectrics, and Frequency Control* 70.1 (2022), pp. 72–80.

[27] WA Wood. “Formation of fatigue cracks”. In: *Philosophical magazine* 3.31 (1958), pp. 692–699.

[28] NF Mott. “A theory of the origin of fatigue cracks”. In: *Acta Metallurgica* 6.3 (1958), pp. 195–197.

[29] FC Frank and WT Read Jr. “Multiplication processes for slow moving dislocations”. In: *Physical Review* 79.4 (1950), p. 722.

[30] Agnès Maurel, Jean-François Mercier, and Fernando Lund. “Scattering of an elastic wave by a single dislocation”. In: *The Journal of the Acoustical Society of America* 115.6 (2004), pp. 2773–2780.

[31] Agnes Maurel, Jean-François Mercier, and Fernando Lund. “Elastic wave propagation through a random array of dislocations”. In: *Physical review B* 70.2 (2004), p. 024303.

[32] Agnès Maurel et al. “Wave propagation through a random array of pinned dislocations: Velocity change and attenuation in a generalized Granato and Lücke theory”. In: *Physical review B* 72.17 (2005), p. 174111.

[33] P Jason White, Gregory T Clement, and Kullervo Hynynen. “Longitudinal and shear mode ultrasound propagation in human skull bone”. In: *Ultrasound in medicine & biology* 32.7 (2006), pp. 1085–1096.

[34] Greg T Clement, P Jason White, and K Hynynen. “Enhanced ultrasound transmission through the human skull using shear mode conversion”. In: *The Journal of the Acoustical Society of America* 115.3 (2004), pp. 1356–1364.

[35] Bowen Jing et al. “Skull microstructure and mode conversion in transcranial ultrasound imaging”. In: *2021 IEEE International Ultrasonics Symposium (IUS)*. IEEE. 2021, pp. 1–4.

[36] Vincent Laude. “Phononic crystals”. In: *Phononic Crystals*. de Gruyter, 2020.

[37] Mehran Jaberzadeh, Bing Li, and KT Tan. “Wave propagation in an elastic metamaterial with anisotropic effective mass density”. In: *Wave Motion* 89 (2019), pp. 131–141.